BERGISCHE UNIVERSITÄT WUPPERTAL

DISSERTATION

Boundary Conditions for multi-speed Lattice Boltzmann Methods

Autor:
Friedemann Klaß

betreut von:
Dr. Andreas Bartel, PD
Alessandro Gabbana, PhD

vorgelegt zur Erlangung des akademischen Grades eines Doktors der Naturwissenschaften (Dr. rer. nat.)

Applied and Computational Mathematics
Fachgruppe Mathematik & Informatik
Fakultät für Mathematik und Naturwissenschaften

März 2024

BERGISCHE UNIVERSITÄT WUPPERTAL

Abstract

Fakultät für Mathematik und Naturwissenschaften
Fachgruppe Mathematik & Informatik

Doktor rer. nat.

Boundary Conditions for multi-speed Lattice Boltzmann Methods

by Friedemann Klaß

The Lattice Boltzmann Method has undergone a rapid development and is widely used to simluate complex fluid flow problems in both academia and industry. In the method, grid nodes exchange information along a finite amount of predefined discrete velocities, which correspond to the abscisae of an underlying quadrature rule used to discretize the continuous velocity space of the Boltzmann equation. Increasing the order of the quadrature rule has proven crucial to increasing the methods range of applicability beyond the Navier-Stokes equations. In particular, it allows for simulations of thermal compressible flow governed by the Navier-Stokes-Fourier equations.

The corresponding velocity stencils exhibit discrete velocities with multiple speed levels. Thus, the neighbourhood a given node exchanges information with is increased beyond the nearest neighbours, which leads to the presence of multiple layer of boundary nodes. This makes the formulation of Boundary Conditions (BCs) for the method more difficult, as information needs to be posed on multiple layers of nodes. It is crucial for the method to treat these layers accurately and effectively. However, not many BCs for these multi-speed stencils are available.

In this work, two classes of BCs for such multi-speed methods are considered: First, wall BCs, i.e. mass-conserving Dirichlet BCs, from the literature are reviewed. A new thermal BC based on the assumption of non-equilibrium bounce-back is described and compared to selected existing BCs for multi-speed LBM in several well-known benchmarks for wall-bounded thermal flow such as Couette flow, Poiseuille flow and Rayleigh-Benard convection.

Second, non-reflecting BCs are explored. They are commonly posed when the boundary of the computational domain is purely artificial, i.e. when it stems from the truncation of a very large or unbounded domain. In this case, the fluid should ideally not interact with the boundary at all. While a few approaches to pose such BCs in the standard single-speed Lattice Boltzmann Method exist, there was no literature about non-reflecting BCs for multi-speed velocity stencils until very recently. In this thesis, the characteristic BC, discrete artificial BC and Perfectly Matched Layer approach are described and subsequently applied to the thermal multi-speed Lattice Boltzmann Method. Numerical results show clear improvements over a naive extrapolation BC. The discrete artifical BC has infeasibly large runtime requirements, while the characteristic BC and the Perfectly Matched Layer approach only add a moderate overhead. It is shown that the Perfectly Matched Layer approach can be combined with characteristic BCs to enhance computational efficiency.

Acknowledgements

Pursuing a PhD is a daunting task. Sterotypical downsides of life as a PhD student include difficult or unsupportive advisors, financial challenges, long hours and permanent stress. Looking back, I guess I can count myself rather lucky!

My advisors, PD Dr. Andreas Bartel and Alessandro Gabbana (PhD), were always willing to take time for discussion in spite of being quite busy themselves. This work would not have been possible withour their guidance, constructive criticism and occasional encouragement, and I am grateful for their support.

During my thesis work, I was employed at the working group Applied and Computational Mathematics lead by Prof. Dr. Michael Günther at the University of Wuppertal. This did not only prevent financial challenges, but was also a pleasant experience. All colleagues contributed to a friendly working athmosphere, which certainly had a positive impact on this work. To fulfill the teaching duties that came with my position, I was working together with Prof. Dr Michael Günther, Prof. Dr. Matthias Ehrhardt and PD Dr. Andreas Bartel, whom I would like to thank for the friendly and fruitful collaboration.

I am particularly thankful to my fellow PhD students who were sitting in the same boat as me: Anna, Hanna, Tatiana, Michelle, Lorenc, Sarah, Konrad, Jan, Daniel, Kevin, Jens, Lokahith and Daniele made my life as a PhD student much more enjoyable (Furthermore, they provided an involuntary audience for puns and sometimes even laughed!). On a more serious note, while I cannot argue that there were neither long hours nor stress, they made the more intense phases of life as a PhD student more bearable by relating to the occasional frustration and offering coffee breaks at the right time.

Finally, I would like to thank my parents for supporting me all the way.

Contents

List of Abbreviations

BBGKY Bogoliubov, Born, Green, Kirkwood and Yvon

BC Boundary Condition

BE Boltzmann Equation

BGK Bhatnagar, Gross and Krook

CBC Characteristic Boundary Condition

CEE Chapman-Enskog Expansion

CFD Computational Fluid Dynamics

DABC Discrete Artificial Boundary Condition

EBC Equilibrium Boundary Condition

LBM Lattice Boltzmann Method

LODI Local One-Dimensional Inviscid

NEBB Non-Equilibrium Bounce-Back

NEEP Non-Equilibrium Extrapolation

NRBC Non-Reflecting Boundary Condition

PML Perfectly Matched Layer

RBC Regularized Boundary Condition

ZG Zero Gradient

List of Symbols

Symbol	Meaning
$a^{(n)}$	n-th Hermite expansion coefficient
c_D	Drag coefficient
c_L	Lift coefficient
c_p	Specific heat capacity at constant pressure
c_s	Lattice speed of sound
c_v	Specific heat capacity at constant volume
$\mathbf{c}^{(i)}$	Integer valued discrete mesoscopic velocity
d	Amount of discrete velocities
D	Amount of spatial dimensions
e	Internal energy per unit mass
E	Total energy per unit mass
Ec	Eckert number
e_Z	global relative L^2 error in Z
$\widetilde{e}_Z$	pointwise relative L^2 error in Z
f	Distribution function
f^{eq}	Equilibrium distribution function
$\mathbf{g}$	External acceleration
$H_{\max}$	max. history depth (DABC)
$\mathcal{H}^{(n)}$	$n-$th Hermite polynomial
$\hat{\mathcal{H}}^{(n)}$	$n-$th orthonormal Hermite polynomial
$\mathbf{i}$	Imaginary unit
k_B	Boltzmann constant
Kn	Knudsen number
$\mathcal{L}_x$	Vector of wave amplitude variations (CBC)
$\overline{\mathcal{L}}_x$	Modified vector of wave amplitude variations (CBC)
m	Molecular mass
M	Order of the highest relevant velocity moment
$\mathcal{M}$	Max. displacement of a given stencil
Ma	Mach number
N	Truncation order of Hermite-expansion
N_{iter}	Max. Iteration in a LBM simulation
p	Pressure
$\mathbf{P}$	Momentum-flux tensor
Pr	Prandtl number
Ra	Rayleigh number

Symbol	Meaning
$\mathbf{q}$	Heat-flux
Q	Degree of precision of a quadrature
r	Lattice constant
Re	Reynolds number
t	Time
T	Temperature
$\mathbf{u}$	Macroscopic velocity
$\mathbb{U}$	Vector of macroscopic target values (CBC)
$\mathbf{v}$	Mesoscopic velocity
$\mathbf{v}^{(i)}$	Discrete mesoscopic velocity
W	Width of dampening zone (PML)
$\mathbf{x}$	Spatial coordinate
Z	Generic macroscopic variable
$\otimes$	Outer product

α	Thermal diffusivity
δ_{ij}	Kronecker Delta
κ	Thermal conductivity
μ	Dynamic viscosity
ν	Kinematic viscosity
ρ	Density
$\boldsymbol{\sigma}$	Deviatoric stress tensor
$\sigma_{\max}$	Max. dampening coefficient (PML)
ω_i	Weight of a quadrature rule
Ω	Collision operator
Ω_{BGK}	BGK-collision operator

Chapter 1

Introduction

The prediction of fluid flow phenomena is of major importance for a wide range of academic and industrial applications, be it weather forecasting, studying mixtures or suspensions or aerodynamic shape optimization. With the Lattice Boltzmann Method (LBM), a versatile, easy to implement, computationally efficient and highly parallelizable [1] solver has been developed over the last few decades.

The method evolves a particle distribution function that gives the probability of finding a particle with a given velocity at a given point in time and space in a discrete approximation to the Boltzmann Equation (BE). The continuous velocity space of the BE is discretized using a quadrature rule, whose abscissae form a discrete velocity stencil for the lattice scheme. Algorithmically, the distribution is evolved following a stream and collide paradigm. In the streaming step, so-called populations (i.e. values of the distribution function) are exchanged among lattice nodes along the discrete velocities. In the collision step, the interaction of populations at the grid points is modelled by a collision rule. Macroscopic behaviour is obtained from the velocity moments of the distribution.

The method was originally intended for simulation of isothermal, incompressible flow [2], but was successfully extended to describe a wide range of complex physical phenomena such as magnetohydrodynamics [3], rarefied gas flow [4], relativistic hydrodynamics [5], combustion [6], turbulence [7], flow in porous media [8], multi-phase and multi-component flows [9, 10] and in particular thermal compressible flow [11].

Motivation

The multi-speed approach is of great interest to further broaden the range of applicability of the LBM. In this approach, a higher order approximation to the BE can be obtained systematically by increasing the order of the quadrature rule used to discretize the velocity space [12, 13]. This procedure leads to discrete velocity stencils with multiple speed levels. That is, the neighbourhood of a lattice node among which populations are exchanged in the streaming step grows beyond the nearest neighbours.

Advantages of this approach include: i) The resulting velocity stencils restore Galilean invariance [14], ii) the numerical stability of the method is increased [15] and iii) macroscopic phenomena beyond the Navier-Stokes equations can be described in terms of higher order moments of the distribution [12].

In particular, it enables simulation of thermal compressible flow, as thermal and compressibility effects are captured as higher order moments of the distribution. Multi-speed LBM has been successfully applied to the simulation of Rayleigh-Taylor instabilities and natural convection in the non-Boussinesq regime [11], Riemann problems [16] and thermal channel flow [17].

However, one major disadvantage of the multi-speed approach is that it exacerbates the task of formulating a Boundary Condition (BC): In any LBM, BCs need to be formulated in terms of populations in a way that gives rise to the desired macroscopic behaviour. This is generally not uniquely possible and in practice a trade-off between efficiency, accuracy and stability is necessary. In multi-speed LBM, several layers of nodes exhibit missing post-streaming populations, which makes the formulation of a BC even more challenging. Because of this added complexity, not much literature dealing with BCs for multi-speed lattices is available.

This work aims at filling this gap by developing new BCs suitable for usage with thermal multi-speed LBM. Two classes of BC are considered here:

First, wall boundary conditions, that are deployed at solid boundaries are considered. Such boundariesdo not permit any mass flux and should be kept at controlled macroscopic values. That is, BCs for this kind of boundary should be locally mass conserving and of Dirichlet type.

Second, Non-Reflecting Boundary Conditions (NRBCs) are considered. Such BCs are commonly posed at artificial boundaries that occur after truncation when the domain of interest is small compared to a given problems full domain or the latter is infeasibly large. That is, the BC should ideally not interact with the flow dynamics at all: Any NRBC approximates a transparent BC, for which the solution obtained in the truncated domain matches the truncated solution on the full domain. Until recently, there was no literature dealing with NRBCs for multi-speed LBM.

Structure of this thesis

This thesis is structured as follows: Chapter 2 discusses the LBMs theoretical framework and its working principle. In Chapter 3, wall BCs are examined. A few multi-speed BCs present in the literature [11, 17, 18] are described and one BC for isothermal flow [19] is extended to the thermal case. Subsequently, the accuracy of these BCs is evaluated numerically in several well-known test-beds. Chapter 4 considers NRBCs for multi-speed stencils. Several approaches to pose non-reflecting BCs for the LBM are discussed [20–22] and extended to the multi-speed case. Subsequently, they are benchmarked in selected flow configurations. A summary of the findings and possible future research directions are given in Chapter 5.

Related scientific works

The results presented in this work are based on scientific publications of the author, which in chronological order are:

A non-equilibrium bounce-back boundary condition for thermal multispeed LBM (2021) [23]

Abstract: High-order lattice Boltzmann methods provide an elegant and systematic way to incorporate thermal and compressible effects and represent a promising approach for the study of beyond-hydrodynamics regimes characterized by finite Knudsen numbers. However, the presence of multiple layers makes the definition of boundary conditions non-trivial, since one needs to define the missing information for particle distributions across several boundary layers. In this work we present a thermal extension of a recently proposed non-equilibrium bounce-back boundary condition and compare it against established algorithms by simulating standard benchmarks with wall-bounded flows.

A non-reflecting boundary condition for multispeed lattice Boltzmann methods (2022) [24]

Abstract: Artificial boundary conditions are commonly employed in numerical simulations to confine very large or unbounded domains to a computationally feasible finite domain. The implementation of an artificial boundary condition should cause no interaction with the bulk dynamics, and in particular should not create artefacts such as reflections of pressure waves. In the context of the Lattice Boltzmann Method (LBM), standard velocity or pressure boundary conditions do not fulfil this requirement. This problem is further emphasized when using multispeed LBM models, in which several layers of boundary nodes interact with the bulk dynamics. In this work, we take a first step towards the definition of a discrete artificial boundary condition for LBM based on stencils with multiple speed levels.

A Characteristic Boundary Condition for Multispeed Lattice Boltzmann Methods (2023) [25]

Abstract: We present the development of a non-reflecting boundary condition, based on the Local One-Dimensional Inviscid (LODI) approach, for Lattice Boltzmann Models working with multi-speed stencils. We test and evaluate the LODI implementation with numerical benchmarks, showing significant accuracy gains with respect to the results produced by a simple zero-gradient condition. We also implement a simplified approach, which allows handling the unknown distribution functions spanning several layers of nodes in a unified way, still preserving a comparable level of accuracy with respect to the standard formulation.

Characteristic Boundary Condition for Thermal Lattice Boltzmann Methods (2023) [26]

Abstract: We introduce a non-reflecting boundary condition for the simulation of thermal flows with the lattice Boltzmann Method (LBM). We base the derivation on the locally one-dimensional inviscid analysis, and define target macroscopic values at the boundary aiming at minimizing the effect of reflections of outgoing waves on the bulk dynamics. The resulting macroscopic target values are then enforced in the LBM using a mesoscopic Dirichlet boundary condition. We present a procedure which allows to implement the boundary treatment for both single-speed and high order multi-speed LBM models, by conducting a layerwise characteristic analysis. We demonstrate the effectiveness of our approach by providing qualitative and quantitative comparison of several strategies for the implementation of a open boundary condition in standard numerical benchmarks. We show that our approach allows to achieve increasingly high accuracy by relaxing transversal and viscous terms towards prescribed target values.

Chapter 2

Theory of the Lattice Boltzmann Method

The Lattice Boltzmann Method (LBM) has emerged as a promising tool for the simulation of fluid flow. Unlike conventional solvers in the field of Computational Fluid Dynamics (CFD), the method operates on the mesoscopic scale. That is, it evolves an approximation to the Boltzmann Equation (BE), which predicts the time evolution of a particle distribution function $f(\mathbf{x}, \mathbf{v}, t)$. This distribution gives the probability of finding a particle with velocity $\mathbf{v}$ at a position $\mathbf{x}$ at time t. The BE is difficult to solve, but includes more information than necessary to recover the correct macroscopic behaviour. In the approximation evolved by the LBM, only a finite amount of predefined discrete velocities are considered. This gives rise to a conceptually very simple scheme: By streaming fictitious particles on a discrete lattice along predefined discrete velocities and modelling their collisions on the lattice nodes $\mathbf{x}$ [27], hydrodynamics emerge at the macroscopic scale by taking discrete velocity moments of the distribution.

Historically, the first rigorous derivation of a lattice Boltzmann equation from the BE was given in [28] under the assumption of incompressible flow, which limited the methods range of applicability. Later, a systematic approach of deriving a lattice Boltzmann equation of in principle arbitrary order (in terms of retained velocity moments) was proposed [12, 13], where the BE is projected on a subspace spanned by Hermite polynomials and then truncated. This approach leads to increased numerical stability [15]. However, it requires high order quadrature rules for the discretization of the velocity space, which in turn lead to discrete velocity stencils with multiple speed levels [29].

This chapter begins with a brief description of the micro-, meso- and macroscopic scales at which fluid flow can be modelled in Sec. 2.1. Sec. 2.2 discusses the BE that governs the mesoscopic scale and its properties. In Sec. 2.3, the systematic approach to obtain a Lattice Boltzmann Method briefly outline above is explained and the working principle of the LBM is described in detail.

2.1 Models for fluid flow

In the following, three different levels of description are introduced as sketched in Fig. 2.1. Individual particles that the fluid consists of can be tracked on the microscopic scale, while continuous fields of macroscopic hydrodynamic quantities are evolved on the macroscopic scale. Between these scales lies the mesoscopic scale, where a distribution describing the location and speed of particles is tracked.

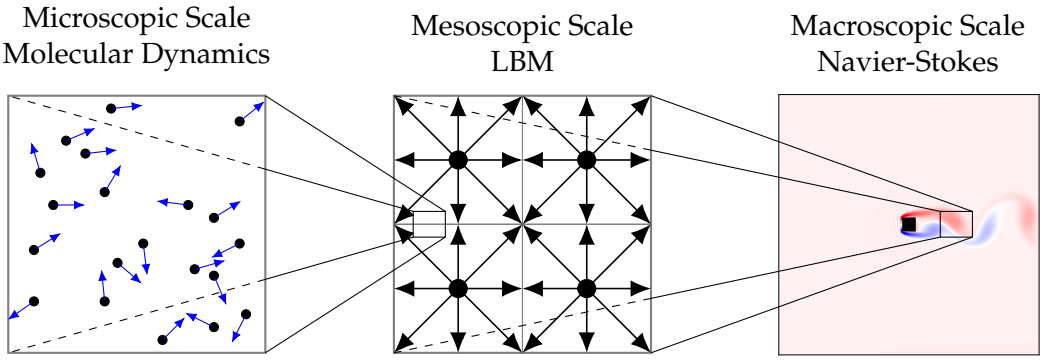

FIGURE 2.1: Visualisation of the length scales commonly used in CFD. On the macroscopic level, a continuum description of a fluid is given by the macroscopic hydrodynamic fields such as density and velocity. On the microscopic level, individual particles are tracked. The mesoscopic scale in between these two scales describes a fluid in terms of a distribution of particles.

2.1.1 Microscopic approach

On the finest level of description, it is assumed that the fluid consists of N particles that are treated as point-like structureless particles [30]. In this case, the classical Newton equations can be applied to obtain a full description of the fluids state, in terms of the position and momentum of all N particles.

While this approach gives complete information about the flow, it is only feasible in situations where the number of particles N is small. For perspective, the number of molecules in a drop of water is $N > 10^{20}$, rendering this approach infeasible for the study of phenomena on the macroscopic scale.

2.1.2 Macroscopic approach

Most conventional numerical CFD solvers rely on the macroscopic approach, where the model equations are directly formulated in terms of the (macroscopic) hydrodynamic quantities such as density $\rho(\mathbf{x}, t)$, velocity $\mathbf{u}(\mathbf{x}, t)$ and pressure $p(\mathbf{x}, t)$. In this case, the fluid is considered as a continuum. That is, in the model, there is no empty space between the particles. With this assumption, the conservation equations for mass, momentum and energy can be derived from balance equations in an infinitesimally small control volume [30]. For instance, consider such a control volume $\Delta x \Delta y$ around a point $\mathbf{x} = (x, y)$ in $D = 2$ spatial dimensions, given by

$$\Delta x \Delta y = [x - \frac{\Delta x}{2}, x + \frac{\Delta x}{2}] \times [y - \frac{\Delta y}{2}, y + \frac{\Delta y}{2}].$$

As mass can not be created or destroyed, the total mass in $\Delta x \Delta y$ can only change due to incoming and outgoing mass fluxes. That is, the rate of change of the density ρ over a time interval Δt is given by

$$\begin{aligned}\frac{\Delta\left(\rho \Delta x \Delta y\right)}{\Delta t} = &\left(\rho u_x\left(x - \frac{\Delta x}{2}, y\right) - \rho u_x\left(x + \frac{\Delta x}{2}, y\right)\right) \Delta y \\ &+ \left(\rho u_y\left(x, y - \frac{\Delta y}{2}\right) - \rho u_y\left(x, y + \frac{\Delta y}{2}\right)\right) \Delta x.\end{aligned}$$

Dividing the equation above by $\Delta x \Delta y$ and taking the continuum limit

$$\Delta t \to 0, \Delta x \to 0, \Delta y \to 0,$$

the continuity equation

$$\frac{\partial \rho}{\partial t} = -\left(\frac{\partial \rho u_x}{\partial x} + \frac{\partial \rho u_y}{\partial y}\right)$$

is obtained. Below, the conservation equations for momentum $\rho \mathbf{u}$ and the total energy density (also called energy per unit volume) $\rho E = \rho e + \frac{1}{2}\rho u^2$, where e and E are the internal energy and total energy per unit mass respectively, are given. They can be derived in a fashion similar to the continuity equation. Details on the derivations can be found in e.g. [31–33]. Note that the energy equation can equivalently be formulated in terms of e, which leads to a different formulation not considered here.

Euler equations

Depending on the fluids properties that are to be modelled, additional source terms appear in the balance equations:

In the case of an ideal fluid, there is neither viscosity nor heat conduction and only source terms due to pressure and external forces appear in the balance equations. This leads to the compressible Euler equations

$$\begin{aligned} \frac{\partial \rho}{\partial t} + \nabla \cdot (\rho \mathbf{u}) &= 0, \\ \frac{\partial (\rho \mathbf{u})}{\partial t} + \nabla \cdot \left(\rho \mathbf{u}\mathbf{u}^\top\right) &= \rho \mathbf{g} - \nabla p, \\ \frac{\partial (\rho E)}{\partial t} + \nabla \cdot (\mathbf{u}(\rho E + p)) &= \rho \mathbf{g} \cdot \mathbf{u}, \end{aligned} \tag{2.1}$$

where ∇ is the spatial gradient operator and $\mathbf{g}$ is an acceleration due to an external force.

The Euler equations (2.1) consist of $D+2$ equations for $D+3$ unknowns $\rho, \mathbf{u}, E, p$. Therefore, an additional equation of state is necessary, that relates (at least) two of the macroscopic variables. In this work, the ideal equation of state that links the fluids pressure to its temperature

$$p = \rho \frac{k_B}{m} T \tag{2.2}$$

is considered, where k_B is the Boltzmann constant and m is the particle mass.

For the description of isothermal fluid flow, the temperature is fixed to a given value T_0 and the energy equation can be dropped. For thermal fluid flow, another equation is needed to describe the temperature evolution. Assuming constant specific heat capacities $c_v = \frac{D k_B}{2m}$, the temperature is related to the energy by the simple equation [32]

$$e = c_v T. \tag{2.3}$$

Navier-Stokes-Fourier equations

The compressible Navier-Stokes-Fourier equations are an extension of the Euler equations that additionally account for diffusive effects due to the dynamic viscosity μ

and thermal conductivity κ. Thus, additional source terms appear in the macroscopic balance equations. Using Fourier's law to express the heat-flux $\mathbf{q}$ as

$$\mathbf{q} = -\kappa \nabla T,$$

the Navier-Stokes-Fourier equations read [32]

$$\begin{aligned} \frac{\partial \rho}{\partial t} &= -\nabla \cdot (\rho \mathbf{u}), \\ \frac{\partial (\rho \mathbf{u})}{\partial t} + \nabla \cdot \left(\rho \mathbf{u} \mathbf{u}^\top \right) &= \rho \mathbf{g} - \nabla p + \nabla \cdot \boldsymbol{\sigma}, \\ \frac{\partial (\rho E)}{\partial t} + \nabla \cdot (\mathbf{u}(\rho E + p)) &= \kappa \Delta T + \boldsymbol{\sigma} : (\nabla \otimes \mathbf{u}) + \rho \mathbf{g} \cdot \mathbf{u} \end{aligned} \tag{2.4}$$

where the deviatoric stress is given by

$$\boldsymbol{\sigma} = \mu \left[\nabla \mathbf{u} + \nabla \mathbf{u}^\top - \frac{2}{D} (\nabla \cdot \mathbf{u}) \mathbf{I} \right], \tag{2.5}$$

the outer product is denoted by $\otimes$ and the product of the rank D tensors $\boldsymbol{\sigma}$ and $\nabla \otimes \mathbf{u}$ denotes full contraction, i.e.

$$\boldsymbol{\sigma} (\nabla \otimes \mathbf{u}) = \sum_i \sum_j \sigma_{i,j} (\nabla \otimes \mathbf{u})_{i,j}.$$

In this work, only the case of constant transport coefficients μ, κ is considered. It is remarked that in the literature, sometimes only the momentum equation is referred to as the Navier-Stokes equation. In this work, the following nomenclature is used: The set of Eqns. (2.4) is referred to as the Navier-Stokes-Fourier equations. Dropping the energy equation, the resulting set of equations

$$\begin{aligned} \frac{\partial \rho}{\partial t} &= -\nabla \cdot (\rho \mathbf{u}), \\ \frac{\partial (\rho \mathbf{u})}{\partial t} + \nabla \cdot \left(\rho \mathbf{u} \mathbf{u}^\top \right) &= \rho \mathbf{g} - \nabla p + \nabla \cdot \boldsymbol{\sigma} \end{aligned} \tag{2.6}$$

is referred to as the Navier-Stokes equations.

This macroscopic approach is only viable if the fluid is sufficiently dense to justify the assumption of continuity. This is usually measured in terms of the Knudsen number Kn , which is defined as the ratio of the mean free path between particles L_{mfp} and a characteristic length scale L, i.e.

$$\text{Kn} = \frac{L_{\text{mfp}}}{L}. \tag{2.7}$$

A commonly adopted threshold for the continuum assumption is given by the inequality $\text{Kn} \leq 0.01$.

To recapitulate, the macroscopic approach is derived from balance equations for mass, momentum and energy in a small control volume. It can be seen as an averaging over the microscopic dynamics an therefore contains less information than a model on the microscopic scale.

2.1.3 Mesoscopic approach

The mesoscopic approach forms an intermediate level of description between the micro- and macroscopic scale. On this level, a particle distribution function $f(\mathbf{x}, \mathbf{v}, t)$ is evolved that gives the probability of finding a particle that at time t is located at position $\mathbf{x}$ and moving with velocity $\mathbf{v}$. The evolution of f is governed by the Boltzmann Equation, a derivation of which is sketched in the following as given in [34]. It is remarked that other derivations are possible [35, 36].

Consider a D-dimensional fluid consisting of N particles. At any given time t, that fluids state can be completely described by two vectors

$$\mathbf{X} = (\mathbf{x}_1, \ldots, \mathbf{x}_N), \quad \mathbf{V} = (\mathbf{v}_1, \ldots, \mathbf{v}_N)$$

that consist of the particles positions and velocities respectively. Consequently, all the information encoded in the microscopic approach can be expressed in terms of the N-particle distribution function $P_N(\mathbf{X}, \mathbf{V}, t)$, as the quantity

$$P_N(\mathbf{X}, \mathbf{V}, t)\, \mathrm{d}\mathbf{x}_1 \ldots \mathrm{d}\mathbf{x}_N\, \mathrm{d}\mathbf{v}_1 \ldots \mathrm{d}\mathbf{v}_N$$

gives the probability of finding the fluid in a state where at time t, the i-th particles location and velocity are in the infinitesimally small volumes $\mathrm{d}\mathbf{x}_i$ around $\mathbf{x}_i$ and $\mathrm{d}\mathbf{v}_i$ around $\mathbf{v}_i$ respectively.

The time evolution of P_N is governed by the Liouville equation

$$\frac{\partial P_N}{\partial t} + \sum_{i=1}^{N} \left(\mathbf{v}_i \cdot \frac{\partial P_N}{\partial \mathbf{x}_i} + \frac{\partial \mathbf{g}}{\partial t} \cdot \frac{\partial P_N}{\partial \mathbf{v}_i} \right) = 0, \tag{2.8}$$

where $\mathbf{g}$ is an uniform external acceleration. This equation is still infeasible to solve for large values of N. However, an expression for the $s-$particle distribution functions $P_N^{(s)}$ with $s < N$ can be derived from it by integrating over the positions and velocities of $N - s$ particles, i.e.

$$P_N^{(s)}(\mathbf{x}_1, \ldots, \mathbf{x}_s, \mathbf{v}_1, \ldots, \mathbf{v}_s, t) = \int P_N\, \mathrm{d}\mathbf{x}_{s+1} \ldots \mathrm{d}\mathbf{x}_N\, \mathrm{d}\mathbf{v}_{s+1} \ldots \mathrm{d}\mathbf{v}_N.$$

Integration of Eq. (2.8) over the positions and momenta of the last $N - s$ molecules gives

$$\frac{\partial P_N^{(s)}}{\partial t} + \sum_{i=1}^{s} \left(\mathbf{v}_i \cdot \frac{\partial P_N^{(s)}}{\partial \mathbf{x}_i} + \mathbf{g} \cdot \frac{\partial P_N^{(s)}}{\partial \mathbf{v}_i} \right) = (N-s)\sigma^2 \sum_{i=1}^{s} \int \left[P_N^{(s+1)'} - P_N^{(s+1)} \right] |\Delta \mathbf{v} \cdot \mathbf{n}|\, \mathrm{d}\mathbf{n}\, \mathrm{d}\mathbf{v}.$$

The term on the right-hand side in the equation above arises from the boundary conditions and describes the simultaneous collision of $s + 1$ particles: The particles are modelled as rigid spheres with radius $r > 0$, thus it follows that $P_N \equiv 0$ for $|\mathbf{x}_i - \mathbf{x}_j| < 2r, i \neq j$. Furthermore, $\Delta \mathbf{v} = \mathbf{v}_i - \mathbf{v}$ is the relative velocity with respect to $\mathbf{v}_i$, $\mathbf{n}$ is an outward normal vector to the sphere $|\mathbf{x} - \mathbf{x}_i| = 2r$ and $P_N^{(s+1)'}$ is evaluated in altered velocity arguments that can be computed assuming elastic collisions of $s + 1$ particles. Still, this expression for $P_N^{(s)}$ is not given in a closed form as it depends on $P_N^{(s+1)}$. This gives rise to a hierarchy of equations, in which the same information as in the full Liouville equation (2.8) is encoded. This hierarchy is commonly referred to as the BBGKY-hierarchy, due to the initials of Bogoliubov, Born, Green, Kirkwood and Yvon.

Discarding the impact of collisions of more than two particles at once, this hierarchy can be truncated at $s = 1$ (Stosszahlansatz) and $P_N^{(2)}$ is then modelled as

$$P_N^{(2)}(\mathbf{x}_1, \mathbf{x}_2, \mathbf{v}_1, \mathbf{v}_2) = P_N^{(1)}(\mathbf{x}_1, \mathbf{v}_1) P_N^{(1)}(\mathbf{x}_2, \mathbf{v}_2).$$

In the limit $N \to \infty$, the Boltzmann Equation (BE)

$$\frac{\partial f}{\partial t} + \mathbf{v} \cdot \nabla_x f + \mathbf{g} \cdot \nabla_v f = \Omega(f) \tag{2.9}$$

is obtained.

The left-hand side of Eq. (2.9) corresponds to the streaming of particles while its right-hand side is referred to as the collision operator. It can be expressed as [34, 36]

$$\Omega(f) = \int_{\mathbb{R}^D} \int_{\mathbb{S}^{D-1}} A(\Omega) |\mathbf{v} - \mathbf{v}_2| \left[f(\mathbf{x}, \bar{\mathbf{v}}, t) f(\mathbf{x}, \bar{\mathbf{v}}_2, t) - f(\mathbf{x}, \mathbf{v}, t) f(\mathbf{x}, \mathbf{v}_2, t) \right] d\Omega \, \mathrm{d}\mathbf{v}_2, \tag{2.10}$$

where $\mathbf{v}, \mathbf{v}_2$ are pre-collisional velocities, $\bar{\mathbf{v}}, \bar{\mathbf{v}}_2$ are post-collisional velocities and $A(\Omega)$ is the differential collision cross section that is integrated over all feasible solid angles in $D-1$-dimensional unit sphere, i.e. $\Omega \in \mathbb{S}^{(D-1)}$.

The BE derived above describes the evolution of a mono-atomic ideal gas from a kinetic point of view. That is, particles are modelled as rigid spheres that undergo elastic collisions, driving the evolution of the distribution f. In this work, only this setting is considered for simplicity. However, several generalizations exist, e.g. extensions to polyatomic gases or mixtures of different gases [34].

2.2 The Boltzmann Equation

In the previous section, the derivation of the BE (2.9) from the microscopic regime was sketched. Here, a concise introduction to the properties of the BE is given following [12] and its link to the macroscopic Navier-Stokes-Fourier equations (2.4) is discussed. A thorough discussion of the BE can be found in e.g. [34, 35].

2.2.1 The particle distribution function and its moments

The BE (2.9) governs the time evolution of the particle distribution function $f = f(\mathbf{x}, \mathbf{v}, t)$ that gives the probability of finding a particle with velocity $\mathbf{v}$ at position $\mathbf{x}$ at time t.

The relevant macroscopic hydrodynamic variables that appear in the Navier-Stokes-Fourier equations (2.4) are recovered from the velocity moments of the distribution f. By definition, the density ρ, momentum $\rho\mathbf{u}$, internal energy density ρe and total energy density ρE are obtained as

$$\rho = m \int f \, \mathrm{d}\mathbf{v}, \quad \rho\mathbf{u} = m \int f \mathbf{v} \, \mathrm{d}\mathbf{v}, \quad \rho e = \frac{m}{2} \int f \, |\hat{\mathbf{v}}|^2 \, \mathrm{d}\mathbf{v}, \quad \rho E = \frac{m}{2} \int f \, |\mathbf{v}|^2 \, \mathrm{d}\mathbf{v}. \tag{2.11}$$

In the above, and throughout this work, integrals are taken over the entire velocity space $\mathbb{R}^D$ unless specified otherwise. Furthermore, $\hat{\mathbf{v}} = \mathbf{v} - \mathbf{u}$ denotes the intrinsic velocity. An equation for the temperature T can be obtained from the definition of

internal energy density in (2.11), by making use of the relation (2.3). This gives

$$\frac{Dk_B}{2m}T = e, \tag{2.12}$$

and therefore, the temperature is proportional to the internal energy per unit mass e for the case of uniform particle mass m.

The second order momentum-flux tensor $\mathbf{P}$ is given by

$$\mathbf{P} = P_{ij} = m \int f \hat{v}_i \hat{v}_j \, d\hat{\mathbf{v}}. \tag{2.13}$$

Ignoring long range molecular interactions [12], the hydrodynamic pressure is approximated as

$$p = \frac{\mathrm{Tr}(P)}{D} = \frac{2\rho e}{D} = \rho T \frac{k_b}{m},$$

which gives again the equation of state (2.2). Finally, the heat-flux $\mathbf{q}$ is found from a contracted third order tensor $\mathbf{Q}$ as

$$\mathbf{q} = q_i = Q_{ijj} = m \int f |\hat{\mathbf{v}}|^2 \hat{v}_i \, d\hat{\mathbf{v}}, \tag{2.14}$$

where the Einstein summation convention of summing over repeated indices, e.g. $Q_{ijj} := \sum_{j=1}^{D} Q_{ijj}$ was used.

2.2.2 Collision operators

The interaction of particles on a given node $\mathbf{x}$ at a fixed time t is modelled by the collision operator (2.10). This process drives f towards a local equilibrium f^{eq}, a state in which the effects of instantaneous collisions of particles balance out and the collision operator (2.10) vanishes. For the sake of completeness, a derivation of the explicit form of f^{eq} is given following [30]. For other possible approaches, see e.g. [36].

A vanishing collision operator Eq. (2.10) implies the detailed balance condition

$$f(\mathbf{x}, \bar{\mathbf{v}}, t) f(\mathbf{x}, \bar{\mathbf{v}}_2, t) = f(\mathbf{x}, \mathbf{v}, t) f(\mathbf{x}, \mathbf{v}_2, t), \tag{2.15}$$

where $\mathbf{v}, \mathbf{v}_2$ are pre-collisional velocities and $\bar{\mathbf{v}}, \bar{\mathbf{v}}_2$ post-collisional velocities. Taking the logarithm of Eq. (2.15), it is seen that the quantity $\log f$ is an additive collision invariant, as it holds that

$$\log f(\mathbf{x}, \bar{\mathbf{v}}, t) + \log f(\mathbf{x}, \bar{\mathbf{v}}_2, t) = \log f(\mathbf{x}, \mathbf{v}, t) + \log f(\mathbf{x}, \mathbf{v}_2, t).$$

Any collision operator Ω should satisfy the conservation of mass, momentum and energy, i.e. fulfil

$$\int_{\mathbb{R}^D} \Psi \, \Omega(f) \, \mathrm{d}\mathbf{v} = 0, \quad \Psi \in \{1, m\mathbf{v}, m|\mathbf{v}|^2\}. \tag{2.16}$$

Now, $\log f$ must be a linear combination function of the invariants Ψ given by Eq. (2.16), i.e.

$$\log f^{\mathrm{eq}}(\mathbf{x}, \mathbf{v}, t) = A + B_\alpha v_\alpha + C \frac{v^2}{2},$$

where α is a spatial index and the constants A, B, C are determined by imposing the conservation of mass, momentum and energy. This results in the Maxwell-Boltzmann distribution [37]

$$f^{\mathrm{eq}}(\mathbf{x}, \mathbf{v}, t) = \rho \left(\frac{m}{2\pi k_B T} \right)^{\frac{D}{2}} \exp\left(-\frac{m}{2k_B T} |\hat{\mathbf{v}}|^2 \right). \tag{2.17}$$

The collision operator given by Eq. (2.10) accounts for all possible pairwise collisions, which makes it difficult to treat numerically. A common simplification consists of replacing it with the single relaxation time approximation

$$\Omega_{BGK}(f) = -\frac{1}{\tau}(f - f^{\mathrm{eq}}), \tag{2.18}$$

due to Bhatnagar, Gross and Krook [38] (also referred to as BGK-collision operator). In this approximation, the collision operator drives f towards the Maxwell-Boltzmann equilibrium f^{eq} with relaxation rate τ independent of the particle velocity $\mathbf{v}$. Note that equation (2.16) also holds for Ω_{BGK}, since the equilibrium conserves mass, momentum and internal energy. Now, the Boltzmann-BGK equation

$$\frac{\partial f}{\partial t} + \mathbf{v} \cdot \nabla f + \mathbf{g} \cdot \nabla_{\mathbf{v}} f = \Omega_{BGK}(f), \tag{2.19}$$

together with equations (2.11) and (2.17) forms a closed set of integro-differential equations that governs the time evolution of f [12]. In the next section, the connection between this mesoscopic and the macroscopic scale is briefly described.

2.2.3 Macroscopic limit of the Boltzmann equation

From the moments (2.11) and the collisional invariants (2.16), the following macroscopic description of the evolution of a thermal compressible fluid can be found [11]:

$$\partial_t \rho + \partial_i(\rho u_i) = 0, \quad \partial_t(\rho u_k) + \partial_i(P_{ij}) = \rho g_k, \quad \partial_t E + \frac{1}{2}\partial_i q_i = \rho g_i u_i.$$

This provides a link between the mesoscopic and macroscopic point of view. However, the above form of the macroscopic conservation equations is not closed, as the s-th equation determining the s-th velocity moment depends on the $s+1$-th moment.

One possible approach obtain a closed system on the macroscopic scale is the so-called Chapman-Enskog Expansion (CEE) [37]. It allows to compute expressions for momentum-flux $\mathbf{P}$ and heat-flux $\mathbf{q}$ in terms of density, velocity and temperature.

The CEE is essentially a perturbation expansion of the distribution f around the equilibrium f^{eq} in terms of the Knudsen number Kn. Up to a given order K, it reads

$$f = \sum_{k=0}^{K} \mathrm{Kn}^k f^{(k)} + \mathcal{O}(\mathrm{Kn}^K), \tag{2.20}$$

where $f^{(0)} = f^{\mathrm{eq}}$.

It turns out that for $K = 0$, the Euler equations (2.1) are recovered, while $K = 1$ allows a derivation of the Navier-Stokes-Fourier equations (2.4) [33]. Truncations at $K = 2$ and $K > 2$ give the Burnett and Super-Burnett equations respectively. However, these equations are quite complex and inherently unstable [39].

The procedure consists of Taylor-expanding the Boltzmann-BGK equation (2.19) and using the rescaled spatial and temporal derivatives

$$\partial_i = \mathrm{Kn}\,\partial_i, \quad \partial_t = \mathrm{Kn}\,\partial_t^{(0)} + \mathrm{Kn}^2\partial_t^{(1)}. \tag{2.21}$$

With this, equations at separated scales of orders $\mathcal{O}(\mathrm{Kn}^0), \mathcal{O}(\mathrm{Kn}^1)$ and $\mathcal{O}(\mathrm{Kn}^2)$ are obtained. Taking velocity moments on each scale gives a PDE in the macroscopic fields with respect to the decomposed derivatives (2.21). The equations on each scale can then be recombined to recover the regular time and spatial derivatives. By matching the Navier-Stokes-Fourier equations, the Chapman-Enskog procedure gives explicit expressions for the transport coefficients (i.e. viscosity and thermal conductivity) in terms of molecular parameters. A more detailed discussion can be found in [35].

In the next section, it will be shown that an approximation to the full BE is sufficient to recover the Navier-Stokes-Fourier equations. Subsequently, the discretization of the approximated BE and some properties of the LBM will be discussed.

2.3 From Boltzmann to Lattice Boltzmann

Here, the discretization of the Boltzmann Equation (BE) to establish a lattice scheme will be discussed. Note that it is common to work in rescaled units to ensure $m = k_B = 1$ (see. Sec. 2.4). Thus the particle mass and Boltzmann constant are dropped in the following.

In this section, the Gauss-Hermite approach [12, 13] to derive the LBM is presented. In this method, an approximation to the BE is obtained by truncating a projection of the BE on a basis of Hermite polynomials, a procedure discussed in Sec. 2.3.1. Subsequently, the velocity space is discretized using a Gauss quadrature rule of sufficiently high order. This is described in Sec. 2.3.2.

While alternatives such as performing a low Mach number expansion [28] exist, this approach is more systematic as it allows to in principle recover velocity moments of any given order N. Controlling the moments recovered under discretization is an important property: Consider for instance the heat-flux $\mathbf{q}$, which by (2.14) is given as a third order moment of the distribution. It does not appear in the Navier-Stokes equations (2.6) and is therefore not relevant for the macroscopic behaviour of isothermal flow. However, it appears in the Navier-Stokes-Fourier equations (2.4) and impacts the macroscopic behaviour of thermal flow.

2.3.1 Hermite expansion

In this section, the Boltzmann-BGK equation without external forcing term

$$\frac{\partial f}{\partial t} + \mathbf{v}\cdot\nabla f = \Omega_{BGK}(f) \tag{2.22}$$

is considered. The incorporation of external forces is discussed in Sec. 2.4.

In a first step, (2.22) is projected on a Hermite polynomial basis [12]. To this end, the distribution f and equilibrium distribution f^{eq} have to be expanded in Hermite polynomials. Here, several important properties of the Hermite polynomials are listed. A more detailed discussion can be found in [40].

Properties of Hermite polynomials The D-dimensional Hermite polynomial of degree n is defined as

$$\mathcal{H}^{(n)}(\mathbf{v}) = \frac{(-1)^n}{\omega(\mathbf{v})}\nabla^n\omega(\mathbf{v})$$

with weight function

$$\omega(\mathbf{v}) = \frac{1}{(2\pi)^{\frac{D}{2}}}\exp(-\frac{1}{2}|\mathbf{v}|^2).$$

The Hermite polynomials are mutually orthogonal with respect to the inner product

$$\langle f, g\rangle = \int \omega f g \ \mathrm{d}\mathbf{v}. \tag{2.23}$$

Introducing the shorthand notation $\mathcal{H}^{(n)} = \mathcal{H}^{(n)}(\mathbf{v})$, Hermite polynomials of arbitrary degree can be obtained from the recursive relation

$$\begin{cases} \mathcal{H}^{(n+1)} & = v_i\mathcal{H}^{(n)} - \boldsymbol{\delta}_i\mathcal{H}^{(n-1)}, \quad n \geq 1 \\ \mathcal{H}^{(0)} & = 1, \quad \mathcal{H}^{(1)} = \mathbf{v}. \end{cases}$$

In the above, Grad's shorthand notation [40] was used, i.e. the tensor-product is taken as the sum over all distinct index permutations. For example,

$$\boldsymbol{\delta}_i\mathcal{H}^{(n-1)} = \sum_{r=1}^{n}\delta_{ii_r}\mathcal{H}^{(n-1)}_{i_1\ldots i_{r-1}i_{r+1}\ldots i_n}, \quad n \geq 1,$$

with the Kronecker delta

$$\delta_{ij} = \begin{cases} 1, & i = j \\ 0, & i \neq j \end{cases}.$$

The explicit form of the first five Hermite polynomials is

$$\begin{aligned} &\mathcal{H}^{(0)} = 1, \quad \mathcal{H}^{(1)}_i = v_i, \quad \mathcal{H}^{(2)}_{ij} = v_iv_j - \delta_{ij}, \\ &\mathcal{H}^{(3)}_{ijk} = v_iv_jv_k - \big(\delta_{ij}v_k + \delta_{ik}v_j + \delta_{jk}v_i\big), \\ &\mathcal{H}^{(4)}_{ijkl} = v_iv_jv_kv_l - \big(\delta_{ij}v_kv_l + \delta_{ik}v_jv_l + \delta_{il}v_jv_k + \delta_{jk}v_iv_l + \delta_{jl}v_iv_k + \delta_{kl}v_iv_j\big) \\ &\qquad + \delta_{ij}\delta_{kl} + \delta_{ik}\delta_{jl} + \delta_{il}\delta_{jk}. \end{aligned}$$

Expansion of the distribution The series expansion of f in terms of Hermite polynomials reads

$$f(\mathbf{x}, \mathbf{v}, t) = \omega(\mathbf{v})\sum_{n=0}^{\infty}\frac{1}{n!}a(\mathbf{x}, t)^{(n)}\mathcal{H}^{(n)}, \tag{2.24}$$

where the expansion coefficients $a^{(n)} = a(\mathbf{x}, t)^{(n)}$ are given as

$$a^{(n)} = \int f(\mathbf{x}, \mathbf{v}, t)\mathcal{H}^{(n)} \ \mathrm{d}\mathbf{v} \tag{2.25}$$

and the product of the rank n tensors $a^{(n)}$ and $\mathcal{H}^{(n)}$ denotes full contraction. That is,

$$a^{(n)}\mathcal{H}^{(n)} = \sum_{i_1}\ldots\sum_{i_n}a^{(n)}_{i_1\ldots i_n}\mathcal{H}^{(n)}_{i_n\ldots i_1}.$$

The reason for choosing Hermite polynomials over any other expansion basis is the correspondence between the expansion coefficients $a^{(n)}$ and velocity moments of f. That is, the n-th expansion coefficient $a^{(n)}$ only depends on the velocity moments of f of up to order n, since $\mathcal{H}^{(n)}$ is a polynomial in $\mathbf{v}$. To give an example, the explicit form of the first few expansion coefficients of f is [12]

$$\begin{aligned}
a^{(0)} &= \int f \ \mathrm{d}\mathbf{v} = \rho, \\
a^{(1)} &= \int f\mathbf{v} \ \mathrm{d}\mathbf{v} = \rho\mathbf{u}, \\
a^{(2)} &= \int f(\mathbf{v}^2 - \delta) \ \mathrm{d}\mathbf{v} = \mathbf{P} + \rho(\mathbf{u}^2 - \delta), \\
a^{(3)} &= \int f(\mathbf{v}^3 - \mathbf{v}\delta) \ \mathrm{d}\mathbf{v} = \mathbf{Q} + \mathbf{u}a^{(2)} - (D-1)\rho\mathbf{u}^3, \\
a^{(4)} &= \int f(\mathbf{v}^4 - \mathbf{v}^2\delta + \delta^2) \ \mathrm{d}\mathbf{v} = \mathbf{R} - P\delta + \delta^2,
\end{aligned}$$

where $\mathbf{R} = R_{ijkl} = \int f(\mathbf{x}, \hat{\mathbf{v}}, t)\hat{v}_i\hat{v}_j\hat{v}_k\hat{v}_l \, d\hat{\mathbf{v}}$ is a fourth rank tensor. Conversely, velocity moments of up to order n are uniquely determined given coefficients $a^{(0)}, \dots a^{(n)}$, i.e. $\rho, \mathbf{u}, \mathbf{P}, \mathbf{Q}$ and $\mathbf{R}$ are determined by $a^{(i)}, i = 0, 1, 2, 3, 4$.

The truncation of the Hermite expansion (2.24) after the N-th Hermite polynomial is now given as

$$f_{(N)} = \sum_{n=0}^{N} \frac{1}{n!} a^{(n)} \mathcal{H}^{(n)}. \tag{2.26}$$

The truncated distribution given by Eq. (2.26) preserves expansion coefficients and therefore moments up to the truncation order N. This follows from the orthogonality of the Hermite polynomials with respect to the inner product given by Eq. (2.23), as for $i = 1, \dots, N$ it holds that

$$\begin{aligned}
\int f\mathcal{H}^{(i)} \, \mathrm{d}\mathbf{v} &= \int f_{(N)}\mathcal{H}^{(i)} \, \mathrm{d}\mathbf{v} + \int \omega(\mathbf{v}) \sum_{n=N+1}^{\infty} \frac{1}{n!} a^{(n)} \mathcal{H}^{(n)} \mathcal{H}^{(i)} \, \mathrm{d}\mathbf{v} \\
&= \int f_{(N)}\mathcal{H}^{(i)} \, \mathrm{d}\mathbf{v} + \int \sum_{n=N+1}^{\infty} \frac{1}{n!} a^{(n)} \langle \mathcal{H}^{(n)}, \mathcal{H}^{(i)} \rangle \, \mathrm{d}\mathbf{v} \\
&= \int f_{(N)}\mathcal{H}^{(i)} \, \mathrm{d}\mathbf{v}.
\end{aligned}$$

It is also necessary to obtain a truncated expansion of the equilibrium distribution f^{eq} when Eq. (2.22) is projected on a Hermite basis. As the Maxwell-Boltzmann equilibrium distribution f^{eq} is known, the expansion coefficients $a_{\mathrm{eq}}^{(n)}$ can be calculated

explicitly. To give an example, the first two expansion coefficients are computed as

$$\begin{aligned}
a_{\mathrm{eq}}^{(0)} &= \int_{\mathbb{R}^D} f^{\mathrm{eq}} \,\mathrm{d}\mathbf{v} = \frac{\rho}{(2\pi T)^{\frac{D}{2}}} \prod_{i=1}^{D} \int_{\mathbb{R}} \exp\left(-\frac{(v_i-u_i)^2}{2T}\right) \mathrm{d}v_i \\
&= \frac{\rho}{(2\pi T)^{\frac{D}{2}}} \prod_{i=1}^{D} (2\pi T)^{\frac{1}{2}} = \rho, \\
a_{\mathrm{eq}}^{(1)} &= \int f^{\mathrm{eq}}\, v_k \,\mathrm{d}\mathbf{v} = \frac{\rho}{(2\pi T)^{\frac{D}{2}}} \prod_{i=1}^{D} \int_{\mathbb{R}} \exp\left(-\frac{(v_i-u_i)^2}{2T}\right) \left(\delta_{ik}(v_k-1)+1\right) \mathrm{d}v_i \\
&= \frac{\rho}{(2\pi T)^{\frac{D}{2}}}\, u_k \prod_{i=1}^{D} (2\pi T)^{\frac{1}{2}} = \rho u_k.
\end{aligned}$$

Proceeding in this manner, one eventually obtains the first four expansion coefficients

$$\begin{aligned}
&a_{\mathrm{eq}}^{(0)} = \rho, \qquad a_{\mathrm{eq}}^{(1)} = \rho\mathbf{u}, \qquad a_{\mathrm{eq}}^{(2)} = \rho(\mathbf{u}^2 + (T-1)\delta), \\
&a_{\mathrm{eq}}^{(3)} = \rho(\mathbf{u}^3 + (T-1)\delta\mathbf{u}), \qquad a_{\mathrm{eq}}^{(4)} = \rho(\mathbf{u}^4 + (T-1)\delta\mathbf{u}^2 + (T-1)^2\delta^2).
\end{aligned}$$

Performing a projection of f^{eq} on the Hermite polynomials by (2.24) and truncating at $N = 2, 3, 4$ gives

$$f_{(2)}^{\mathrm{eq}} = \omega(\mathbf{v})\rho\left(1 + \mathbf{u}\cdot\mathbf{v} + \frac{1}{2}\left[(\mathbf{u}\cdot\mathbf{v})^2 - |\mathbf{u}|^2 + (T-1)(|\mathbf{v}|^2 - D)\right]\right), \tag{2.27a}$$

$$f_{(3)}^{\mathrm{eq}} = f_{(2)}^{\mathrm{eq}} + \omega(\mathbf{v})\rho\left(\frac{\mathbf{u}\cdot\mathbf{v}}{6}\left[(\mathbf{u}\cdot\mathbf{v})^2 - 3|\mathbf{u}|^2 + 3(T-1)(|\mathbf{v}|^2 - D - 2)\right]\right), \tag{2.27b}$$

$$\begin{aligned}
f_{(4)}^{\mathrm{eq}} = f_{(3)}^{\mathrm{eq}} + \omega(\mathbf{v})\rho\Bigg(\frac{1}{24}\Bigg[&(\mathbf{u}\cdot\mathbf{v})^4 - 6(\mathbf{u}\cdot\mathbf{v})^2|\mathbf{u}|^2 + 3|\mathbf{u}|^4 \\
&+ 6(T-1)\left[(\mathbf{u}\cdot\mathbf{v})^2(|\mathbf{v}|^2 - D - 2) + |\mathbf{u}|^2(2 + D - |\mathbf{v}|^2)\right] \\
&+ 3(T-1)^2(|\mathbf{v}|^4 - 2(D+2)|\mathbf{v}|^2 + (D+2)D)\Bigg]\Bigg).
\end{aligned} \tag{2.27c}$$

The procedure outlined in this section gives a systematic way to obtain an approximation to the full Boltzmann equation that retains the velocity moments of up to order N by making use of Eq. (2.26). However, the truncated Boltzmann equation still needs to be discretized. In particular, the discretization of the velocity space needs to be done in a way that ensure that the relevant moments are retained. In the next section, this issue is discussed and a strategy to choose the truncation parameter N is described.

2.3.2 Discretization of velocity space

The numerical quadrature rule use for the discretization of the velocity space must be chosen appropriately to ensure the relevant moments are captured after discretization. This section describes the procedure in greater detail. Here, it is assumed that such a quadrature rule is available. A strategy to obtain such a quadrature rule is discussed in Sec. 2.4.1.

Let M be the highest order of relevant velocity moments. As discussed in the previous section, $N \geq M$ must hold to ensure that these moments are retained in the truncated Hermite expansion of the distribution (2.26). For instance, recalling

Eqns. (2.13) and (2.14), the Navier-Stokes equations (2.6) and Navier-Stokes-Fourier equations (2.4) contain moments of up to order $M = 2$ (Pressure) and $M = 3$ (heat flux) respectively.

It can be seen from equations (2.24) and (2.25) that for any $i \in \{0, \dots, N\}$ there exists a polynomial $p^\star$ in $\mathbf{v}$ with $\deg(p^\star) \leq 2N$ that fulfils

$$f_{(N)}(\mathbf{x}, \mathbf{v}, t)\mathcal{H}^{(i)}(\mathbf{v}) = \omega(\mathbf{v})p^\star(\mathbf{x}, \mathbf{v}, t). \tag{2.28}$$

Let a Gauss-Hermite quadrature rule with degree of precision $Q \geq 2N$ consisting of weights $w_1, \dots, w_d$ and abscissae $\mathbf{v}^{(1)}, \dots, \mathbf{v}^{(d)}$ be given.

For $i \in \{0, \dots, N\}$, the expansion coefficient $a^{(i)}$ is retained under discretization as

$$\begin{aligned} a^{(i)} &= \int \omega(\mathbf{v})p^\star(\mathbf{x}, \mathbf{v}, t)\ \mathrm{d}\mathbf{v} = \sum_{j=1}^{d} w_j p^\star(\mathbf{x}, \mathbf{v}^{(j)}, t) \\ &= \sum_{j=1}^{d} \frac{w_j}{\omega(\mathbf{v}^{(j)})} f_{(N)}\left(\mathbf{x}, \mathbf{v}^{(j)}, t\right)\ \mathcal{H}^{(i)}\left(\mathbf{v}^{(j)}\right). \end{aligned}$$

This quadrature also retains the first N velocity moments of f (see (2.11))

$$\begin{aligned} \rho &= \int f(\mathbf{x}, \mathbf{v}, t)\, \mathrm{d}\mathbf{v} = \sum_{i=1}^{d} \frac{w_i}{\omega(\mathbf{v}^{(i)})} f(\mathbf{x}, \mathbf{v}^{(i)}, t) = \sum_{i=1}^{d} f_i, \\ \rho\mathbf{u} &= \int f\mathbf{v}\, \mathrm{d}\mathbf{v} = \sum_{i=1}^{d} \frac{w_i}{\omega(\mathbf{v}^{(i)})} \mathbf{v}^{(i)} f(\mathbf{x}, \mathbf{v}^{(i)}, t) = \sum_{i=1}^{d} f_i \mathbf{v}^{(i)}, \\ 2\rho e &= \int f|\hat{\mathbf{v}}|^2\, \mathrm{d}\mathbf{v} = \sum_{i=1}^{d} \frac{w_i}{\omega(\mathbf{v}^{(i)})} |\hat{\mathbf{v}}^{(i)}|^2 f(\mathbf{x}, \mathbf{v}^{(i)}, t) = \sum_{i=1}^{d} f_i |\hat{\mathbf{v}}^{(i)}|^2, \end{aligned}$$

where

$$f_i := \frac{w_i}{\omega(\mathbf{v}^{(i)})} f(\mathbf{x}, \mathbf{v}^{(i)}, t)$$

and $\hat{v}_k^{(i)} = v_k^{(i)} - u_k$.

Recalling Eq. (2.12) and the rescaling $m = k_B = 1$, the temperature T is obtained from

$$\rho D T = 2\rho e.$$

Therefore, the macroscopic quantities can be defined in terms of the discrete abscissae only:

$$\rho := \sum_{i=1}^{d} f_i, \quad \rho\mathbf{u} := \sum_{i=1}^{d} \mathbf{v}^{(i)} f_i, \quad D\rho T := \sum_{i=1}^{d} |\hat{\mathbf{v}}|^2 f_i. \tag{2.29}$$

With the discretized velocity space given by $\mathbf{v}^{(1)}, \dots, \mathbf{v}^{(d)}$, the semi-discretized Boltzmann-BGK equation reads

$$\frac{\partial f_i}{\partial t} + \mathbf{v}^{(i)} \cdot \nabla f_i = -\frac{1}{\tau}(f_i - f_i^{\mathrm{eq}}). \tag{2.30}$$

2.4 The Lattice Boltzmann Method

Since the Maxwell-Boltzmann equilibria (2.27) only depend on space and time through the macroscopic fields $\rho, \mathbf{u}$ and T, the discrete equilibrium populations can be expressed in terms of these arguments, i.e. $f_i^{\mathrm{eq}}(\mathbf{x}, t) = f_i^{\mathrm{eq}}(\rho, \mathbf{u}, T)$.

With this the fully discrete lattice Boltzmann-BGK equation

$$f_i(\mathbf{x} + \mathbf{v}^{(i)}\Delta t, t + \Delta t) = f_i(\mathbf{x}, t) - \frac{\Delta t}{\tau}\left(f_i(\mathbf{x}, t) - f_i^{\mathrm{eq}}(\rho, \mathbf{u}, T)\right) \tag{2.31}$$

is obtained after discretising space and time using uniform step sizes Δx and Δt respectively.

This equation governs the time evolution of the so-called populations $f_i(\mathbf{x}, t)$. In the Lattice Boltzmann Method (LBM), these populations are evolved following a stream and collide paradigm. In the collision step, values assigned to populations at a given node are updated according to the right-hand side of Eq. (2.31). In the streaming step, time-marching takes place as the populations are distributed along the given discrete velocities. This procedure is sketched in Fig. 2.2.

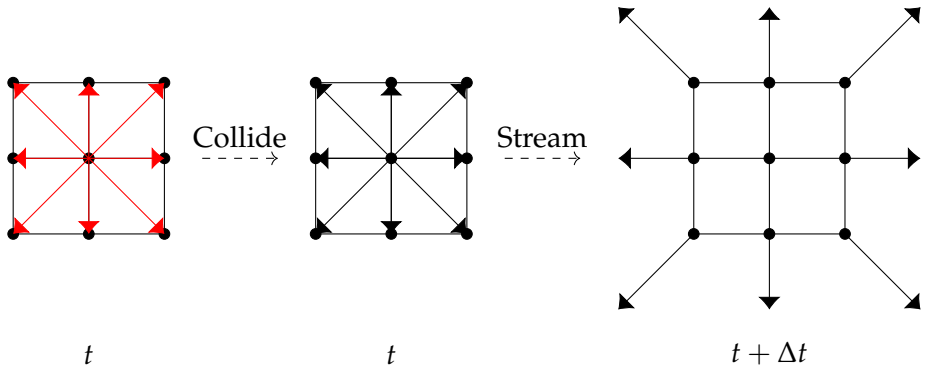

FIGURE 2.2: Illustration of the basic working principle of the LBM. At a given time t, the old populations (red) at a given node are updated according to the collision rule. The updated populations (black) are then streamed along the discrete velocities defined by the velocity stencil.

For boundary nodes $\mathbf{x}_b$ of the computational domain, the streaming step leaves at least one post-streaming population unspecified, as there is no neighbouring node the information is received from. Thus, the missing populations need to be specified by a Boundary Condition (BC). After applying BCs, the macroscopic quantities are computed on each grid node using the discrete velocity moments (2.29). This procedure is summarized as pseudocode in Algorithm 2.1.

It is seen that the only inherently non-local operation is the streaming step, which gives rise to a huge degree of parallelizability. However, the BCs may also be non-local, depending on their implementation. A brief overview of established BCs for single-speed velocity stencils is given in Sec. 2.4.2.

Algorithm 2.1 2D LBM using BGK collision operator

Inputs:
Grid size $L_x, L_y \in \mathbb{N}$, Relaxation time $\tau \in (\frac{1}{2}, \infty)$,
Maximum Iteration $N_{\text{iter}} \in \mathbb{N}$, Initial Fields: $\rho, \mathbf{u}, T$
Initialize:
iter $\leftarrow 0$
$f_i^1 \leftarrow f_i^{\text{eq}}(\rho, \mathbf{u}, T)$
while iter $\leq N_{\text{iter}}$ **do**
  for all nodes $\mathbf{x}$ and all discrete velocities **do**
    Update equilibrium distribution: $f_i^2 \leftarrow f_i^{\text{eq}}(\rho, \mathbf{u}, T)$
    Collide: $f_i^1 \leftarrow f_i^1 - \frac{\Delta t}{\tau}(f_i^1 - f_i^2)$
  end for
  for all valid nodes $\mathbf{x}$ and all valid discrete velocities **do**
    Stream: $f_i^2(\mathbf{x} + \mathbf{v}^{(i)}\Delta t, (\text{iter} + 1) \cdot \Delta t) \leftarrow f^1(\mathbf{x}, \text{iter} \cdot \Delta t)$
  end for
  for all boundary nodes $\mathbf{x}_b$ **do**
    Apply Boundary Conditions to f^2
  end for
  for all nodes **do**
    Update macroscopic quantities based on f^2
  end for
  iter $\leftarrow$ iter $+1$
end while

Exact streaming One notable feature of the LBM is the exact streaming achieved by coupling the step sizes for discretization of time, space and velocity space. That is, given a spatial step size $\Delta x^{(p)}$ m, the corresponding time step $\Delta t^{(p)}$ s is computed from the equation

$$r = \frac{\Delta x^{(p)}}{\Delta t^{(p)}}, \tag{2.32}$$

where r denotes the so-called lattice constant. The discrete velocity stencils speed of sound c_s is given as

$$c_s = \frac{\Delta t^{(p)}}{\Delta x^{(p)}} = \frac{1}{r}. \tag{2.33}$$

If the discrete abscissae of the underlying quadrature rule now fulfil

$$\mathbf{v}^{(i)} = r\mathbf{c}^{(i)} \quad \text{with } \mathbf{c}^{(i)} \in \mathbb{Z}^D \tag{2.34}$$

for all $i = 1, \ldots, d$, then by (2.31) the streaming is restricted to the discrete spatial mesh $\mathbb{Z}\Delta x^{(p)}$. The condition given by Eq. (2.34) is commonly used in the derivation of velocity stencils, see Sec. 2.4.1.

This property of exact linear advection should be contrasted with macroscopic models, where the advection term is non-linear (see (2.6)). In LBM, the non-linearity is strictly confined to the local collision step.

It is remarked that in implementations, the macroscopic quantities (2.29) are rescaled with the speed of sound (2.33) to obtain discrete moments with integer valued velocities $\mathbf{c}^{(i)}$.

Lattice Units The LBM works in dimensionless lattice units, where $\Delta t = \Delta x = 1$ is often chosen for convenience. The conversion from physical variables (superscript (p)) to dimensionless lattice variables may occur as follows: For example, the dimensional spatial step size $\Delta x^{(p)}$ (with SI unit m) can be expressed as a product of the dimensionless lattice step size Δx and a dimensional conversion factor C_x as

$$\Delta x^{(p)}\ \mathrm{m} = C_x\ \mathrm{m} \cdot \Delta x.$$

Analogously, it holds that

$$\Delta t^{(p)}\ \mathrm{s} = C_t\ \mathrm{s} \cdot \Delta t$$

and the time conversion factor C_t is uniquely determined, since the discretization of time and space and coupled via Eq. (2.32):

$$\Delta t^{(p)} = \frac{\Delta x^{(p)}}{r} = \underbrace{C_x c_s}_{=C_t}\ \mathrm{s}$$

With this, a given physical kinematic viscosity $\nu^{(p)}$ is mapped to a numerical kinematic viscosity ν as

$$\nu^{(p)}\mathrm{m}^2/\mathrm{s} = \frac{(C_x\mathrm{m})^2}{C_t\ \mathrm{s}}\nu.$$

Similarly, conversion factors C_ρ and C_T for density and temperature can be obtained. With this, the remaining conversion factors can be uniquely determined. For a more thorough discussion of unit conversion in the LBM, see [33].

Finally, it is remarked that in the LBM, one usually works in units where the Boltzmann constant k_B and molecular mass m are unity, i.e. $k_B = m = 1$. Thus, the ideal equation of state reduces to

$$P = \rho T. \tag{2.35}$$

Chapman-Enskog expansion The Chapman-Enskog Expansion (see Sec. 2.2.3) can also be applied to the discrete lattice Boltzmann-BGK equation (2.31), providing expressions for the transport coefficients in terms of lattice variables. That is, the Navier-Stokes-Fourier equations are obtained, where the numerical kinematic viscosity ν is given in terms of the relaxation time τ as

$$\nu = c_s^2(\tau - \frac{1}{2}). \tag{2.36}$$

Furthermore, the CEE provides a guideline to the choice of the truncation parameter N in the projection of f^{eq} on a Hermite basis given by Eq. (2.26).

Applying the Hermite expansion (2.24) to the ansatz (2.20), a recursive relation for the expansion coefficients $a_{k+1}^{(n)}$ of $f^{(k+1)}$ is obtained [12]:

$$a_{k+1}^{(n)} = -\tau \left[\sum_{m=0}^{k} \partial t^{(k)} a_{k-m}^{(n)} + n\nabla a_k^{(n-1)} + \nabla \cdot a_k^{(n+1)} - n\mathbf{g} a_k^{(n-1)} \right] \tag{2.37}$$

This equation shows that the n-th Hermite expansion coefficient of $f^{(k+1)}$ only depends on $(n+1)$-th order expansion coefficients of $f^{(k)}$. From this, it follows that in keeping the first N expansion coefficients of $f^{(0)} = f^{\mathrm{eq}}$, also the first $N-k$ expansion coefficients of $f^{(k)}$ are retained. In particular, for the truncation of Eq. (2.20) at

$K = 1$, the first $N + 1$ expansion coefficients should be kept in the expansion of f^{eq} to ensure that the first N expansion coefficients of $f^{(1)}$ are retained.

As the expansion coefficients uniquely determine the velocity moments, $N = M + 1$ should be chosen, where M denotes the highest order of relevant moments. That is, $N = 3$ should be chosen for problems described by the Navier-Stokes equations (2.6), as the pressure p is constructed from a second order moment. In contrast, the full Navier-Stokes-Fourier equations (2.4) require the choice $N = 4$, since the heat-flux $\mathbf{q}$ is a third order moment.

Recalling that from Eq. (2.28), it is seen that a numerical quadrature with degree of precision $Q \geq 2N$ is necessary to retain the relevant moments under discretization, it follows that a sixth order quadrature is necessary to recover the Navier-Stokes equations (2.6), while an eight order quadrature is needed for the full Navier-Stokes-Fourier equations (2.4). Before discussing an approach for the derivation of such quadrature rules in Sec. 2.4.1, the adaptation of a forcing scheme is briefly discussed.

Incorporation of external forces Until now, effects of external forces have been omitted for ease of discussion, as the continuous Boltzmann-BGK equation (2.22) lacks a forcing term when compared to Eq. (2.19), which has the additional term $\mathbf{g} \cdot \nabla_v f$.

In this work, the action of this forcing term is be absorbed in a modified collision operator [11, 41], where the equilibrium appearing in the right hand side of (2.31) is evaluated with respect to shifted velocity and temperature fields

$$\bar{f} = f^{\mathrm{eq}}(\rho, \bar{\mathbf{u}}, \bar{T}).$$

By matching the Navier-Stokes-Fourier equations in the Chapman-Enskog expansion, the shifted fields entering the equilibrium can be calculated as

$$\bar{\mathbf{u}} = \mathbf{u} + \tau \mathbf{g}, \quad \bar{T} = T + \frac{\tau(\Delta t - \tau)|\mathbf{g}|^2}{D},$$

which gives rise to the shifted lattice Boltzmann-BGK equation

$$f_i(\mathbf{x} + \mathbf{v}^{(i)}\Delta t, t + \Delta t) = f_i(\mathbf{x}, t) - \frac{\Delta t}{\tau}\left(f_i(\mathbf{x}, t) - f_i^{\mathrm{eq}}(\rho, \bar{\mathbf{u}}, \bar{T})\right) \tag{2.38}$$

after discretization.

The presence of an external acceleration implies a shift in the macroscopic velocity to correctly recover the Navier-Stokes equations (2.6) [42]. This results extends to the thermal case [11, 41], where an additional shift in the temperature T becomes necessary to give rise to the Navier-Stokes-Fourier equations. The hydrodynamic fields (indicated with the superscript H) are then given by

$$\rho^{(H)} = \rho, \quad \mathbf{u}^{(H)} = \mathbf{u} + \frac{\Delta t}{2}\mathbf{g}, \quad T^{(H)} = T + \frac{(\Delta t)^2|\mathbf{g}|^2}{4D}. \tag{2.39}$$

Evidently, this formulation recovers the case without external forces discussed previously if $\mathbf{g} \equiv 0$.

It is remarked that several other forcing strategies exist, a thorough review can be found in [43].

2.4.1 Lattice Construction

In the previous section, it was seen from Eqns. (2.28) and (2.37) that a numerical quadrature with degree of precision $Q = 6$ ($Q = 8$) order is necessary to recover the macroscopic Navier-Stokes (Navier-Stokes-Fourier) equations.

The quadrature should satisfy the following criteria: First, its weights should be non-negative to ensure numerical stability. Second, as discussed in Sec. 2.4, both Eqns. (2.32) and (2.34) should hold to ensure exact streaming. Finally, the set of discrete velocities should satisfy symmetry requirements to ensure lattice isotropy [27]: That is, it can be partitioned into r fully symmetric sets of points that share a lattice weight. Such a set consists of all possible signed permutations of a given vector.

In the following, the subscript FS is used in conjunction with a representative as a shorthand for the enumeration of all elements of the respective fully symmetric set of points. To give an example, in two spatial dimensions, it holds that

$$(1,0)_{FS} = (1,0), (-1,0), (0,-1), (0,1).$$

A lattice that fulfils these requirements is characterized by a set of integer valued velocity vectors $\mathcal{C} = \{\mathbf{c}^{(1)}, \ldots, \mathbf{c}^{(\beta)}\}$, a set of weights $\mathcal{W} = \{\omega_1, \ldots, \omega_r\}$ and a lattice constant r where the tuple $(r\mathcal{C}, \mathcal{W})$ forms a quadrature rule of degree of precision Q.

A lattice consisting of β velocities in α spatial dimensions is commonly referred to as an DαQβ lattice.

This section now discusses how such a quadrature rule can be obtained.

Construction of 1D lattices

In a one-dimensional setting, one can make use of Gauss-Hermite quadrature, which aims at finding poles $x_1, \ldots, x_n \in [a, b]$ and weights $\omega_1, \ldots, \omega_n > 0$ such that

$$\int_a^b \exp(-x^2) p(x) \, \mathrm{d}x = \sum_{i=1}^{n} \omega_i p(x_i)$$

holds for polynomials p of up to a certain degree of precision Q.

In a one-dimensional n-point Gaussian quadrature, the abscissae are given by the roots of the n-th Hermite polynomial $\mathcal{H}^{(n)}$,the corresponding weights are obtained from the formula

$$\omega_i = \frac{n!}{(n\mathcal{H}^{(n-1)}(x_i))^2} \tag{2.40}$$

and the degree of precision is $Q = 2n - 1$. By construction, those weights are strictly positive, which contributes to numerical stability of the quadrature.

Thus, it is straightforward to obtain quadratures and thus velocity stencils in the one-dimensional case.

Example: Construction of the D1Q3 lattice The appropriate discrete velocities are

$$v_1 = 0, v_{2,3} = \pm\sqrt{3},$$

i.e. the roots of the one-dimensional polynomial $\mathcal{H}^{(3)}(v) = v^3 - 3v$. The corresponding weights can be calculated from (2.40) as

$$\omega_1 = \frac{2}{3}, \; \omega_2 = \omega_3 = \frac{1}{6}.$$

Thus, the D1Q3 lattice is given as

$$\mathcal{C} = \{-1, 0, 1\} = \{0, 1_{FS}\}, \quad \mathcal{W} = \{\frac{2}{3}, \frac{1}{6}\}, \quad r = \sqrt{3}.$$

It corresponds to a quadrature with degree of precision $Q = 5$ and can therefore retain up to the second moment of the distribution function f. It is commonly used in combination with the second order Hermite expansion of the equilibrium distribution f^{eq}.

Construction of lattices in higher dimensions

In $D \geq 2$ spatial dimensions, there is no known formula for the optimal weights and abscissae.

Using a 1D quadrature along each dimension, product quadrature rules can be obtained [12]. However, they will in general not be optimal in the sense that the same degree of precision may be achieved using less abscissae.

D	2			3		
Q	5	7	9	5	7	9
$d_{\min}$	9	17	37	15	39	103

TABLE 2.1: Minimal amount of velocities $d_{\min}$ required for an on-lattice quadrature rule of order Q in D dimensions. Non-negative lattice weights and a maximum displacement of $\mathcal{M} = 3$ are required. Data taken from [44].

Instead, the so-called quadrature with prescribed abscissae [13] can be followed. First, orthonormal Hermite polynomials $\hat{\mathcal{H}}$ are computed up to a desired order M using the Gram-Schmidt procedure.

Now, a tuple $(r\mathcal{C}, \mathcal{W})$ forms a quadrature with degree of precision Q if and only if the orthonormality of $\hat{\mathcal{H}}$ is preserved, i.e. if

$$\sum_i w_i \hat{\mathcal{H}}^{(p)}(r\mathbf{c}^{(i)}) \hat{\mathcal{H}}^{(q)}(r\mathbf{c}^{(i)}) = \delta_{pq} \; \forall p, q \text{ with } p + q \leq Q \tag{2.41}$$

holds. For later reference, the following subsets of independent equations are stated:

$$\sum_i w_i \big(\hat{\mathcal{H}}^{(0)}(r\mathbf{c}^{(i)})\big)^2 = 1, \quad \sum_i w_i \big(\hat{\mathcal{H}}^{(1)}_x(r\mathbf{c}^{(i)})\big)^2 = 1, \tag{2.42a}$$

$$\sum_i w_i \big(\hat{\mathcal{H}}^{(2)}_{xx}(r\mathbf{c}^{(i)})\big)^2 = 1, \quad \sum_i w_i \big(\hat{\mathcal{H}}^{(2)}_{xy}(r\mathbf{c}^{(i)})\big)^2 = 1, \tag{2.42b}$$

$$\sum_i w_i \big(\hat{\mathcal{H}}^{(3)}_{xxx}(r\mathbf{c}^{(i)})\big)^2 = 1, \quad \sum_i w_i \big(\hat{\mathcal{H}}^{(3)}_{xxy}(r\mathbf{c}^{(i)})\big)^2 = 1, \tag{2.42c}$$

$$\sum_i w_i \big(\hat{\mathcal{H}}^{(4)}_{xxxx}(r\mathbf{c}^{(i)})\big)^2 = 1, \quad \sum_i w_i \big(\hat{\mathcal{H}}^{(4)}_{xxxy}(r\mathbf{c}^{(i)})\big)^2 = 1,$$

$$\sum_i w_i \big(\hat{\mathcal{H}}^{(4)}_{xxyy}(r\mathbf{c}^{(i)})\big)^2 = 1. \tag{2.42d}$$

In a next step, different integer velocity stencils $\mathcal{C} = \{\mathbf{c}^{(1)}, \ldots, \mathbf{c}^{(d)}\}$, consisting of sets of fully symmetric points are prescribed and an attempt is made to solve a subset of (2.41) for the lattice constant r and positive weights ω. In this way, lattices of in principle arbitrary order can be constructed.

By making use of linear programming techniques, minimal velocity stencils of fifth, seventh and ninth order for $D \in \{2,3\}$ under the additional assumption of a maximum displacement of $\mathcal{M} = 3$ can be derived [44]. They are tabulated in Tab. 2.1. Note that in Sec. 2.4, it was seen that sixth and eight order quadratures are required. However, due to the symmetry of the lattice vectors, the conditions for odd orders are fulfilled automatically [44].

The next few paragraphs include the constructions of the velocity stencils used in this work.

Construction of the D2Q9 lattice The well known D2Q9 lattice [45, 46] sketched in Fig. 2.3 can be constructed by prescribing the 9 velocities

$$\mathcal{C} = \{(0,0), (1,0)_{FS}, (1,1)_{FS}\},$$

which introduces the four unknowns $\omega_1, \omega_2, \omega_3$ and r as each symmetric group shares a weight.

FIGURE 2.3: Discrete velocities (Populations) and their indices in the D2Q9 model. The rest population is taken to have the index 9.

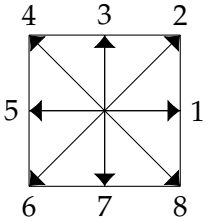

Selecting four independent equations from system (2.41), for example Eqns. (2.42a) and (2.42b), gives a closed system with explicit form

$$\begin{bmatrix} 1 & 4 & 4 \\ 0 & 2r^2 & 4r^2 \\ \frac{1}{2} & 1+(r^2-1)^2 & 2(r^2-1)^2 \\ 0 & 0 & 4r^4 \end{bmatrix} \begin{bmatrix} \omega_1 \\ \omega_2 \\ \omega_3 \end{bmatrix} = \begin{bmatrix} 1 \\ 1 \\ 1 \\ 1 \end{bmatrix} \text{ and solution } (r, \omega_1, \omega_1, \omega_3) = (\sqrt{3}, \tfrac{4}{9}, \tfrac{1}{9}, \tfrac{1}{36}).$$

Construction of the D2Q17 lattice The D2Q17 velocity stencil depicted in Fig. 2.4 can be obtained from solving the system in the six unknowns $\omega_1, \ldots, \omega_5, r$ that arises from the prescribed velocities [29]

$$\mathcal{C} = \{(0,0), (1,0)_{FS}, (1,1)_{FS}, (2,2)_{FS}, (3,0)_{FS}\}$$

and the equations (2.42a), (2.42b) and (2.42c). The solution of this system is given in Tab. 2.2.

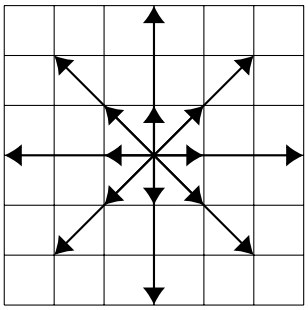

FIGURE 2.4: D2Q17 stencil.

ω_1	$\frac{575+193\sqrt{193}}{8100}$
ω_2	$\frac{3355-91\sqrt{193}}{18000}$
ω_3	$\frac{655+17\sqrt{193}}{27000}$
ω_4	$\frac{685-49\sqrt{193}}{54000}$
ω_5	$\frac{1445-101\sqrt{193}}{162000}$
r	$\left(\sqrt{\frac{5(25+\sqrt{193})}{72}}\right)^{-1}$

TABLE 2.2: Weights and lattice constant for the D2Q17 model.

Construction of the D2Q37 lattice Prescribing the 37 velocities

$$\mathcal{C} = \{(0,0), (1,0)_{FS}, (1,1)_{FS}, (2,0)_{FS}, (2,1)_{FS}, (2,2)_{FS}, (3,0)_{FS}, (3,1)_{FS}\}$$

depicted in Fig. 2.5, introduces the nine unknowns $\omega_1, \ldots, \omega_8, r$.

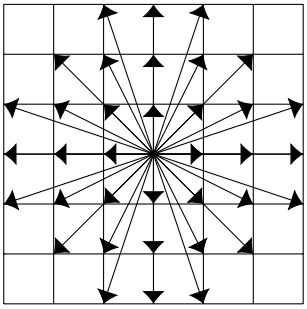

FIGURE 2.5: D2Q37 stencil.

ω_1	0.2331506691323525
ω_2	0.1073060915422190
ω_3	0.0576678598887948
ω_4	0.0142082161584507
ω_5	0.0053530490005137
ω_6	0.0010119375926735
ω_7	0.0002453010277577
ω_8	0.0002834142529941
r	1.1969797703930743

TABLE 2.3: Weights and lattice constant for the D2Q37 model.

A closed system is obtained when selecting the nine independent equations (2.42) Its solution given in Tab. 2.3.

2.4.2 Boundary Conditions

As already mentioned in the discussion of Fig, 2.2, the streaming step can not be executed for nodes that lack a corresponding neighbour to pull populations from. For any such boundary node $\mathbf{x}_b$, a Boundary Condition (BC) is needed to specify the missing populations. Any BC needs to assign values to mesoscopic populations in a way that gives rise to a desired macroscopic behaviour. However, there is no unique way to do this as the distribution f carries more information than the macroscopic Navier-Stokes or Navier-Stokes-Fourier equations. There is no objectively best BC and all approaches present in the literature have advantages and disadvantages. In this section, popular BC for single speed on-lattice stencils like the D2Q9 shown in Fig. 2.3 are briefly presented. For these stencils, information is only pulled from among the nearest neighbours.

1. Periodic BC: In the case of a fully periodic computational domain, outgoing populations are simply reinjected at the far side of the domain .

2. Equilibrium Boundary Condition (EBC): A very simple way to enforce a Dirichlet BC is to just set all the populations of $\mathbf{x}_b$ to the desired equilibrium with respect to target values $\rho_{\text{tgt}}, \mathbf{u}_{\text{tgt}}, T_{\text{tgt}}$, i.e.

   $$f_i(\mathbf{x}, t) = f_i^{\text{eq}}(\rho_{\text{tgt}}, \mathbf{u}_{\text{tgt}}, T_{\text{tgt}}).$$

   This is cheap and very simple, but completely neglects the non-equilibrium parts of the flow dynamics. However, this may be acceptable for some use cases [47].

3. Regularized Boundary Condition (RBC): From the Chapman-Enskog expansion, an explicit form of the first order correction $f^{(1)}$ is obtained [48] and all populations on the node $\mathbf{x}_b$ are set as

   $$f_i(\mathbf{x}_b, t) = f_i^{\text{eq}} + f_i^{(1)}.$$

4. Bounce-Back [49]: A popular choice to model a stationary wall, where populations leaving the computational domain are mirrored as

$$f_i(\mathbf{x}_b, t + \Delta t) = f_{\bar{i}}(\mathbf{x}_b, t),$$

where $\bar{i}$ is the index of the mirror conjugate $\mathbf{c}^{(\bar{i})} = -\mathbf{c}^{(i)}$.

5. Diffusive BC: Derived from the assumption of diffusive scattering of particles after interaction with the wall [50], this BC is sometimes referred to as kinetic BC. This means that the angle at which a particle approaches the wall does not influence its angle after reflection. Applying this to the discrete populations in the LBM gives an expression in terms of index sets of incoming populations I entering the bulk and outgoing populations O leaving the bulk. Incoming populations are then set as

$$f_i = \frac{\sum_{k \in O} f_k}{\sum_{j \in I} f_j^{\mathrm{eq}}} f_i^{\mathrm{eq}}, \quad i \in I.$$

6. Non-Equilibrium Extrapolation (NEEP): This method [51] sets unknown populations as

$$f_i = f_i^{\mathrm{eq}} + f_i^{\mathrm{neq}},$$

where the equilibrium is calculated with respect to imposed macroscopic values and the non-equilibrium part is extrapolated from the bulk.

7. Non-Equilibrium Bounce-Back (NEBB): This popular method was developed by Zou and He [52] for usage with single-speed velocity stencils for the simulation of isothermal flow. It is sometimes also referred to as Zou-He BC. In this approach, D out of the $D + 1$ scalar macroscopic quantities u_α, ρ are imposed on the boundary. The remaining quantity is not known a priori, but determined from the continuity equation. Additional constrains are obtained from the assumption of bounce-back of the non-equilibrium part of the populations normal to the boundary. Consider for instance the D2Q9 stencil (see Fig. 2.3), where the populations f_2, f_3 and f_4 are missing after the streaming step. Now, one has three equations in four unknowns, i.e. three populations and one macroscopic quantity. The additional constraint,that the non-equilibrium part of f_4 is equal to the one of f_2 is assumed, giving the closed system

$$\begin{aligned} f_2 + f_5 + f_6 &= \rho - (f_1 + f_3 + f_4 + f_7 + f_8 + f_9) \\ f_2 - f_6 &= \rho u_x - (f_1 - f_3 - f_7 + f_8) \\ f_2 + f_5 + f_6 &= \rho u_y + (f_4 + f_7 + f_8) \\ f_2 - f_2^{\mathrm{eq}} &= f_4 - f_4^{\mathrm{eq}}. \end{aligned}$$

in the four unknowns f_2, f_5, f_6, ρ is obtained. It can be solved analytically, as the form of f^{eq} is known.

A review of BCs 3 to 6 can be found in [53]. Out of the BC listed above, the regularized BC [18, 54], the diffusive BC [17] and the Zou-He BC [19, 23] have been formulated for multi-speed velocity stencils. In addition, it is straightforward to also apply the NEEP BC in this case. Details on this are reported in Chapter 3.

Chapter 3

Wall BC for multi-speed LBM

In this chapter, several approaches for posing wall BC in multi-speed thermal LBM are discussed and subsequently evaluated in numerical experiments. This kind of BC is commonly used when the interaction of a fluid with a solid obstacle needs to be modelled.

Recall from the previous section that two main reasons make the formulation of BC for multi-speed LBM non-straightforward: First, multi-speed velocity stencils have a maximum displacement of $\mathcal{M} > 1$. Thus, populations are being exchanged among the $\mathcal{M}$ nearest neighbours in the streaming step and there are $\mathcal{M}$ layers of boundary nodes where some post-streaming populations are missing. Second, BCs in the context of LBM have to be posed in terms of mesoscopic populations in a way that corresponds to the desired macroscopic behaviour. For the case of Dirichlet BC, this leads to an under-constrained system of equations and there is some freedom in choosing additional constraints, which in turn affects the overall accuracy and stability of the solver.

One important additional physical requirement that wall BCs should fulfil is the conservation of mass: As solid walls do not allow for mass flux, a proper wall BC should not alter the systems total mass.

In this work, the following naming convention is used: The layers of boundary nodes are labelled from 0 to $\mathcal{M} - 1$, beginning with the innermost layer that is adjacent to the last layer of fluid nodes. Furthermore $\mathbf{x}_b^{(k)}$ denotes a boundary node located at layer k while $\mathbf{x}_f$ represents the closest neighbouring fluid node.

The description of the BCs is kept as generic as possible to make it applicable to arbitrary velocity stencils. However, the sketches and numerical results shown in this section refer to the D2Q37 velocity stencil with a maximum displacement of $\mathcal{M} = 3$ (see Fig. 2.5). As discussed in Chapter 2, this stencil requires a minimal amount of integer-valued velocities given the requirements of a ninth order quadrature rule with non-negative weights and $\mathcal{M} \leq 3$.

In the following, two different design choices for the implementation of BCs, namely on-site and halfway BCs are explained. In Sec. 3.1, selected BCs for multi-speed LBM are listed. Sec. 3.2 gives a thermal extension of an existing multi-speed BC and Sec. 3.3 contains a numerical evaluation of selected BCs in a variety of wall-bounded thermal flow problems.

On-site approach For on-site boundaries, the boundary is located exactly on the lattice nodes as shown in Fig. 3.1. In the context of multi-speed velocity stencils, either the innermost layer ($k = 0$) is interpreted as the physical location of a boundary that spans several layers of nodes or the outermost layer ($k = 2$) is taken to correspond to the physical boundary while the inner layers of boundary nodes are viewed as fluid nodes. In this work, the former point of view is followed.

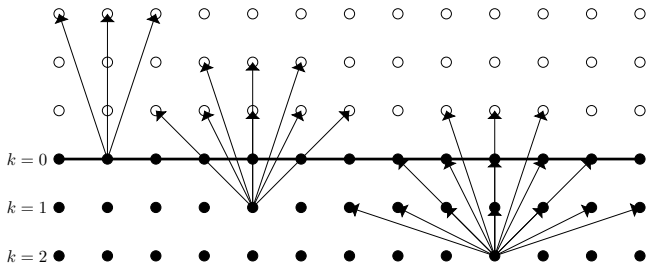

FIGURE 3.1: Sketch of the on-site boundary design for the example of a lower wall using the D2Q37 lattice. The wall (solid line) is aligned with the innermost layer of boundary nodes.

For each boundary, the three sets of indices $K^{(k)}, U^{(k)}, L^{(k)}$ can be defined, where $K^{(k)}\left(U^{(k)}\right)$ contains the known (unknown) post-streaming populations at layer k and $L^{(k)}$ contains the indices of populations pointing out of the computational domain at layer k. Considering for example a lower grid aligned boundary, the sets

$$K^{(k)} = \{\, i \mid c_y^{(i)} < \mathcal{M} - k\},\ U^{(k)} = \{\, i \mid c_y^{(i)} \geq \mathcal{M} - k\},\ L^{(k)} = \{\, i \mid c_y^{(i)} \leq k - \mathcal{M}\}$$

are obtained. With this, the mass conserving density $\rho^\star$ can be computed as

$$\rho^\star(\mathbf{x}_b^{(k)}, t + \Delta t) = \sum_{i \in L^{(k)}} f_i\left(\mathbf{x}_b^{(k)}, t\right) + \sum_{i \in K^{(k)}} f_i\left(\mathbf{x}_b^{(k)}, t + \Delta t\right), \tag{3.1}$$

i.e. the sum of the mass leaving the computational domain at time t and the known post-streaming populations at time $t + \Delta t$.

Halfway approach In the halfway approach, sketched in Fig 3.2, the boundary is located half a lattice spacing behind the last fluid node. Here, the boundary nodes are not part of the system but purely auxiliary. Letting $\mathbf{n}$ be the normal unit vector of the boundary pointing into the fluid, the missing populations on the nodes $\mathbf{x}_b^{(2)}, \mathbf{x}_b^{(1)} = \mathbf{x}_b^{(2)} + \Delta x\mathbf{n}, \mathbf{x}_b^{(0)} = \mathbf{x}_b^{(1)} + \Delta x\mathbf{n}$ are constructed from information available on these nodes. For grid aligned boundaries, this give rise to a column-wise or row-wise treatment.

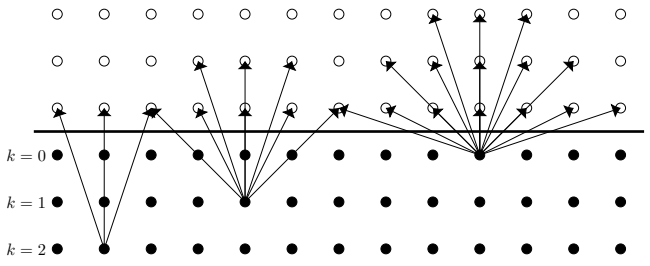

FIGURE 3.2: Sketch of the halfway boundary design for the example of a lower wall using the D2Q37 lattice. The wall (solid line) is located halfway between the innermost layer of boundary nodes and the last fluid nodes.

Conservation of mass in the bulk of the system is ensured by demanding that the mass injected into the bulk equals the mass leaving the bulk, i.e.

$$\sum_{k=0}^{\mathcal{M}-1} \sum_{j \in I_k} f_j(\mathbf{x}_b^{(k)}, t + \Delta t) = \sum_{k=0}^{\mathcal{M}-1} \sum_{j \in O_k} f_j(\mathbf{x}_b^{(k)}, t + \Delta t). \tag{3.2}$$

In the above, I_k denotes the set of indices corresponding to populations that enter the bulk from layer k. The indices of post-streaming populations that propagated from the bulk to auxiliary layer k are kept in a set O_k. Considering a lower grid aligned boundary as an example (see Fig. 3.2), the sets

$$I^{(k)} = \{\, i \mid c_y^{(i)} > k\},\ O^{(k)} = \{\, i \mid c_y^{(i)} < -k\}$$

are obtained.

Using this notation, mass-conserving halfway BCs can be constructed as follows: First, preliminary values $f_i^\star$ for the populations entering the bulk from the auxiliary boundary nodes are computed using an on-site BC. Second, the preliminary populations are weighted according to the formula

$$f_i(\mathbf{x}_b^{(k)}, t+\Delta t) = \frac{\sum_{k=0}^{\mathcal{M}-1} \sum_{j\in O_k} f_j(\mathbf{x}_b^{(k)}, t+\Delta t)}{\sum_{k=0}^{\mathcal{M}-1} \sum_{j\in I_k} f_j^\star(\mathbf{x}_b^{(k)}, t+\Delta t)} f_i^\star, \text{where } i \in I_k. \tag{3.3}$$

Finally, an instantaneous streaming step is applied to the populations obtained from Eq. (3.3), i.e.

$$f_i(\mathbf{x}_b^{(k)} + \Delta t \mathbf{c}^{(i)}, t+\Delta t) = f_i(\mathbf{x}_b^{(k)}, t+\Delta t), \quad i \in I_k.$$

Summing over all the populations set in Eq. (3.3), it is seen that indeed Eq. (3.2) holds.

Corner treatment The intersection of two straight boundaries forms a corner. As illustrated in Fig. 3.3, any corner node $\mathbf{x}_b^{(k_x,k_y)}$ can be characterized by its vertical and horizontal position k_x and k_y. Depending on the BC used, corners may require special treatment. Details on this are reported in the following sections, where selected BCs are presented.

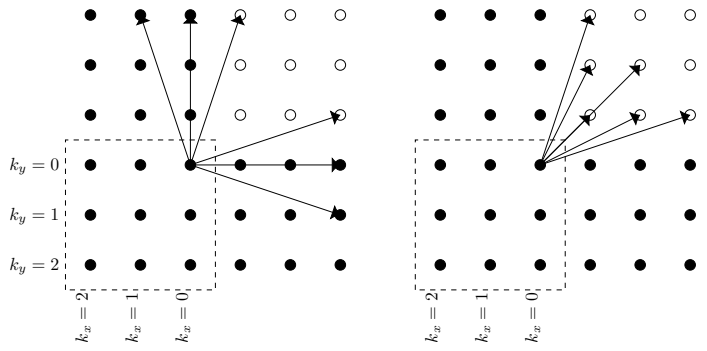

FIGURE 3.3: Lower left corner of a 2D rectangular domain and unknown post-streaming populations of the D2Q37 stencil. Filled (hollow) nodes are boundary (fluid) nodes. The left panel shows the situation for on-site boundaries, the right for halfway boundaries.

However, the same procedures as outlined above can be applied to ensure conservation of mass. Sticking with the example of a lower left corner, the relevant sets

of indices in the on-site approach become

$$K^{(k_x,k_y)} = \{\, i \mid c_y^{(i)} < \mathcal{M} - k_y,\ c_x^{(i)} < \mathcal{M} - k_x \},$$
$$U^{(k_x,k_y)} = \{\, i \mid c_y^{(i)} \geq \mathcal{M} - k_y \text{ or } c_x^{(i)} \geq \mathcal{M} - k_x \},$$
$$L^{(k_x,k_y)} = \{\, i \mid c_y^{(i)} \leq k_y - \mathcal{M} \text{ or } c_x^{(i)} \leq k_x - \mathcal{M} \}.$$

For the halfway approach, the corner is treated as a whole and the resulting expression reads

$$f_i(\mathbf{x}_b^{(k_x,k_y)}, t+\Delta t) = \frac{\sum_{k_x,k_y} \sum_{j \in O_{k_x,k_y}} f_j(\mathbf{x}_b^{(k_x,k_y)}, t+\Delta t)}{\sum_{k_x,k_y} \sum_{j \in I_{k_x,k_y}} f_j^\star(\mathbf{x}_b^{(k_x,k_y)}, t+\Delta t)} f_i^\star, \text{where } i \in I_{k_x,k_y}. \tag{3.4}$$

The relevant sets of indices are given by

$$I_{k_x,k_y} = \{\, i \mid c_x^{(i)} > k_x \text{ and } c_y^{(i)} > k_y \},\ O_{k_x,k_y} = \{\, i \mid c_x^{(i)} < -k_x \text{ and } c_y^{(i)} < -k_y \}.$$

3.1 Existing multi-speed BC

Here, several existing multi-speed BC are briefly listed. They are derived from their single-speed counterparts listed in Sec. 2.4.2.

3.1.1 Equilibrium BC

The Equilibrium BC (EBC) [47] discussed in Sec. 2.4.2 is straightforward to extend to multi-speed velocity stencils. Given target quantities $\rho_{\text{tgt}}, \mathbf{u}_{\text{tgt}}, T_{\text{tgt}}$, all populations on the boundary node $\mathbf{x}_b^{(k)}$ are set to the desired equilibrium, i.e.

$$f_i(\mathbf{x}_b^{(k)}, t+1) = f_i^{\text{eq}}(\rho_{\text{tgt}}, \mathbf{u}_{\text{tgt}}, T_{\text{tgt}}), \quad i = 1, \dots d. \tag{3.5}$$

This BC is straightforward to adapt to complex geometries. However, it incorporates no information about the non-equilibrium part of the populations.

3.1.2 Non-Equilibrium Extrapolation BC

The Non-Equilibrium Extrapolation scheme (NEEP) [51] can be viewed as an enhancement of the EBC, as in addition to supplying the equilibrium part of the distribution to all populations $f_i, i = 1, \dots d$, the non-equilibrium part $f_i^{\text{neq}} = f_i - f_i^{\text{eq}}$ is estimated by extrapolation from the bulk. While in principle all kinds of extrapolation schemes are feasible, only the case of constant extrapolation is considered here. The action of the BC can be stated as

$$f_i(\mathbf{x}_b^{(k)}, t+\Delta t) = f_i^{\text{eq}}(\rho_{\text{tgt}}, \mathbf{u}_{\text{tgt}}, T_{\text{tgt}}) + f_i^{\text{neq}}(\mathbf{x}_f, t+\Delta t), \quad k = 0, \dots, \mathcal{M}-1. \tag{3.6}$$

This version of the NEEP BC sets all post-streaming populations, overwriting known ones. This gives a Dirichlet BC, as the velocity moments of f_i^{neq} vanish. Corners are treated by posing the non-equilibrium part of the adjacent fluid node on all corner nodes (see Fig. 3.3).

3.1.3 Regularized BC

Like the NEEP scheme, the Regularized BC (RBC) aims at approximating the non-equilibrium part f_i^{neq} at the boundary [55]. It has been applied to isothermal multi-speed LBM [54] and extended to the thermal case [18], where all populations on a boundary node are set as

$$f_i(\mathbf{x}_b^{(k)}, t+\Delta t) = f_i^{\text{eq}}(\rho_{\text{tgt}}, \mathbf{u}_{\text{tgt}}, T_{\text{tgt}}) + f_i^{(1)}(\rho_{\text{tgt}}, \mathbf{u}_{\text{tgt}}, T_{\text{tgt}}, \nabla\mathbf{u}, \nabla T), \quad k = 0, \dots, \mathcal{M}-1. \tag{3.7}$$

In the above, the explicit form of the term $f_i^{(1)}$ is obtained using the Chapman-Enskog analysis.

The original literature proposes to treat the outermost layer differently than the inner layers of boundary nodes [18]. At the outermost layer, the desired macroscopic quantities are directly imposed and Eq. (3.7) is applied to all the populations. However, at the inner layers, only missing populations are replaced and the target macroscopic values are taken from the previous time step. With this design of the BC, the inner layers are interpreted as fluid layers. This procedure has the drawback that mass conservation is not satisfied at the inner layers of boundary nodes.

To be consistent with other on-site BC considered, in this work the algorithm is applied to all layers as originally intended for the outermost layer of nodes only. This has the advantage of ensuring mass conservation by choosing the density as in Eq. (3.1).

The implementation of this BC is the same for straight walls and corners apart from the way the appearing gradients are evaluated. In this work, a second order central difference is chosen whenever possible. For nodes $\mathbf{x}_b^{(\mathcal{M}-1)}$ located in the outermost layers, second order one sided finite difference stencils have been chosen.

3.1.4 Diffusive BC

The diffusive BC has been derived from kinetic theory under the assumption that the interaction with a solid wall kept at target quantities $\rho_{\text{tgt}}, \mathbf{u}_{\text{tgt}}, T_{\text{tgt}}$ causes diffuse scattering of particles [50]. It has been extended to multi-speed LBM and successfully applied beyond the hydrodynamic regime, i.e. at moderate Knudsen numbers [17]. This BC has been reported to have excellent stability properties [53] due to its firm roots in kinetic theory.

The diffusive BC is of halfway type. That is, as discussed in the beginning of this chapter, the populations that are injected into the bulk from the auxiliary node $\mathbf{x}_b^{(k)}$ are set as

$$f_i(\mathbf{x}_b^{(k)}, t+\Delta t) = \frac{\sum_{k=0}^{\mathcal{M}-1} \sum_{j\in O_k} f_j(\mathbf{x}_b^{(k)}, t+\Delta t)}{\sum_{k=0}^{\mathcal{M}-1} \sum_{j\in I_k} f_j^{\text{eq}}(\mathbf{x}_b^{(k)}, t+\Delta t)} f_i^{\text{eq}}, \text{where } i \in I_k. \tag{3.8}$$

and an instantaneous streaming step is applied to stream them into the fluid.

Note that the equation above coincides with Eq. (3.3) for the choice $f^\star = f^{\text{eq}}$. Corners are treated using this choice of $f^\star$ with Eq. (3.4).

3.1.5 Isothermal on-Site velocity BC

The isothermal on-site velocity BC is based on the Zou-He BC [52] described in Sec. 2.4.2. It has been originally introduced for the single-speed setting [56] and extended to multi-speed stencils in [19].

In this approach, the macroscopic velocity $\mathbf{u}$ is imposed at the boundary and a closed system that can be solved for the unknown populations f_i is obtained by the assumption of non-equilibrium bounce-back in conjunction with additional velocity correction terms. That is, the ansatz for the unknown post-streaming populations reads

$$f_i = f_i^{\mathrm{eq}} + f_{\bar{i}} - f_{\bar{i}}^{\mathrm{eq}} + W_i \sum_{\alpha=1}^{D} c_\alpha^{(j)} Q_\alpha, \quad i \in U^{(k)}, \tag{3.9}$$

where velocity correction terms Q_α are introduced for each spatial coordinate α and $\bar{i}$ is the index of the mirror conjugate $\mathbf{c}^{(\bar{i})} = -\mathbf{c}^{(i)}$. Inserting this ansatz in the moments (2.29) gives a closed system of $D+1$ equations in $D+1$ unknowns $\mathbf{Q}, \rho$.

Depending on the velocity stencil and order of expansion of f^{eq} (see Eqns. (2.27)), the resulting expressions for the correction terms can become quite complex. However, the resulting BC is completely local, as only information available on the current boundary node is required.

Variants of the scheme The authors in [19] discuss two different aspects in which the scheme may be varied. The first one is a *scaling* of the correction terms with the corresponding lattice weight ω_i. In Eq. (3.9), this is accounted for in the term $W_i \in \{1, \omega_i\}$. The resulting BC is referred to as scaled (unscaled) scheme for the choice $W_i = \omega_i$ ($W_i = 1$). Both approaches give a closed system of equations. However, the scaled approach has been reported to allow for a lower attainable viscosity [19] than the unscaled approach. Still, the stability range for BCs based on the assumption of non-equilibrium bounce-back is in general more narrow when compared to other BC schemes [53].

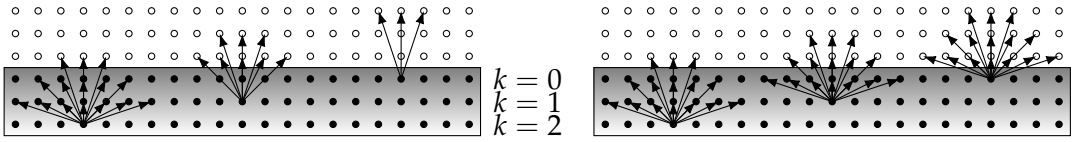

FIGURE 3.4: Internal and external population replacement strategy for a bottom boundary and the D2Q37 velocity stencil. Fluid (boundary) nodes are hollow (filled). In the internal treatment (left panel), only the unknown post-streaming populations are set. In the external treatment (right panel), all boundary layers share the same set of unknown populations. The layers are numbered in ascending order starting from the innermost.

The second variation lies in the selection of the populations that are replaced by the BC, where the authors in [19] distinguish between the *internal* and *external* treatment.

In the internal treatment, only the missing populations $f_i, i \in U^{(k)}$ are specified in each layer k (Fig. 3.4, left), which results in a different system of equations per layer. The desired macroscopic values are imposed in the outermost layer only. Linear interpolation between this layer and the last layer of fluid nodes gives target values for the remaining layers of boundary nodes. With this design choice, only the outermost layer of boundary nodes are interpreted as solid nodes while the remaining

layers are interpreted as fluid nodes. Thus, the macroscopic profiles are forced to be linear close to the boundary.

In this work, this problem is circumvented by imposing the same macroscopic quantities over all layers of boundary nodes. With this design choice, all the layers of boundary nodes are interpreted as non-fluid nodes.

It should also be mentioned that the internal approach can not be applied to arbitrary velocity stencils. Consider for instance the D2Q17 velocity stencil derived in Sec. 2.4.1. On using this stencil, the outermost layer of any straight boundary is only missing a single population and the transversal velocity correction in Eq. (3.9) will vanish, leaving not enough degrees of freedom to pose all desired macroscopic quantities.

In the external treatment, identical macroscopic values are posed at all the layers forming the boundary and missing populations from the outermost layer are replaced in all remaining layers as well (Fig. 3.4 right).

With this, it is possible to combine and implement four different NEBB BC schemes: i) unscaled-internal (NEBB-UI) ii) scaled-internal (NEBB-SI), iii) unscaled-external (NEBB-UE), iv) scaled-external (NEBB-SE).

Regardless of the chosen scheme, the NEBB ansatz (3.9) can not be directly applied to corners, as in general there are unknown populations f_i with unknown mirror conjugates $f_{\bar{i}}$. These populations are referred to as buried links [56] and are just kept at the desired target equilibrium. Subsequently, they are treated as known populations.

3.2 Thermal Non-Equilibrium Bounce-Back Boundary Condition

Here, the on-site velocity BC is extended to the thermal case, as first presented in [23]. The following ansatz for unknown populations in the boundary layer k is proposed:

$$f_i = f_i^{\mathrm{eq}} + f_{\bar{i}} - f_{\bar{i}}^{\mathrm{eq}} + W_i \left(\sum_{\alpha=1}^{D} c_\alpha^{(i)} Q_\alpha + |\mathbf{c}^{(i)}|^2 Q_t \right), \quad i \in U^{(k)}, \tag{3.10}$$

where Q_α denotes the momentum correction for the α-th vector component, and Q_t denotes a scalar temperature correction. This newly introduced correction term Q_t serves as an additional degree of freedom, which allows to prescribe the desired lattice temperature. Regardless of the chosen velocity stencil, the $d+1$ Eqns. (2.29) combined with the ansatz in Eq. 3.10 form a closed system which can be solved for the $D+1$ correction terms, yielding a Dirichlet BC.

Note that the BC as originally formulated by Lee et al. [19] does not ensure mass conservation. However, it can be ensured by rescaling all the populations with a common factor $\frac{\rho^\star}{\rho}$ to obtain the mass-conserving density $\rho^\star$. This deviates from what was reported in [23], where the excess mass $\Delta\rho = \rho^\star - \rho$ was added to the rest population f_0 to enforce the target density. On inspecting Eq. (2.29), it can be seen that manipulation of only f_0 leads to an effective temperature

$$T = T_{\mathrm{tgt}} + \frac{\Delta\rho|\mathbf{u}|}{D\rho^\star},$$

while the rescaling of all populations ensures that the imposed target values are indeed obtained.

3.3 Numerical Results

In this section, the accuracy of the BC schemes introduced in the previous section is evaluated in $D = 2$ spatial dimensions using the D2Q37 velocity stencil. The BCs ability to model grid aligned straight walls is tested by simulation of well known benchmarks, i.e. Poiseuille flow, Couette flow, and Rayleigh-Bénard convection. For these channel flows, wall BC are used at the lower and upper plates while lateral boundaries are fully periodic. Finally, the corner treatment of the different BC is inspected by simulation of a lid driven cavity flow, i.e. in a geometry where all the straight boundaries and corners are considered to be solid boundaries.

Important control parameters for the simulations are the dimensionless Reynolds, Mach and Knudsen numbers [33]

$$\mathrm{Re} = \frac{U_0 \cdot L}{\nu}, \quad \mathrm{Ma} = \frac{U_0}{c_s}, \quad \mathrm{Kn} \sim \frac{\mathrm{Ma}}{\mathrm{Re}}, \tag{3.11}$$

where L is a characteristic length scale, U_0 the characteristic flow velocity, ν the kinematic viscosity given by Eq. (2.36) and the Knudsen number defined in Eq. (2.7) is proportional to the ratio between Mach and Reynolds number. The Reynolds number is ratio of inertial to viscous forces and controls the transition between laminar and turbulent flow. To ensure a fair comparison of benchmarks when some simulations parameters are altered, the law of similarity, which states that two flows that share the same value of Re can be considered equivalent is exploited.

The Mach number is the ratio of the flow velocity to the speed of sound and can be viewed as a measure for the relevance of compressibility effects. That is, flow with $\mathrm{Ma} < 0.1$ can be considered incompressible. Finally, the limit of vanishing viscosity gives rise to numerical instability. From Eq. (2.36) a relaxation time $\tau > \frac{1}{2}$ should be chosen. A more thorough discussion of the dimensionless numbers can be found in [33]. It is remarked that usage of higher order velocity stencils contributes to a broader range of applicability [15].

Further relevant parameters used in simulations of thermal flow are the Prandtl and Eckert numbers

$$\mathrm{Pr} = \frac{\nu}{\alpha}, \quad \mathrm{Ec} = \frac{U_0^2}{c_p \, \Delta T} \tag{3.12}$$

with thermal diffusivity α, specific heat at constant pressure $c_p = \frac{D}{2} + 1$ and temperature difference between top and bottom plate ΔT. Using the single relaxation time BGK collision operator Ω_{BGK} given in Eq. (2.18), only the case $\mathrm{Pr} = 1$ is considered here.

The Poiseuille and Couette flows discussed below are channel flows with exact steady state solutions. The resulting macroscopic fields are stratified along the $x-$axis, i.e. constant for a fixed height. Thus, in order to quantify the accuracy of the BC schemes presented, it is sufficient to calculate the relative L^2-error for a generic macroscopic quantity Z with respect to the the exact solution Z^{ex} along a vertical slice through the centre of the computational domain as

$$e_Z = \sqrt{\frac{\sum_{j=1}^{L_y} \left(Z^{\mathrm{sim}}(x_i, y_j) - Z^{\mathrm{ex}}(y_j) \right)^2}{\sum_{j=1}^{L_y} \left(Z^{\mathrm{ex}}(y_j) \right)^2}}.$$

3.3.1 Thermal Poiseuille flow

Consider a fluid between two stationary horizontal plates placed at a distance H. The plates are kept at constant temperatures $T_{\text{top}}, T_{\text{bot}}$ respectively, with $\Delta T = T_{\text{top}} - T_{\text{bot}} > 0$. A constant acceleration g acts along the x-axis. The analytic steady state solutions [46] for velocity and reduced temperature $\hat{T} = \left(\frac{T - T_{\text{bot}}}{\Delta T}\right)$ read as

$$u_x^{\text{ex}}(y) = 4U_0 \cdot y(H - y) \qquad u_y^{\text{ex}} \equiv 0,$$
$$\hat{T}^{\text{ex}}(y) = \frac{y}{H} + \frac{\text{Pr} \cdot \text{Ec}}{3}\left(1 - \left(1 - \frac{2y}{H}\right)^4\right).$$

In the above, g and the maximum stream-wise velocity U_0 are linked by the relation

$$U_0 = \frac{gH^2}{8\nu}. \tag{3.13}$$

It is remarked that for stencils with a maximum displacement of $\mathcal{M}$ the channel height is given in lattice units as $H = L_y - 2\mathcal{M} + 1$, since all but the innermost layers of boundary nodes are considered auxiliary.

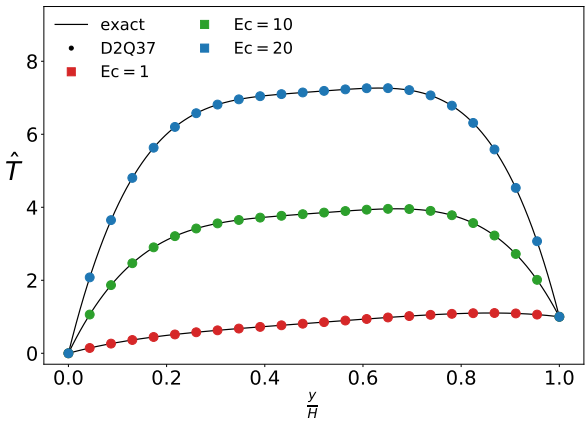

FIGURE 3.5: Steady state temperature profiles at various Eckert numbers for the D2Q37 stencil, obtained with the NEBB-SE BC. Simulation parameters are $L_y = 512, \text{Re} = 100, \text{Ma} = 0.05$ and $T_{\text{bot}} = 1$.

The various wall BCs discussed in this chapter are evaluated at the top and bottom boundaries of the rectangular computational domain. Periodic BCs are applied at the left- and right-hand side boundaries. Due to the periodicity, only $L_x = 16$ nodes were used for the rectangular $L_x \times L_y$ grid.

Note that in the following, not all relevant control parameters are explicitly given. However, the missing ones can be easily calculated from the ones present. For instance, by prescribing values for Re, Ec, Ma, T_{bot} and L_y, the values for g, ν and T_{top} are uniquely determined by Eqns. (3.11), (3.12) and (3.13).

The NEBB BC First, the different instances of the NEBB BC are analysed. In Fig. 3.5, the steady state temperature is shown for various values of Ec. Evidently, the profiles are captured accurately. To quantify this result, a grid convergence study is conducted, where the values of e_{u_x} and $e_{\hat{T}}$ are computed for several channel heights L_y. Results for the different NEBB BC versions are given in Fig. 3.6. As expected, both errors decrease as the spatial resolution is refined.

Considering e_{u_x}, it is observed that the scaling has no significant impact on the resulting accuracy. The internal versions of the NEBB BC exhibit about second order

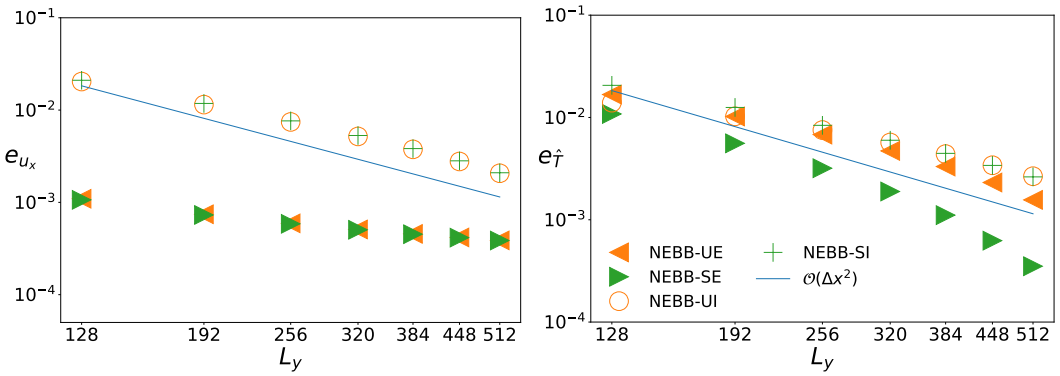

FIGURE 3.6: Grid convergence test for the thermal Poiseuille flow, comparing the different NEBB models. Shown are L^2-Errors with respect to the exact solutions for velocity (left) and reduced temperature (right). The remaining simulation parameters are $\mathrm{Re} = 100, \mathrm{Ma} = 0.05, \mathrm{Ec} = 1$ and $T_{\mathrm{bot}} = 1$.

convergence in space while the external schemes show only about first order convergence. However, usage of the latter leads to significantly better accuracy at every spatial resolution tested.

Regarding $e_{\hat{T}}$, it can be clearly seen that all versions of the NEBB exhibit about second order convergence. Again, no distinct difference between the internal approaches is observed. However, the scaled external approach leads to a significant advantage over the unscaled external approach, resulting in better accuracy for each L_y considered.

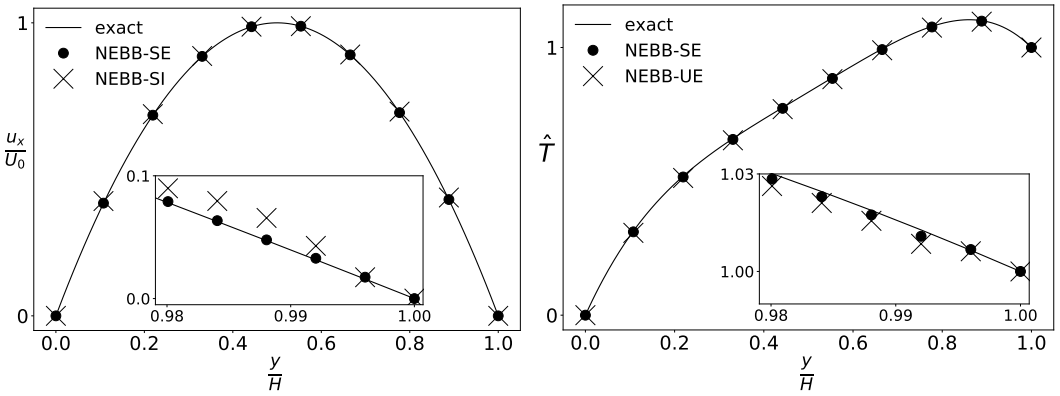

FIGURE 3.7: Left (Right): Steady state normalized velocity (reduced temperature) profile for a thermal Poiseuille flow. Inset: Zoom in the proximity of the top plate. Simulation parameters are $L_y = 256, \mathrm{Re} = 100, \mathrm{Ma} = 0.05, \mathrm{Ec} = 1$ and $T_{\mathrm{bot}} = 1$.

An explanation for this behaviour can be found in Fig. 3.7: It is observed that usage of i) internal NEBB BC causes an overshoot in the velocity near the boundary ii) unscaled NEBB BC causes a significant deviation from the correct temperature profile. Since the NEBB-SE BC gives the best results, only this version of the BC is considered in the following.

Regularized BC Next, the RBC is considered. As discussed in Sec. 3.1.3, the original formulation of the RBC [18] does not conserve total mass, since the macroscopic target density ρ_{tgt} is obtained from the previous time step for inner boundary nodes $\mathbf{x}_b^{(k)}, k \neq \mathcal{M} - 1$. This error in density pollutes the steady state temperature profiles,

which do not coincide with the analytic prediction as shown in Fig. 3.8. With the proposed version of the RBC, where mass conservation is imposed over all layers of boundary nodes, this problem does not occur.

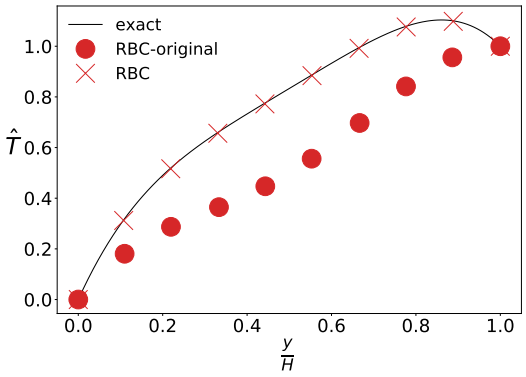

FIGURE 3.8: Steady state temperature profiles for the originally proposed RBC and the RBC adapted in this work as discussed in Sec. 3.1.3. Simulations were conducted on a $L_x \times L_y = 16 \times 256$ grid. Remaining simulation parameters are $\mathrm{Re} = 100, \mathrm{Ma} = 0.05, \mathrm{Ec} = 1$ and $T_{\mathrm{bot}} = 1$.

Grid convergence A grid convergence study is presented in Fig. 3.9, where the NEBB-SE BC is compared against other BC. Note that here, the Reynolds number is kept constant over several characteristic heights by altering the flows Mach number. This is because in general, the resulting errors curves obtained for each BC are depending on the relaxation time τ and thus the errors obtained in a steady state may increase on larger grids as τ grows past its optimal value [57]. It is observed that all the BC considered exhibit about second order convergence in e_{u_x} and e_T.

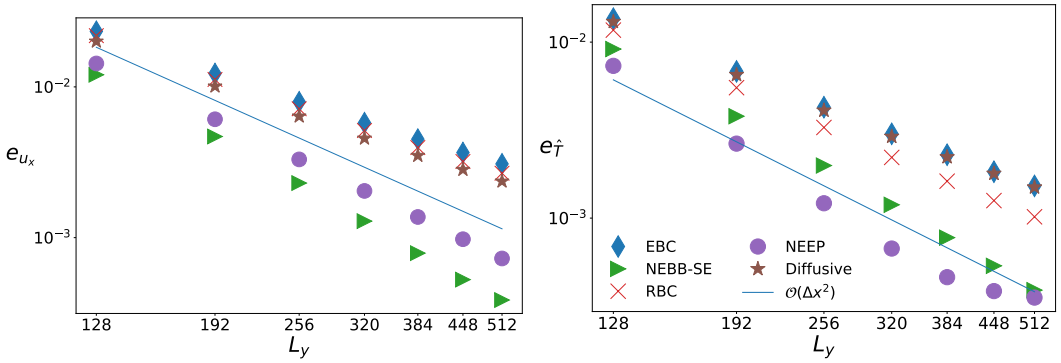

FIGURE 3.9: Grid convergence test for the thermal Poiseuille flow, comparing different BC models. Shown are L^2-Errors with respect to the exact solutions for velocity (left) and reduced temperature (right). $\mathrm{Re} = 100$ has been enforced by altering the Mach number at a fixed viscosity $\nu = 0.2$. Remaining simulation parameters are $\mathrm{Ec} = 1$ and $T_{\mathrm{bot}} = 1$.

The EBC gives the least accurate steady state profiles, which is expected as the non-equilibrium part is completely neglected. The diffusive BC and RBC yield accuracy similar to the EBC in both velocity and temperature. It can be clearly seen that the NEBB and NEEP scheme lead to the best convergence speed and highest accuracy among the BC tested. Thus, the NEEP scheme apparently gives a better estimate for f^{neq} than the RBC, while the NEBB BC benefits from minimizing the amount of information lost as not all populations on boundary nodes are replaced.

3.3.2 Thermal Couette flow

In this setup, a fluid between two horizontal plates at a distance H is considered. The top plate is moving horizontally with constant velocity U_0 and is kept at a fixed temperature T_{top}, whereas the bottom plate is stationary and kept at a temperature $T_{\text{bot}} < T_{\text{top}}$. Thus, wall BC are applied at the upper and lower straight boundaries while lateral boundaries are taken to be periodic.

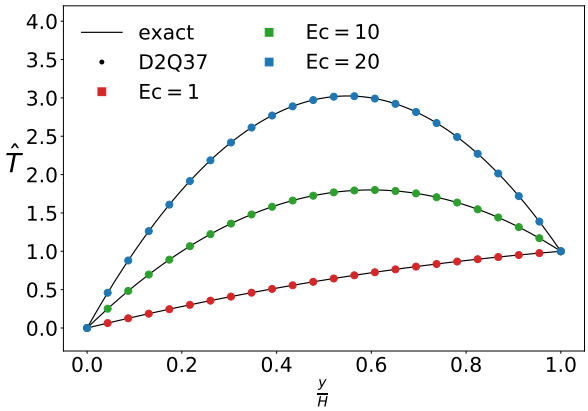

FIGURE 3.10: Steady state temperature profiles for a thermal Couette flow, simulated using the D2Q37 model with the NEBB-SE BC, for a few selected Eckert numbers. All simulations have been performed with $L_y = 512$ points, $\text{Re} = 100$, $\text{Ma} = 0.05$ and $T_{\text{bot}} = 1$.

The benchmark admits an analytic steady-state solution, here reported for the velocity, reduced temperature and density [58]:

$$u_x^{\text{ex}}(y) = U_0 \frac{y}{H}, \qquad u_y^{\text{ex}} \equiv 0,$$

$$\hat{T}^{\text{ex}}(y) = \frac{y}{H} + \frac{\text{Pr} \cdot \text{Ec}}{2} \frac{y}{H} \left(1 - \frac{y}{H}\right), \quad \rho^{\text{ex}}(y) = \frac{\rho_0 T_0}{T^{\text{ex}}(y)} \left(1 + \frac{\text{Pr}\, \text{Ma}_e^2}{3}\right),$$

where $\text{Ma}_e = \frac{U_0}{\sqrt{c_p T_0}}$ is a lattice-specific Mach number. In Fig. 3.10, a a few examples of steady state temperature profiles at different Eckert numbers obtained with the NEBB BC are shown.

Grid convergence Results of a grid convergence study are reported in Fig. 3.11. Again, simulations were conducted using $\text{Re} = 100, T_{\text{bot}} = 1, \text{Ec} = 1$ and $\nu = 0.2$. Here, second order convergence is found in the density errors e_ρ, where all the results obtained visually match. The errors $e_{\hat{T}}$ and e_{u_x} decrease at about order 1.5. Interestingly, the RBC captures the temperature profile more accurately than the NEEP BC while giving around one order of magnitude less accurate results for the velocity profiles.

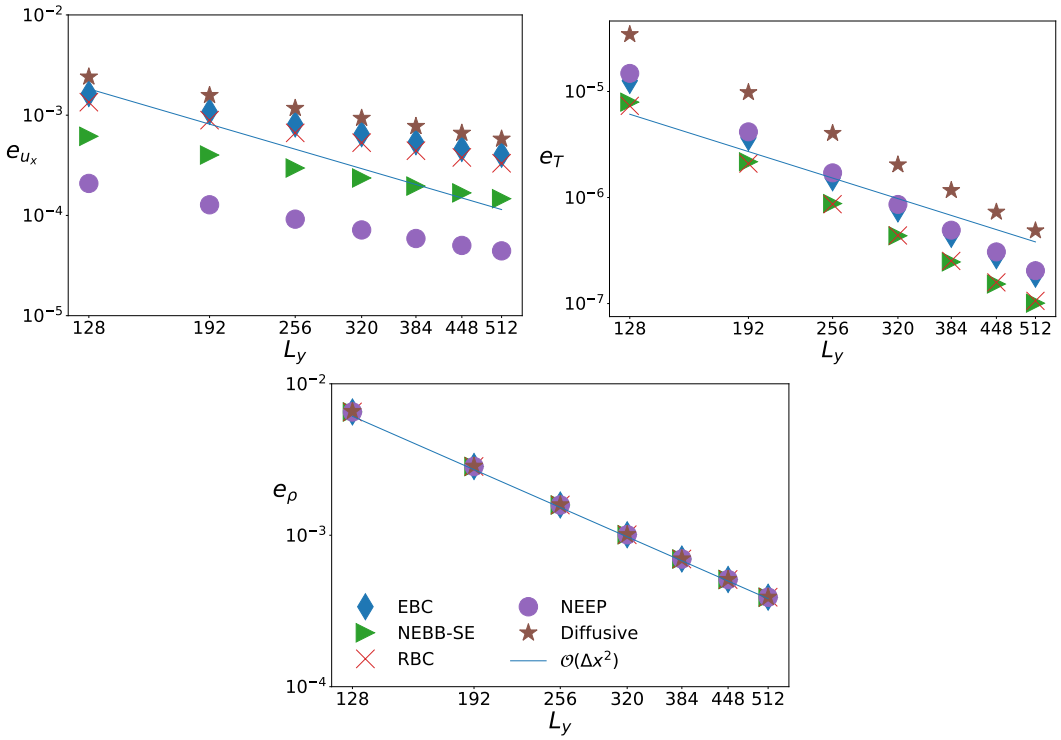

FIGURE 3.11: Grid convergence test for the thermal Couette flow, comparing different on-site BC models. Shown are L^2-Errors with respect to the exact solutions for velocity (top-left), reduced temperature (top-right) and density (bottom). All simulations have been performed with $\mathrm{Re} = 100, \mathrm{Ec} = 1, \nu = 0.2$ and $T_{\mathrm{bot}} = 1$.

3.3.3 Rayleigh-Bénard convection

In this classical setup, natural convection arises in a fluid that is heated from below and subjected to a gravity force. A fluid is confined in a channel between two horizontal walls placed at a distance H, lateral boundaries are taken to be periodic. The walls are kept at a fixed temperature, respectively T_{top} and T_{bot}, with $T_{\mathrm{top}} < T_{\mathrm{bot}}$. The gravity-like force acting along the y axis induces an acceleration $\mathbf{g} = (0, -g)^T$.

The behaviour of the system is controlled by the dimensionless Rayleigh number, that can be defined as [11]

$$\mathrm{Ra} = \frac{\mathrm{Pr}}{T_0} \frac{g H^3 \left(\Delta T - \frac{Hg}{c_p} \right)}{\nu_0^2}, \tag{3.14}$$

where the kinematic viscosity ν_0 is evaluated at the reference temperature T_0 and reference density ρ_0.

Three cases may occur on applying a small initial perturbation: First, for sufficiently low values of Ra (Fig. 3.12-left), the initial perturbations will be dampened out due to viscous dissipation and the system returns to a stationary state with a constant temperature gradient between the hot and the cold plates. Second, on increasing Ra to – or slightly above – a critical value $\mathrm{Ra}_{\mathrm{crit}}$, an onset of convection is observed that eventually saturates in a steady state (Fig. 3.12-right). Finally, when further increasing Ra the initial perturbation gives rise to a turbulent flow.

The numerical value of this critical Rayleigh number $\mathrm{Ra}_{\mathrm{crit}}$ can be obtained by performing a linear stability analysis. The most commonly studied configuration

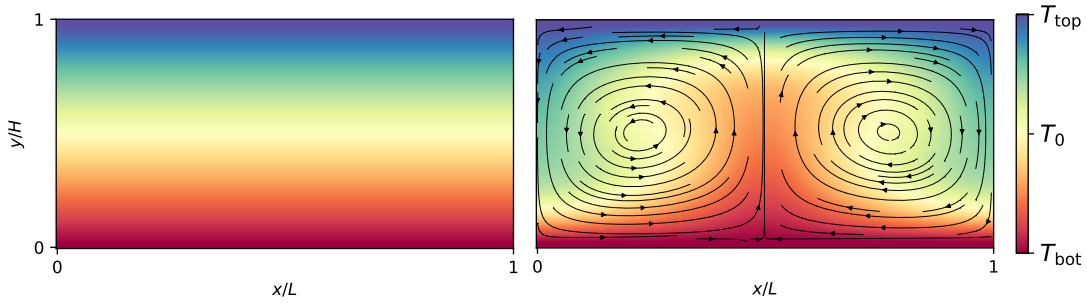

FIGURE 3.12: Example for the temperature fields in the Rayleigh-Bénard convection. Left: Stratified temperature field in the steady conductive state for low Ra. Right: Steady convective state near the critical Rayleigh number. Black lines represent the velocity streamlines.

is an incompressible fluid within the Boussinesq limit of vanishing compressibility effects [18, 59–61], where a value of $\mathrm{Ra}_{\mathrm{crit}} \approx 1707$ is obtained.

To better highlight the capabilities of multi-speed LBM, here a non-Boussinesq case with significant compressibility effects is considered. Also in this case, the critical Rayleigh number can be computed from a linear stability analysis. In the compressible regime $\mathrm{Ra}_{\mathrm{crit}}$ is found to be a function of the non-dimensional temperature jump $\Delta T/T_0$ and the polytropic index $m = g\frac{H}{\Delta T} - 1$ [62, 63]. Here, the parameters

$$\frac{\Delta T}{T_0} = 0.6, T_{\mathrm{bot}} = 0.7, T_0 = 1, m = 0.98$$

are chosen, where the analytical prediction is $\mathrm{Ra}_{\mathrm{crit}} \approx 1604$ [11].

Prediction of the critical Rayleigh number A numerical estimation of $\mathrm{Ra}_{\mathrm{crit}}$ is obtained by the following procedure: A small perturbation of the temperature field is applied close to the lower plate, where the initial temperature is set to T_{top}. In a first step, simulations with different values of Ra are conducted and the time evolution of the systems average kinetic energy $E_{\mathrm{kin}}^{\mathrm{avg}}$ is tracked. Note that due to the choice of parameters, the external acceleration g is determined by the polytropic index once a grid size is chosen. Consequently, the Rayleigh number is tuned by altering the numerical viscosity. After a start-up phase, the quantity $\log\left(E_{\mathrm{kin}}^{\mathrm{avg}}\right)$ will increase (decrease) linearly for super-critical (sub-critical) values of Ra. In a second step, the growth rate γ of $\log\left(E_{\mathrm{kin}}^{\mathrm{avg}}\right)$ is computed as a function of Ra by a linear fit. A numerical estimate for $\mathrm{Ra}_{\mathrm{crit}}$ is then given by the Rayleigh number that corresponds to zero growth rate, i.e. from the relation $\gamma(\mathrm{Ra}_{\mathrm{crit}}) = 0$.

TABLE 3.1: Numerical estimate of the critical Rayleigh number in a non-Boussinesq regime with $\Delta T/T_0 = 0.6$, $m = 0.98$. The analytic result from a linear stability analysis predicts $\mathrm{Ra}_{\mathrm{crit}} \approx 1604$.

Grid size	Diffusive	NEBB-SE	NEEP	REG	EBC
200×100	1692	1612	1618	1647	1654
400×200	1610	1613	1612	1608	1607
800×400	1603	1613	1619	1605	1593

This procedure is sketched for the NEEP BC on a 400×200 grid in Fig. 3.13, where $\mathrm{Ra}_{\mathrm{crit}} \approx 1612$ is obtained. On changing the wall BC used for the upper and lower boundaries, slightly different predictions are obtained as tabulated in Tab. 3.1.

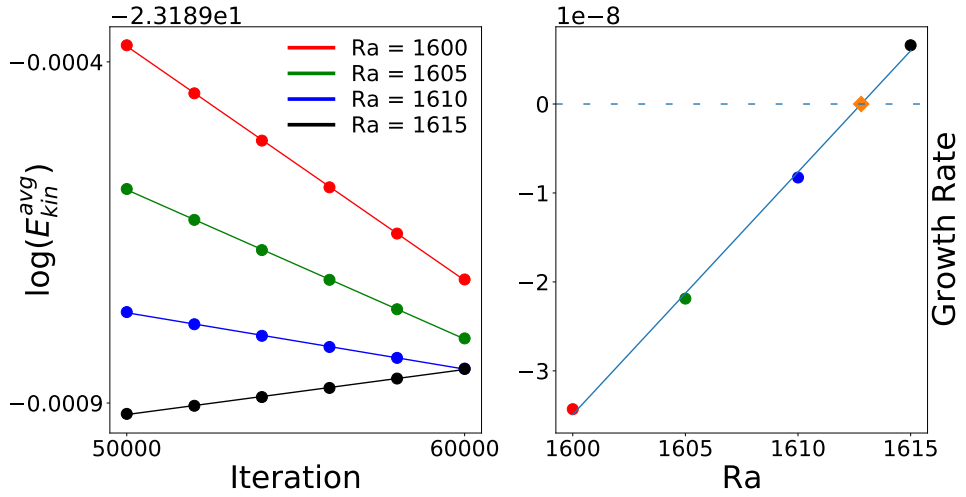

FIGURE 3.13: Sketch of the procedure of obtaining a numerical estimate for $\mathrm{Ra}_{\mathrm{crit}}$. Left panel: Linear fitting of samples of $E_{\mathrm{kin}}^{\mathrm{avg}}$ at various Rayleigh numbers. Right panel: Construction of the growth rate as a function of Ra by linear fitting of the slopes of the curves in the left panel. The value $\mathrm{Ra}_{\mathrm{crit}} \approx 1612$ is obtained (diamond node).

It is observed that the NEBB-SE and NEEP BC give the most accurate prediction on the coarsest grid tested. The predicted value of $\mathrm{Ra}_{\mathrm{crit}}$ obtained from the NEBB-SE BC is rather insensitive to the grid resolution used. On increasing the grid size, the diffusive BC and Regularized BC become slightly more accurate than both NEBB and NEEP BC while the prediction produced with the EBC appears to converge to a notably smaller number.

3.3.4 Lid driven cavity flow

In this section, a lid driven cavity flow is considered, where a homogeneous fluid contained in a square box is set into motion by a top lid that moves at a constant speed U_0. In contrast to the previous benchmarks, here all boundaries represent solid walls and thus the implementation of BCs for corners becomes necessary. The treatment of corner boundaries is still an open research problem for the LBM [33], arguably even more so for the case of multi-speed velocity stencils.

Halfway and on-site BCs In Fig. 3.14, the u_x and u_y components of the steady state velocity obtained from simulations with the NEBB-SE BC are shown. They are plotted over the vertical midplane $x = \frac{L_x}{2}$ and horizontal midplane $y = \frac{L_y}{2}$ respectively. The scheme has been implemented in both the on-site and halfway fashion. For the latter, the quantity $f^\star$ in Eq. (3.3) has been computed using the NEBB-SE scheme. For comparison, reference values from the literature that have been obtained using a multigrid method [64] are shown. The general shape of the reference solution is recovered for both approaches. However, a distinct overshoot can be seen for the on-site version of the BC. This is because the requirement of local mass conservation on the corner nodes leads to an accumulation of mass in the 'downstream' corner of the boundary corresponding to the moving lid while the 'upstream' corner nodes lack mass. This accumulation and leakage of mass is avoided when halfway schemes are used, as the outgoing mass is reinjected into the bulk in an instantaneous streaming step.

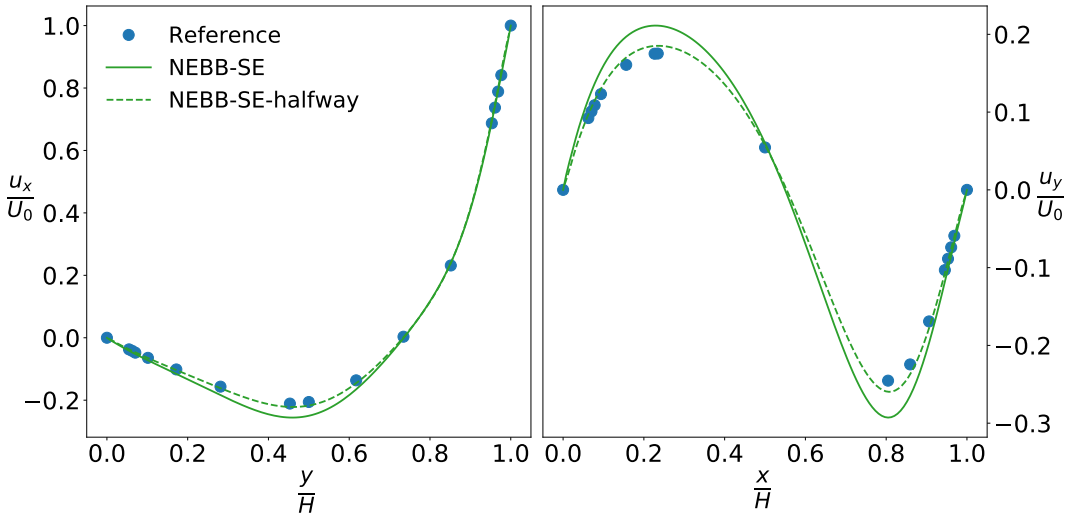

FIGURE 3.14: Effect of switching from on-site to halfway BC on an $L_x \times L_y = 133 \times 133$ grid at $\mathrm{Re} = 100$. The halfway scheme makes use of Eq. (3.3), where the quantity $f^\star$ has been computed using the NEBB-SE scheme.

To quantify the impact of the BC used, the relative errors e_{u_x}, e_{u_y} with respect to the reference solution obtained from the steady state velocity fields are given in Fig. 3.15. It is seen that for any on-site BC, the obtained accuracy is improved when the corresponding halfway scheme is used. Among the halfway BCs, the RBC gives the best accuracy with respect to e_{u_x} while e_{u_y} is minimized for the diffusive BC. This result indicates that the halfway approach is more suitable for modelling complex geometries than the on-site approach.

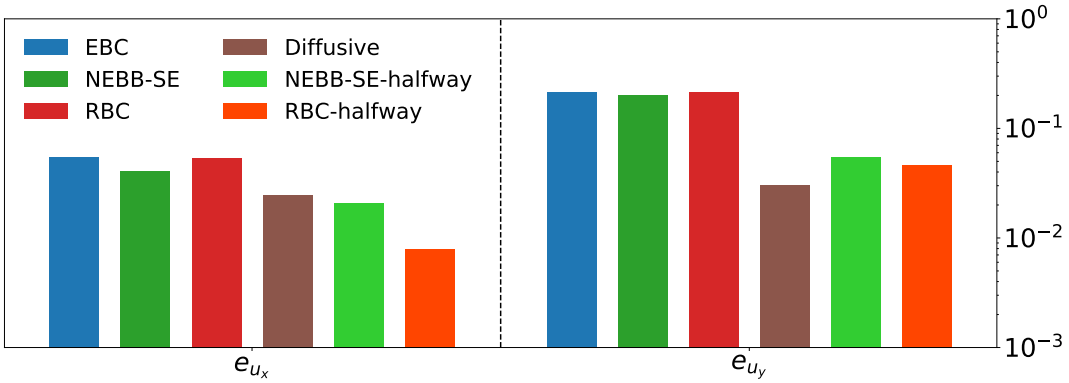

FIGURE 3.15: Deviation from reference values for various BCs. Simulations were conducted on an $L_x \times L_y = 133 \times 133$ grid at $\mathrm{Re} = 100$.

Chapter 4

Non-Reflecting Boundary Conditions

In many situations, the domain of interest is small when compared to the complete physical domain (which may be even unbounded). For reasons of computational efficiency, it is desirable to minimize the size of the computational domain. However, truncation of the physical domain leads to so-called artificial boundaries, where missing information has to be provided in a way such that the flow dynamics are not significantly altered. This is an important task, as the artificial boundary encodes no physical meaning in itself but just stems from the truncation of the domain. Therefore, the flow fields obtained on the truncated domain should match those obtained on the complete domain as closely as possible. Ideally, the solution obtained in the truncated domain coincides with the truncated solution obtained on the full domain.

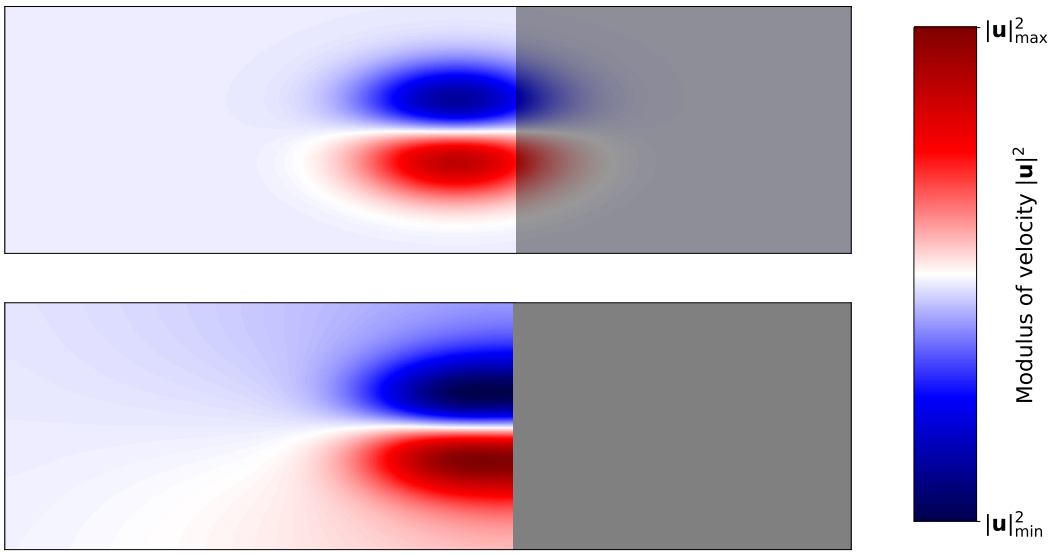

FIGURE 4.1: Snapshot of bulk dynamics affected by an extrapolation boundary condition posed at an artificial boundary.

Fig. 4.1 gives an illustration of this problem: Shown is the magnitude of the velocity of a vortex against a homogeneous background velocity in a rectangular computational domain. Due to the background velocity, the vortex propagates to the right-hand side boundary. In the upper panel, the computational domain spans the shaded and unshaded area. The domain of interest is only given by the unshaded area and thus, the shaded area may be discarded to obtain a smaller computational domain. However, posing a naive extrapolation boundary condition at the arising

artificial boundary gives rise to spurious reflections (i.e. unphysical reflections due to the boundary treatment). This significantly distorts the velocity field, as can be seen from the lower panel.

To address this problem, so-called Non-Reflecting Boundary Conditions (NRBCs) are commonly posed [65–67] at the artificial boundaries. NRBCs are tailored specifically to let outgoing information travel out of the system without polluting the flow fields in the domain of interest with unphysical reflections.

In the field of computational fluid dynamics, a first work in this direction has been conducted in [68], where absorbing boundary conditions for the wave equation have been formulated. In [69], a NRBC for one-dimensional non-linear hyperbolic systems was developed and later extended to the multidimensional case in [70]. This so-called characteristic BC was later extended to the Navier-Stokes equations [71].

In another approach, a discrete artificial BC was developed for the finite-difference discretization of the incompressible Navier-Stokes equations in [72].

A alternate strategy to avoid reflections at artificial boundaries is the perfectly matched layers approach, where the computational domain is padded with a zone of absorbing layers that is specifically designed to absorb outgoing waves. They are *perfectly* matched to the bulk in the sense that the interface between bulk and absorbing layers will not give rise to reflection. This enables usage of standard BC beyond the dampening layers, as the occurring reflections are absorbed. This approach was originally formulated for the Maxwell equations [73] and later applied to the Euler and Navier-Stokes equations [74–76]. In the nomenclature this work uses, the perfectly matched layers approach is referred to as an NRBC and the actual BC used in conjunction with it is specified.

These three approaches to posing NRBCs have been applied to isothermal, single-speed LBM in the literature. In this chapter, these techniques are reviewed their extension to thermal multi-speed LBM is discussed. Sec. 4.1 discusses the discrete artificial boundary condition [20], where the missing post-streaming populations are obtained from another LBM simulation. Sec. 4.2 deals with characteristic boundary conditions, where wave amplitude variations of incoming waves are manipulated [21]. In Sec. 4.3, the perfectly matched layers technique [22] is described for the discrete velocity Boltzmann-BGK equation. The accuracy and computational demand of these NRBCs is evaluated in Sec. 4.4.

This chapter is based on the authors following works: The multi-speed extension of the discrete artificial BC given in Sec. 4.1 is based on [24]. The application of the characteristic BC in Sec. 4.2 to isothermal flow using multi-speed velocity stencils follows [25] while the derivation of the characteristic BC for thermal flow is based on [26] .

4.1 Discrete Artificial Boundary Condition

The term Discrete Artificial Boundary Condition (DABC) is commonly used to describe any artificial BC that is derived purely on the discrete level. Doing so has the advantage of avoiding additional discretization errors.

Such a DABC has been formulated for the single-speed LBM [20, 77], where the unknown post-streaming populations are obtained from a so-called sub-problem, a separate LBM simulation that takes into account information from the previous $H_{\max}$ iterations. The natural number $H_{\max}$ is referred to as the maximum history depth and can be specified by the user. This strategy has the advantage of operating in the same mesoscopic framework as the original LBM simulation. Thus, no additional

structural assumptions have to be made. In the following, the DABC as given in [20] is described and an extension to the multi-speed [24] thermal LBM is given.

Working principle of the DABC For the sake of discussion, the right-hand side boundary of a rectangular computational grid consisting of $L_x \times L_y$ nodes is considered. The DABC introduces a sub-problem, whose computational domain is a rectangular grid consisting of $(H+1) \times L_y$ nodes, where the history depth

$$H = \min(\text{iter}, H_{\max})$$

is the number of previous time steps considered. The domains of the original problem and the sub-problem intersect in a set of nodes Γ. That is, the nodes contained in Γ form the right-hand side boundary of the original LBM domain as well as the left-hand side boundary of the sub-problem.

Algorithm 4.1 Right LBM sub-problem for time level t_k

Inputs:
  history depth H, grid $(\mathcal{M}(H+1) \times L_y)$, τ, initial fields: $\rho, \mathbf{u}, T$
Initialize:
  Initialize f^{sub}, set $\text{iter}_{\text{sub}} = 1$ and $f^{\text{sub}}(x_\gamma, t_{k-H}) = f(x_\gamma, t_{k-H})$
while $\text{iter}_{\text{sub}} \leq$ H **do**
  for all grid points **do**
    Update equilibrium distribution f^{eq}
    Collide & Stream
    if $\text{iter}_{\text{sub}} <$ H **then**
      Left BC of sub-problem: $f_i^{\text{sub}}(x_\gamma, t_{k-H+\text{iter}_{\text{sub}}}) = f_i(x_\gamma, t_{k-H+\text{iter}_{\text{sub}}})$
    else
      Right BC of original problem: $f_i(x_\gamma, t_k) = f_i^{\text{sub}}(x_\gamma, t_k)$
    end if
    Update macroscopic quantities
  end for
  $\text{iter}_{\text{sub}} = \text{iter}_{\text{sub}} + 1$
end while

Initialization Considering the time t_k, the nodes $x_\gamma \in \Gamma$ are initialized with known previous populations from time t_{k-H}. For the remaining nodes of the sub-problem, three different initialization strategies are considered:

In the first one, the sub-problems are initialized as

$$f_i^{\text{sub}}(\mathbf{x}, t_{k-H}) = f_i^{\text{eq}}(\rho_0, \mathbf{u}_0), \tag{4.1}$$

where the macroscopic fields $\rho_0, \mathbf{u}_0$ represent the fluids homogeneous state outside of the region of interest. The DABC with this initialization is referred to as DABC-A.

The second strategy, labelled DABC-B, initializes the sub-problem using a constant extrapolation (along the outward pointing normal vector $\mathbf{n}$ of the original grid) from the node x_γ

$$f_i^{\text{sub}}(\mathbf{x}, t_{k-H}) = f_i(\mathbf{x}_\gamma, t_{k-H}). \tag{4.2}$$

Both of these approaches have been suggested in [20]. They are combined in a third one, where the populations at the intersection Γ are taken from the bulk at time t_{k-H} and the populations at the far side of the sub-problems grid (e.g. the right-hand

side boundary of right sub-problem) are set to a given equilibrium by Eq. (4.1). The populations at the intermediate layers are then set to an equilibrium with respect to interpolated macroscopic values

$$f_i^{\text{sub}}(\mathbf{x}_b^{(\mathcal{M}-1)} + k\mathbf{n}, t_{k-H}) = f_i^{\text{eq}}(\rho^\star, \mathbf{u}^\star), \tag{4.3}$$

where $\mathbf{n}$ is the normal vector pointing inside the sub-problems grid and

$$Z^\star = Z(\mathbf{x}_b^{(\mathcal{M}-1)}, t_{k-H}) - \frac{k}{L_x^{\text{sub}}}\left(Z(\mathbf{x}_b^{(\mathcal{M}-1)}, t_{k-H}) - Z_0\right), \quad Z \in \{\rho, u_x, u_y\}.$$

This scheme will be referred to as DABC-C.

Evolving the sub-problem After initialization, the sub-problem is evolved with the usual LBM scheme for H iterations. In each iteration, the previously computed populations $f_i(x_\gamma, t_{k-H+\text{iter}})$ of the original problem are used as a BC on Γ. Finally, the unknown populations of the original problem are obtained as the corresponding post-streaming populations of the sub-problem located at the intersection Γ at time t_k, i.e. $f_i(x_\gamma, t_k)$. This procedure is summarized in Algorithm 4.1.

It should be noted that the boundary treatment on the right-hand side boundary of the sub-problem has no impact on the simulation, as no error will propagate to Γ over the course of H iterations.

DABC for multi-speed thermal LBM As the DABC operates directly on the mesoscopic scale, it is straightforward to deploy for simulations of thermal flow. This is simply done by also evolving the temperature T as a moment of the distribution and accounting for its impact in the calculation of f^{eq}. When building a multi-speed sub-problem, two technical changes are necessary. First, the size of the sub-problems grid needs to be adapted. To ensure that no information from the far side boundaries reaches Γ over H iterations, $\mathcal{M} \cdot H$ layers of nodes are now introduced beyond Γ. Second, the intersection Γ now consists of $\mathcal{M}$ layers of nodes, namely the layers of boundary nodes of the original grid. Both aspects are depicted in Fig. 4.2.

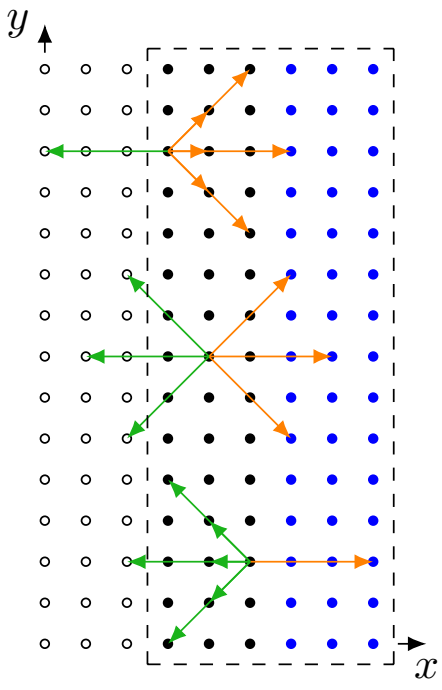

FIGURE 4.2: Sketch of populations assigned in a sub-problem for a right-hand side boundary using the D2Q17 stencil. The dashed rectangle contains the sub-problems domain for $H_{\text{max}} = 1$, consisting of the original problems boundary nodes $\mathbf{x}_b \in \Gamma$ (black nodes) and $\mathcal{M} = 3$ layers of auxiliary nodes (blue nodes). Hollow nodes are fluid nodes for the original problem. In each iteration of the sub-problem, orange populations are taken as a BC from the history of the original lattice at time $t_{k-H+\text{iter}}$. Green populations are the final output of the sub-problem at time level t_k.

History depth and computational cost The value of $H_{\max}$ controls the amount of previous time steps that contribute information to the construction of boundary populations at a given time. In the extreme case, if the maximum history depth equals the maximum iteration count, i.e. $H_{\max} = N_{\text{iter}}$, the DABCs only source of error lies in the initialization of the sub-problems. If exact information about the initial state of the fluid outside of the region of interest at initial time t_0 is available, the artificial boundary will not introduce any error. However, the computational effort required for this is infeasibly large in practice: Considering a sub-problem on the right-hand side boundary of the computational domain, H iterations of the sub-problem have to be performed on an auxiliary domain of size $\mathcal{M}(H+1) \times L_y$ in the H-th iteration of the original problem. Thus, the DABC requires a total of

$$A = L_y \cdot H \cdot \mathcal{M} \cdot (H+1)$$

additional stream and collide operations in the H-th iteration. That is, the computational cost grows quadratically over the iterations and becomes infeasible for long term simulations.

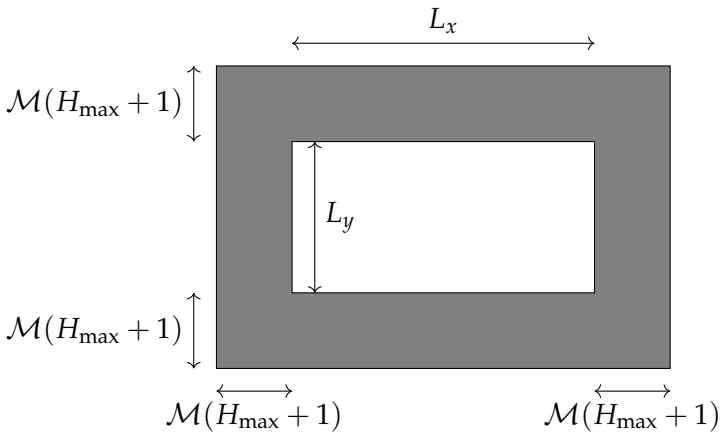

FIGURE 4.3: Sketch of the sub-problem geometry and amount of necessary additional nodes for a rectangular computational domain with open boundaries only. The original domain (white rectangle) consists of $L_x \times L_y$ nodes and is enclosed by the sub-problems grid (grey).

The situation is even more demanding when all face and corner boundaries are to be equipped with the DABC. In this case, the computational grid of the sub-problem encloses the domain of interest, see Fig. 4.3. Thus, in each LBM iteration, H iterations on a sub-problem grid consisting of

$$B = 2\mathcal{M}(H+1)(L_x + L_y) + 4\mathcal{M}(H+1)^2$$

additional nodes need to be computed, giving a a total of $A = HB$ additional stream and collide operations and thus a cubic growth of A in H. It is concluded that the choice of $H_{\max}$ requires a trade-off between accuracy and computational efficiency.

In the next section, another NRBC is discussed that does not rely on any kind of grid extension.

4.2 Characteristic BC

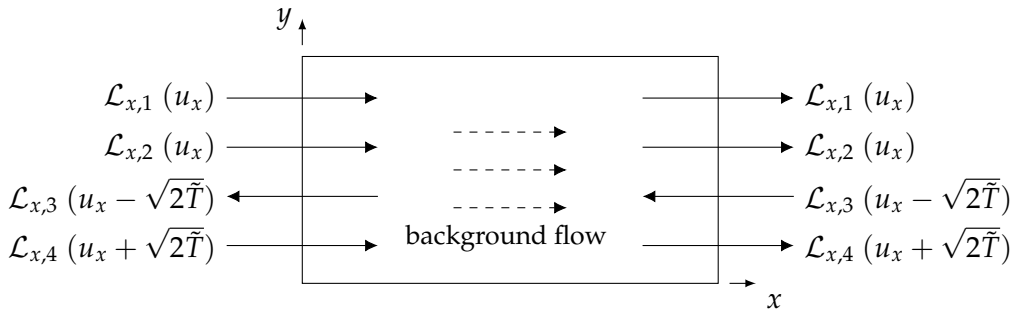

FIGURE 4.4: Two-dimensional rectangular computational domain, with an inlet (outlet) at the left-hand (right-hand) side x-boundary . The orientation of the four characteristic waves amplitude variations $\mathcal{L}_{x,i}$ from the thermal CBC based on Eq. (4.11) is sketched assuming $u_x > 0$ and $\mathrm{Ma} < 1$.

In contrast to the DABC discussed in the previous section, Characteristic Boundary Conditions (CBCs) are derived from continuous equations on the macroscopic level. The general idea of characteristic BCs is to obtain wave amplitude variations of incoming and outgoing waves by means of characteristic analysis of a hyperbolic system. The variation of the outgoing wave amplitude can be then computed from the adjacent fluid nodes, whereas incoming waves need to be specified using (application dependent) external information.

Thompson [70] introduced characteristic boundary conditions for non-linear hyperbolic systems such as the Euler equations (2.1). This approach has been extended to non-hyperbolic Navier-Stokes equations by Poinsot and Lele [71]. To enable a characteristic analysis, the wave amplitude variations where computed using the one-dimensional Euler equations. As transversal and viscous terms are dropped, this is referred to as a Local One-Dimensional Inviscid (LODI) problem. On solving this problem, macroscopic target values are obtained and subsequently posed as a Dirichlet BC. The LODI approach can be improved upon by reincorporation of the transversal and viscous contributions [78–80]. Both the LODI procedure [21, 81] and the reincorporation of transversal and viscous information [82, 83] have been applied to single-speed LBM.

This section recapitulates the details of the characteristic analysis and describes the LODI approach and its improvements in detail. Based on works by the author, the characteristic analysis is extended to the thermal case [26] and the application to multi-speed LBM is discussed [25].

4.2.1 Characteristic Analysis

In the following, a bounded rectangular computational domain in $D = 2$ dimensions is assumed. For the sake of brevity, only the case of a right-hand side boundary is discussed here (see Fig. 4.4). It is straightforward to apply the following discussion to other straight boundaries. Furthermore, a procedure for the corners of the computational domain is given.

Isothermal Case

In the isothermal case, the starting point for the characteristic analysis are the Navier-Stokes equations (2.6), where no energy equation is needed to describe the evolution

of temperature. as the temperature is fixed to a reference value and does not evolve, i.e. $T \equiv c_s^2$, the ideal equation of state (2.2) reduces to $p = \rho c_s^2$.

Therefore (2.6) can be expressed as

$$\frac{\partial \rho}{\partial t} = -\nabla \cdot (\rho \mathbf{u}), \qquad \frac{\partial \mathbf{u}}{\partial t} = -(\mathbf{u} \cdot \nabla)\mathbf{u} - \frac{c_s^2 \nabla \rho}{\rho} + \frac{\nabla \cdot \boldsymbol{\sigma}}{\rho} \tag{4.4}$$

In a first step, a hyberbolic system is obtained by dropping the deviatoric stress (2.5) from Eq. (4.4). This approximation is necessary to conduct the characteristic analysis. Given the vector of unknowns $\mathbb{U} = \left(\rho, u_x, u_y\right)^\top$, Eq. (4.4) can be restated as

$$\frac{\partial \mathbb{U}}{\partial t} + A\frac{\partial \mathbb{U}}{\partial x} + B\frac{\partial \mathbb{U}}{\partial y} = 0, \text{ with } A = \begin{pmatrix} u_x & \rho & 0 \\ \frac{c_s^2}{\rho} & u_x & 0 \\ 0 & 0 & u_x \end{pmatrix}, \quad B = \begin{pmatrix} u_y & 0 & \rho \\ 0 & u_y & 0 \\ \frac{c_s^2}{\rho} & 0 & u_y \end{pmatrix}. \tag{4.5}$$

The matrices A and B are similar to diagonal matrices $\Lambda = \mathrm{diag}(u_x - c_s, u_x, u_x + c_s)$ and $V = \mathrm{diag}(u_y - c_s, u_y, u_y + c_s)$ respectively:

$$\Lambda = SAS^{-1}, \qquad \text{with } S = \begin{pmatrix} c_s^2 & -c_s\rho & 0 \\ 0 & 0 & 1 \\ c_s^2 & c_s\rho & 0 \end{pmatrix}, \quad S^{-1} = \begin{pmatrix} \frac{1}{2c_s^2} & 0 & \frac{1}{2c_s^2} \\ -\frac{1}{2c_s\rho} & 0 & \frac{1}{2c_s\rho} \\ 0 & 1 & 0 \end{pmatrix},$$

$$V = TBT^{-1}, \qquad \text{with } T = \begin{pmatrix} c_s^2 & 0 & -c_s\rho \\ 0 & 1 & 0 \\ c_s^2 & 0 & c_s\rho \end{pmatrix}, \quad T^{-1} = \begin{pmatrix} \frac{1}{2c_s^2} & 0 & \frac{1}{2c_s^2} \\ 0 & 1 & 0 \\ -\frac{1}{2c_s\rho} & 0 & \frac{1}{2c_s\rho} \end{pmatrix}.$$

The spatial derivatives in the direction normal to the boundary can be rewritten as

$$A\frac{\partial \mathbb{U}}{\partial x} = S^{-1}\Lambda S\frac{\partial \mathbb{U}}{\partial x} =: S^{-1}\mathcal{L}_x.$$

In the above, the term $\mathcal{L}_x$ describes the amplitude variations of the characteristic waves, and can be expressed as

$$\mathcal{L}_x = \begin{pmatrix} \mathcal{L}_{x,1} \\ \mathcal{L}_{x,2} \\ \mathcal{L}_{x,3} \end{pmatrix} = \begin{pmatrix} (u_x - c_s)(c_s^2\frac{\partial \rho}{\partial x} - c_s\rho\frac{\partial u_x}{\partial x}) \\ u_x\frac{\partial u_y}{\partial x} \\ (u_x + c_s)(c_s^2\frac{\partial \rho}{\partial x} + c_s\rho\frac{\partial u_x}{\partial x}) \end{pmatrix}. \tag{4.6}$$

This formulation allows distinguishing between incoming and outgoing waves on the basis of the sign of the eigenvalues. The i-th characteristic wave with amplitude variation $\mathcal{L}_{x,i}$ travels in positive (negative) x-direction if $\Lambda_{i,i}$ is positive (negative). Now, amplitude variations $\mathcal{L}_{x,\text{out}}$ of outgoing waves are obtained from the bulk dynamics while incoming amplitudes remain to be specified by the BC, i.e $\mathcal{L}_{x,\text{in}} = L^*_{\text{in}}$. The subsequently used vector of modified wave amplitude variations $\bar{\mathcal{L}}_x$ is given by

$$\bar{\mathcal{L}}_{x,i} = \begin{cases} \mathcal{L}_{x,i}, & \text{outgoing wave} \\ L^*_{x,i}, & \text{incoming wave.} \end{cases}$$

The choice of proper values for $L^*_{x,i}$ will be discussed in Sec. 4.2.2.

Given $\bar{\mathcal{L}}_x$, the Navier-Stokes equations (4.4) can be restated in characteristic form as [82]

$$\frac{\partial}{\partial t}\mathbb{U} = \begin{pmatrix} -\frac{1}{c_s^2}\left[\left(\bar{\mathcal{L}}_{x,3} + \bar{\mathcal{L}}_{x,1}\right) - \left(\mathcal{T}_{x,3} + \mathcal{T}_{x,1}\right) - \left(\mathcal{V}_{x,3} + \mathcal{V}_{x,1}\right)\right] \\ -\frac{1}{\rho c_s^2}\left[\left(\bar{\mathcal{L}}_{x,3} - \bar{\mathcal{L}}_{x,1}\right) - \left(\mathcal{T}_{x,3} - \mathcal{T}_{x,1}\right) - \left(\mathcal{V}_{x,3} - \mathcal{V}_{x,1}\right)\right] \\ -\bar{\mathcal{L}}_{x,2} + \mathcal{T}_{x,2} + \mathcal{V}_{x,2} \end{pmatrix}. \tag{4.7}$$

where the quantities $\mathcal{T}_{x,i}, \mathcal{V}_{x,i}$ include transversal and viscous terms respectively. In detailed form, they read

$$\mathcal{T}_x = \begin{pmatrix} \mathcal{T}_{x,1} \\ \mathcal{T}_{x,2} \\ \mathcal{T}_{x,3} \end{pmatrix} = \begin{pmatrix} -\left(\mathbf{u}_t \cdot \nabla_t p + \gamma p \nabla_t \cdot \mathbf{u}_t - \rho c_s \mathbf{u}_t \cdot \nabla_t u_x\right) \\ -\left(\mathbf{u}_t \cdot \nabla_t u_y + \frac{1}{\rho}\frac{\partial p}{\partial y}\right) \\ -\left(\mathbf{u}_t \cdot \nabla_t p + \gamma p \nabla_t \cdot \mathbf{u}_t + \rho c_s \mathbf{u}_t \cdot \nabla_t u_x\right) \end{pmatrix},$$

$$\mathcal{V}_x = \begin{pmatrix} \mathcal{V}_{x,1} \\ \mathcal{V}_{x,2} \\ \mathcal{V}_{x,3} \end{pmatrix} = \begin{pmatrix} d_p - \rho c_s d_u \\ d_v \\ d_p + \rho c_s d_u \end{pmatrix},$$

where γ is the ratio of specific heats and

$$\begin{pmatrix} d_p \\ d_u \\ d_v \end{pmatrix} = \begin{pmatrix} (\gamma - 1)\,\sigma_{j,k} : \nabla_j u_k \\ \frac{1}{\rho}\nabla_j \cdot \sigma_{j,2} \\ \frac{1}{\rho}\nabla_j \cdot \sigma_{j,1} \end{pmatrix}.$$

Furthermore, $\mathbf{u}_t = [u_y]$ and $\nabla_t = [\partial y]$ denote transversal velocities and derivatives respectively. Note that in the isothermal case, $\gamma = 1$ holds for an ideal equation of state [33].

In the CBC, Eq. (4.7) is used to determine macroscopic target values $\mathbb{U}$ for the boundary nodes. These values are then enforced in the LBM by means of a Dirichlet BC.

By contrast, in the LODI approximation, only the direction normal to the boundary is considered and transversal terms $\mathcal{T}$ and viscous terms $\mathcal{V}$ are discarded from Eq. (4.7). For our example, considering a right boundary target values of $\mathbb{U}$ are obtained from

$$\frac{\partial \mathbb{U}}{\partial t} = -S^{-1}\,\bar{\mathcal{L}}_x = \begin{pmatrix} -\frac{1}{2c_s^2}\left(\bar{\mathcal{L}}_{x,1} + \bar{\mathcal{L}}_{x,3}\right) \\ \frac{1}{2\rho c_s}\left(\bar{\mathcal{L}}_{x,1} - \bar{\mathcal{L}}_{x,3}\right) \\ -\bar{\mathcal{L}}_{x,2} \end{pmatrix}. \tag{4.8}$$

Before discussing the choice of incoming wave amplitudes, the procedures extension to thermal flow configurations is discussed.

Thermal Case

In the thermal case, the energy equation needs to be considered and the temperature is an additional primitive variable to be tracked. Here, the ideal equation of state (2.35) can be written as $P = \rho\tilde{T}$, where the temperature is scaled as $\tilde{T} = Tc_s^2$. With this, the rescaled temperature evolved in the LBM is $T \sim 1$.

Thus, starting from Eqns. (2.4), the time evolution of the macroscopic quantities $\mathbb{U} := \left(\rho, u_x, u_y, T\right)^\top$ can be expressed as the sum of three distinct contributions

$$\frac{\partial \mathbb{U}}{\partial t} = -A\frac{\partial \mathbb{U}}{\partial x} + \mathbb{T} + \mathbb{V}, \tag{4.9}$$

respectively:

i) the term $A\frac{\partial}{\partial x}\mathbb{U}$, which accounts for derivatives normal to the boundary,

ii) $\mathbb{T}$, which includes spatial derivatives in transversal directions,

iii) $\mathbb{V}$, which includes viscous contributions.

In $D = 2$ spatial dimensions, the explicit form of these terms reads

$$A = \begin{pmatrix} u_x & \rho & 0 & 0 \\ \frac{\tilde{T}}{\rho} & u_x & 0 & c_s^2 \\ 0 & 0 & u_x & 0 \\ 0 & \frac{\tilde{T}}{c_s^2} & 0 & u_x \end{pmatrix}, \mathbb{T} = \begin{pmatrix} -\frac{\partial(\rho u_y)}{\partial y} \\ -u_y \frac{\partial u_x}{\partial y} \\ -\frac{1}{\rho}\frac{\partial(\rho\tilde{T})}{\partial y} - u_y \frac{\partial u_y}{\partial y} \\ -\frac{1}{c_s^2}\frac{\partial(\tilde{T}u_y)}{\partial y} \end{pmatrix}, \mathbb{V} = \begin{pmatrix} 0 \\ \nu\Delta u_x \\ \nu\Delta u_y \\ \frac{\nu c_p}{\mathrm{Pr}\, c_s^2}\Delta\tilde{T} + \frac{\nu}{c_s^2}\tilde{u} \end{pmatrix},$$

where $\tilde{u} = \left(\frac{\partial u_x}{\partial x} - \frac{\partial u_y}{\partial y}\right)^2 + \left(\frac{\partial u_x}{\partial y} + \frac{\partial u_y}{\partial x}\right)^2$. A diagonalization of A gives $A = S^{-1}\Lambda S$ with

$$\Lambda = \mathrm{diag}\left(u_x, u_x, u_x - \sqrt{2\tilde{T}}, u_x + \sqrt{2\tilde{T}}\right). \tag{4.10}$$

The matrices S and S^{-1} are given by

$$S = \begin{pmatrix} -\frac{\tilde{T}}{2\rho c_s^2} & 0 & 0 & \frac{1}{2} \\ 0 & 0 & 1 & 0 \\ \frac{\tilde{T}}{4\rho c_s^2} & -\sqrt{\frac{\tilde{T}}{8c_s^4}} & 0 & \frac{1}{4} \\ \frac{\tilde{T}}{4\rho c_s} & \sqrt{\frac{\tilde{T}}{8c_s^4}} & 0 & \frac{1}{4} \end{pmatrix}, \quad S^{-1} = \begin{pmatrix} -\frac{\rho c_s^2}{\tilde{T}} & 0 & \frac{\rho c_s^2}{\tilde{T}} & \frac{\rho c_s^2}{\tilde{T}} \\ 0 & 0 & -\sqrt{\frac{2c_s^4}{\tilde{T}}} & \sqrt{\frac{2c_s^4}{\tilde{T}}} \\ 0 & 1 & 0 & 0 \\ 1 & 0 & 1 & 1 \end{pmatrix}.$$

It is remarked that the last two eigenvalues in the above expression are structurally of the same form as in the isothermal case. Here, the adiabatic index reads $\gamma = \frac{c_p}{c_v} = 2$ and the temperature is $\tilde{T}$ instead of c_s^2.

With this, the vector of wave amplitude variations for waves crossing the right-hand side boundary is defined as

$$\mathcal{L}_x = \left(\mathcal{L}_{x,1},\ \mathcal{L}_{x,2},\ \mathcal{L}_{x,3},\ \mathcal{L}_{x,4}\right)^\top = \Lambda S\frac{\partial\mathbb{U}}{\partial x}.$$

The explicit form of this equation is

$$\begin{pmatrix} \mathcal{L}_{x,1} \\ \mathcal{L}_{x,2} \\ \mathcal{L}_{x,3} \\ \mathcal{L}_{x,4} \end{pmatrix} = \begin{pmatrix} u_x\left(-\frac{\tilde{T}}{2\rho c_s^2}\frac{\partial\rho}{\partial x} + \frac{1}{2c_s^2}\frac{\partial\tilde{T}}{\partial x}\right) \\ u_x\frac{\partial u_y}{\partial x} \\ \left(u_x - \sqrt{2\tilde{T}}\right)\left(\frac{\tilde{T}}{4\rho c_s^2}\frac{\partial\rho}{\partial x} - \sqrt{\frac{\tilde{T}}{8c_s^4}}\frac{\partial u_x}{\partial x} + \frac{1}{4c_s^2}\frac{\partial\tilde{T}}{\partial x}\right) \\ \left(u_x + \sqrt{2\tilde{T}}\right)\left(\frac{\tilde{T}}{4\rho c_s^2}\frac{\partial\rho}{\partial x} + \sqrt{\frac{\tilde{T}}{8c_s^4}}\frac{\partial u_x}{\partial x} + \frac{1}{4c_s^2}\frac{\partial\tilde{T}}{\partial x}\right) \end{pmatrix}. \tag{4.11}$$

Again, the orientation of $\mathcal{L}_{x,i}$ is given by the sign of the corresponding eigenvalue Λ_{ii} and the outward pointing waves are determined by the bulk dynamics and can thus be computed from Eq. (4.11) whereas the inward pointing waves encode information injected into the system from outside of the computational domain and need to be specified. Hence, $\mathcal{L}_x$ is replaced with a vector $\bar{\mathcal{L}}_x$ to modulate inward pointing wave amplitudes (a few possible choices are discussed in Sec. 4.2.2).

Observe that by discarding transversal and viscous terms at the boundary Eq. (4.9) reduces to

$$\frac{\partial \mathbb{U}}{\partial t} = -S^{-1}\ \bar{\mathcal{L}}_x, \tag{4.12}$$

which coincides with the LODI approximation.

The CBC approach [79, 82], instead, aims at including the effect of transversal and viscous contributions at the boundary to the time evolution of $\mathbb{U}$ by solving

$$\frac{\partial \mathbb{U}}{\partial t} = -S^{-1}\ \bar{\mathcal{L}}_x + \mathbb{T} + \mathbb{V}. \tag{4.13}$$

4.2.2 Choices for incoming wave amplitudes

In this section, possible strategies for the treatment of incoming wave amplitudes for a characteristic boundary condition are revised. This is applicable to both the thermal and isothermal cases discussed above.

A) Annihilation A common approach consists choosing incoming wave amplitudes such that their contribution to the time evolution of $\mathbb{U}$ vanishes [69, 70]. In other words, this means no information enters the bulk and the influence of external dynamics on the domain of interest is completely suppressed.

In the LODI approximation (Eq. (4.12)), this translates to setting incoming wave amplitude variations to zero, i.e., substituting $\mathcal{L}_x$ with a vector $\bar{\mathcal{L}}_x$, whose i-th component is defined as

$$\bar{\mathcal{L}}_{x,i} = \begin{cases} \mathcal{L}_{x,i} & \text{for an outgoing wave } i, \\ 0 & \text{for an incoming wave } i. \end{cases} \tag{4.14}$$

By contrast, in the CBC approach, setting incoming wave amplitudes to zero will not guarantee that no information will travel from the boundary to the bulk domain for cases where transversal and viscous contributions are relevant to the dynamic. This can be seen by casting Eq. (4.13) in the following form:

$$\frac{\partial \mathbb{U}}{\partial t} = -S^{-1}\ \bar{\mathcal{L}}_x + \mathbb{T} + \mathbb{V} = -S^{-1}\big(\ \bar{\mathcal{L}}_x - \mathcal{T}_x - \mathcal{V}_x\big),$$

where $\mathcal{T}_x = S\mathbb{T}$, $\mathcal{V}_x = S\mathbb{V}$. As a remedy, the contributions $\mathcal{T}_x$ and $\mathcal{V}_x$ can be absorbed in the unknown wave amplitude variation $\bar{\mathcal{L}}_{x,i}$ as proposed in Ref. [82]:

$$\bar{\mathcal{L}}_{x,i} = \mathcal{T}_{x,i} + \mathcal{V}_{x,i}. \tag{4.15}$$

This strategy of completely annihilating incoming waves theoretically leads to a perfectly non-reflecting BC. In practice, however, due to discretization errors and the fact that wave amplitudes get computed from an approximate system, reflection waves are generally still present.

B) Relaxation towards target quantities As observed in the previous paragraph, posing a perfectly non-reflecting BC gives no control over the macroscopic values at the boundary since their time evolution strongly depends on the outgoing waves. On the other hand, imposing desired target values by means of a Dirichlet BC generally leads to significant reflection waves. As a trade-off between these two cases, a relaxation towards a target macroscopic value can be incorporated in the incoming wave amplitude variations [71, 84]. A general expression for the unknown wave

amplitudes in conjunction with the CBC approach was proposed in Ref. [79] and reads as:

$$\bar{\mathcal{L}}_{x,i} = \mathcal{T}_{x,i} + \mathcal{V}_{x,i} + \alpha(\mathcal{T}^{\infty}_{x,i} - \mathcal{T}_{x,i}) + \beta(Z - Z^{\infty}), \tag{4.16}$$

where a chosen macroscopic quantity Z (e.g. the pressure), and transversal waves $\mathcal{T}^{\infty}_{x,i}$, are relaxed towards target values Z^{∞} and $\mathcal{T}^{\infty}_{x,i}$ at rates α and β, respectively. This strategy has been reported to increase numerical stability and accuracy [79].

Note that the same strategy can be applied to the LODI approach (4.12), i.e.,

$$\bar{\mathcal{L}}_{x,i} = \beta(Z - Z^{\infty}). \tag{4.17}$$

To demonstrate the way this choice influences the macroscopic values at the boundary, consider a right-hand side outlet boundary (i.e. $u_x > 0$) for isothermal flow. Assuming subsonic flow (Ma < 1 or equivalently $u_x < c_s$), the quantities $\mathcal{L}_{x,2}, \mathcal{L}_{x,3}$ can be computed from Eq. (4.6). Determining $\bar{\mathcal{L}}_{x,1}$ from Eq. (4.17) and plugging it into Eq. (4.8) gives

$$\rho c_s \frac{\partial u_x}{\partial t} - c_s^2 \frac{\partial \rho}{\partial t} = \beta(Z - Z^{\infty}).$$

That is, as the fluid approaches a steady state and the time derivatives of the flow fields go to zero, the chosen quantity Z approaches its reference state at rate β. However, the relaxation coefficients pose additional degrees of freedom that have to be determined.

4.2.3 Realization of characteristic BC in the LBM

The previous sections described how to obtain macroscopic target values $\mathbb{U}$ by conducting a characteristic analysis. These target values need to be translated to mesoscopic populations in order to implement a characteristic BC in the LBM.

The general procedure to apply the characteristic BCs to the LBM [21, 81] is summarized in Fig. 4.5. The starting points are the macroscopic flow fields computed by the LBM algorithm (see Sec. 2.3) at a generic time t. The task of the boundary condition is to define the lattice populations left undefined at the boundary of the computational domain. To this aim, a spatial discretization is performed, replacing the spatial derivatives with finite differences and enabling the computation of the discrete analogue of the vector of manipulated wave amplitudes $\bar{\mathcal{L}}_x$ given by Eq. (4.11). Plugging this vector into the corresponding macroscopic evolution equation and performing a time integration, macroscopic target values for the next time step $t + \Delta t$ are obtained. Finally, the computed target values are supplied to the LBM by means of a mesoscopic Dirichlet BC, thus specifying the missing populations at time $t + \Delta t$.

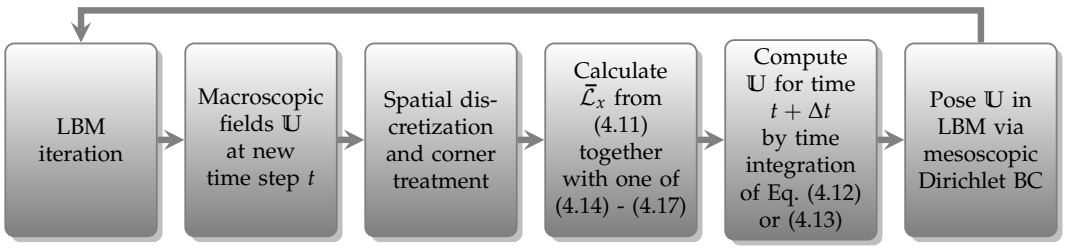

FIGURE 4.5: Flowchart of the conceptual steps required to pose a characteristic BC in the LBM.

In a few studies, the CBC scheme has been applied to LBM [82, 83]. Recently, the applicability of CBCs for multi-speed models has been discussed [26, 85].

The remaining part of this section provides details on the implementation of CBC for multi-speed stencils, corner treatment and possible choices for space and time discretization.

Multi-speed LBM For multi-speed LBM, $\mathcal{M}$ layers of boundary nodes exhibit missing populations, where $\mathcal{M}$ is the maximum displacement of the underlying velocity stencil. For the D2Q17 and D2Q37 velocity stencils (see Sec. 2.4.1) considered in this work , $\mathcal{M} = 3$ holds. Recalling the labelling convention for from Chapter 3, for a fixed y, boundary nodes are labelled as

$$\mathbf{x}_b^{(k)} = (x_b^{(k)}, y),\ k\ = 0, \ldots, \mathcal{M} - 1.$$

In the above, $\mathbf{x}_b^{(0)}$ is adjacent to the outermost fluid node $\mathbf{x}_f = (x_f, y)$ and $\mathbf{x}_b^{(\mathcal{M}-1)}$ is the outermost boundary node (see Fig. 4.6). The characteristic analysis is conducted layer by layer for each layer of boundary nodes. As explained in Sec. 4.2.1, waves crossing the k-th layer of boundary nodes are identified by the sign of the corresponding eigenvalue and the incoming wave amplitude variations are posed on $\mathbf{x}_b^{(k)}$. Note that the resulting target values may differ for the various layers forming the boundary. Finally, the macroscopic equation describing the time evolution of $\mathbb{U}$ on the boundary is solved numerically. Details on the numerical solution are reported in the paragraphs below.

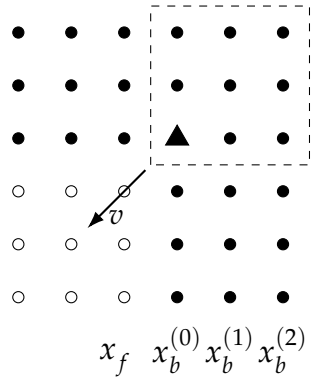

FIGURE 4.6: Schematic boundary geometry for multi-speed velocity stencils with a displacement of $\mathcal{M} = 3$. Filled (hollow) symbols denote boundary (bulk) nodes. To pose a characteristic BC, finite differences are applied to approximate spatial derivatives in the boundary nodes. The triangle node is used to calculate the target macroscopic quantities for all corner nodes in the dashed rectangle. In this case, spatial derivatives are evaluated along the inward diagonal v indicated by the arrow.

Spatial discretization and corner treatment The spatial derivatives of macroscopic quantities $\mathbb{U}$ on a boundary node $\mathbf{x}_b^{(k)}$ at a fixed time t are approximated with second order finite differences. Dropping the fixed time t for the sake of a compact notation, a spatial discretization step in x-direction is denoted by $\mathbf{e}_x = (\Delta x, 0)^\top$. For $\mathbf{x}_b^{(\mathcal{M}-1)}$ (outermost layer), one-sided finite differences are used to replace the spatial derivatives:

$$\frac{\partial \mathbb{U}_i(\mathbf{x}_b^{(\mathcal{M}-1)})}{\partial x} \approx \tfrac{1}{2}\big(3\mathbb{U}_i(\mathbf{x}_b^{(\mathcal{M}-1)}) - 4\mathbb{U}_i(\mathbf{x}_b^{(\mathcal{M}-2)}) + \mathbb{U}_i(\mathbf{x}_b^{(\mathcal{M}-3)})\big). \tag{4.18}$$

For inner boundary nodes $\mathbf{x}_b^{(k)},\ k = 0, \ldots, \mathcal{M} - 2$, central finite differences are used:

$$\frac{\partial \mathbb{U}_i(\mathbf{x}_b^{(k)})}{\partial x} \approx \tfrac{1}{2}\big(\mathbb{U}_i(\mathbf{x}_b^{(k)} + \mathbf{e}_x) - \mathbb{U}_i(\mathbf{x}_b^{(k)} - \mathbf{e}_x)\big). \tag{4.19}$$

Spatial derivatives in y-direction are evaluated analogously.

This procedure is used for any straight boundary (i.e. upper, lower, left,right boundary c.f. Fig. 4.4). Corners can be treated using a combination of the LODI approaches along the $x-$ and $y-$ axis respectively. However, compatibility conditions must be defined if the corner lies at the intersection between different types of BC [80]. In this work, a simpler approach is considered, where spatial derivatives are computed in the direction of the inward facing diagonal (e.g. $v = (-1,-1)^\top$ in the example given in Fig. 4.6, where the top right corner is considered). Target macroscopic quantities for all corner nodes (dashed box in Fig. 4.6) are obtained by conducting the characteristic analysis only in innermost corner node (triangle node in Fig. 4.6).

Evaluation of viscous terms The CBC described in this work (see Tab. 4.1) aims at reconstructing the full Navier-Stokes-Fourier equations on the boundary. This should be contrasted with the recent implementation of characteristic BCs for multi-speed LBM given in [85], where the focus was on acoustic problems and thus the viscous terms where discarded.

To ensure consistency in the coupling of mesoscopic and macroscopic scales at the boundary, the link between the scales provided by the Chapman-Enskog expansion is exploited. This multi-scale expansion offers expressions for the viscous terms on the macroscopic scale in terms of the mesoscopic distribution.

That is, the Laplacian of velocity appearing in Eq. (2.4) is approximated as [33]

$$\mu\partial_{jj}u_k \approx \nabla_j \cdot \left(-\left(1-\tfrac{1}{2\tau}\right)\sum_{i=1}^{d} c_j^{(i)} c_k^{(i)} f_i^{\mathrm{neq}} \right), \tag{4.20}$$

where the derivatives of the non-equilibrium part $f_i^{\mathrm{neq}} = f_i^{\mathrm{eq}} - f_i$ are evaluated in $\mathbf{x}_f$ – i.e. in the fluid node adjacent to the boundary (see Fig. 4.6) – using the finite differences (4.18) and (4.19) (along y). For a sufficiently high order quadrature, which allows recovery of the third order moment of the distribution, the heat-flux can be computed as

$$\mathbf{q} = \frac{1}{2}\sum_{i=1}^{d} f_i |\mathbf{c}^{(i)} - \mathbf{u}|^2 \left(\mathbf{c}^{(i)} - \mathbf{u}\right).$$

It is then possible to evaluate the Laplacian of temperature as

$$-\kappa\partial_{jj}T = \mathrm{div}(\mathbf{q}) = \nabla \cdot \frac{1}{2}\sum_{i=1}^{d} f_i |\mathbf{c}^{(i)} - \mathbf{u}|^2 \left(\mathbf{c}^{(i)} - \mathbf{u}\right). \tag{4.21}$$

That is, only first order spatial derivatives of $\mathbf{q}$ need to be evaluated using finite differences (e.g. (4.18) or (4.19)).

Table 4.1 summarizes the different CBC schemes which will be evaluated in numerical simulations in the upcoming sections.

Name	Macroscopic Eq.	Incoming amplitude
LODI	(4.12)	(4.14)
CBC	(4.13)	(4.15)
CBC-RELAX	(4.13)	(4.16)

TABLE 4.1: Summary of the characteristic based BC considered in this work.

Time integration The implementation of a characteristic BC requires time integration of either Eq. (4.12) or Eq. (4.13). As pointed out in Ref. [85], it is not possible to use an explicit Euler scheme for time integration since the lattice time step leads to the violation of the CFL condition for the FD solver.

Here, the fourth order Runge-Kutta scheme (RK4) [86] is used, which requires spatial derivative at time $t + \frac{\Delta t}{2}$ that are approximated using the second order finite differences (4.18) and (4.19). Macroscopic quantities located on fluid nodes at this intermediate stage are obtained by linear interpolation in time.

For simplicity, the time integration of the CBC scheme is conducted with viscous terms (4.20) and (4.21) kept at time t, since no information about f is available at time $t + \frac{\Delta t}{2}$.

The resulting macroscopic target values $\mathbb{U}$ are then imposed in the LBM using a mesoscopic Dirichlet BC. Further details on this are given in Sec. 4.4.

4.3 Perfectly Matched Layers

The Perfectly Matched Layer (PML) technique is an established tool to treat artificial boundaries. While it has been originally formulated for the absorption of electromagnetic waves governed by the Maxwell equations [73], it has been successfully applied to elastodynamics [87] as well as the Schrödinger [88], Helmholtz [89] and Navier-Stokes equations [76].

In the context of fluid dynamics, Hu developed the perfectly matched layer technique for linearised Euler equations [74] and later extended it for the case of nonlinear Euler and Navier-Stokes equations [76] as well as the Boltzmann equation [90]. Further developments lead to an application of the PML to the LBM [22, 91].

Using the PML technique, the computational domain is padded out with a dampening zone of a given width W. In this zone, the governing equations are modified in a way that i) causes outgoing waves to decay exponentially and ii) is *perfectly* matched to the bulk in the sense that the interface between fluid and PML region will not cause reflections.

The strength of the dampening is controlled by an absorption coefficient σ. This coefficient does not need to be constant, but may vary spatially over the dampening zone. In general, it is not clear how the profile of σ over the dampening layer should be chosen, which leaves some room for optimization [92]. In this work, the common practice [90] of ramping up the absorption coefficient σ quadratically is adopted. That is, the dampening strength is given as

$$\sigma = \sigma_{\max} \left(\frac{w}{W} \right)^2, \tag{4.22}$$

where w denotes the distance from the bulk. It is remarked that the PML itself is not a BC, but enables usage of standard BC, as outgoing waves are decayed before they interact with the boundary.

Dampening waves Following [67], an intuition for the working principle of the PML is given by considering a wave of the form $W = e^{\mathbf{i}(kx-\omega t)}$. When subjected to a complex coordinate transformation, it becomes

$$W = e^{\mathbf{i}(kx-\omega t)} e^{-\frac{k}{w}\int_{x_0}^{x} \sigma_x dx}$$

and the second factor in the expression above causes the wave to exponentially decay if and only if

$$\frac{k}{w}\int_{x_0}^{x}\sigma_x dx > 0. \tag{4.23}$$

This means that waves propagating from a given point x_0 to the right (left) decay given their phase velocity $\frac{\omega}{k}$ is positive (negative). Thus, the PML can be seen as a coordinate stretching in the frequency domain.

In the following section, the main steps to derive the modified PML equations, as given in [22], are discussed. A thorough discussion of the PML approach for both the discrete velocity Boltzmann-BGK equation (2.30) and fully discrete lattice Boltzmann-BGK equation (2.31) can be found in [93].

Derivation of PML for LBM The starting point for the derivation of the governing equations in the PML zone is the discrete velocity Boltzmann-BGK equation (2.30) that can be rewritten as

$$\frac{\partial f_i}{\partial t} + A\frac{\partial f_i}{\partial x} + B\frac{\partial f_i}{\partial y} = -\frac{1}{\tau}\left(f_i - f_i^{\mathrm{eq}}\right), \tag{4.24}$$

where $A = \mathrm{diag}\left(c_x^{(1)},\ldots,c_x^{(d)}\right)$ and $B = \mathrm{diag}\left(c_y^{(1)},\ldots,c_y^{(d)}\right)$. The distribution f_i is decomposed in equilibrium parts f_i^{eq} and non-equilibrium parts f_i^{neq}

$$f_i = f_i^{\mathrm{eq}} + f_i^{\mathrm{neq}} = \bar{f}_i^{\mathrm{eq}} + \tilde{f}_i^{\mathrm{eq}} + f_i^{\mathrm{neq}}, \tag{4.25}$$

and f_i^{eq} is again split into a mean equilibrium component $\bar{f}_i^{\mathrm{eq}}$ and a deviation $\tilde{f}_i^{\mathrm{eq}}$ from this equilibrium.

Plugging f_i^{eq} into Eq. (4.24) yields

$$\frac{\partial f_i^{\mathrm{eq}}}{\partial t} + A\frac{\partial f_i^{\mathrm{eq}}}{\partial x} + B\frac{\partial f_i^{\mathrm{eq}}}{\partial y} = 0.$$

Therefore, due to the decompositions above, the equations

$$\frac{\partial \bar{f}_i^{\mathrm{eq}}}{\partial t} + A\frac{\partial \bar{f}_i^{\mathrm{eq}}}{\partial x} + B\frac{\partial \bar{f}_i^{\mathrm{eq}}}{\partial y} = 0, \tag{4.26}$$

$$\frac{\partial \tilde{f}_i^{\mathrm{eq}}}{\partial t} + A\frac{\partial \tilde{f}_i^{\mathrm{eq}}}{\partial x} + B\frac{\partial \tilde{f}_i^{\mathrm{eq}}}{\partial y} = 0, \tag{4.27}$$

$$\frac{\partial f_i^{\mathrm{neq}}}{\partial t} + A\frac{\partial f_i^{\mathrm{neq}}}{\partial x} + B\frac{\partial f_i^{\mathrm{neq}}}{\partial y} = -\frac{f_i^{\mathrm{neq}}}{\tau} \tag{4.28}$$

are obtained. Splitting up $\tilde{f}_i^{\mathrm{eq}} = \tilde{M}_i^{+}\tilde{N}_i$ and introducing damping coefficients σ_α to the left hand side of (4.27) gives the expression

$$\frac{\partial \tilde{M}_i}{\partial t} + \sigma_x \tilde{M}_i^{\mathrm{eq}} + A\frac{\partial \tilde{f}_i^{\mathrm{eq}}}{\partial x} = 0, \quad \frac{\partial \tilde{N}_i}{\partial t} + \sigma_y \tilde{N}_i^{\mathrm{eq}} + B\frac{\partial \tilde{f}_i^{\mathrm{eq}}}{\partial y} = 0. \tag{4.29}$$

This formulation can be shown to result in exponential decay of outgoing waves in the PML zone, thus minimizing reflections [87]. However, it is possible to achieve a slightly more elegant form of the PML equations [22, 74]. Casting Eq. (4.29) to the

frequency domain using

$$\tilde{f}_i(x,y) = \hat{f}_i(x,y,t)\exp(-\mathbf{i}\omega t),$$

one obtains the two equations

$$-\mathbf{i}\omega\hat{M}_i + \sigma_x\hat{M}_i + A\frac{\partial\hat{f}_i}{\partial x} = 0, \quad -\mathbf{i}\omega\hat{N}_i + \sigma_y\hat{N}_i + B\frac{\partial\hat{f}_i}{\partial y} = 0.$$

Dividing the above equations by $\frac{1+\mathbf{i}\sigma_x}{\omega}$ and $\frac{1+\mathbf{i}\sigma_y}{\omega}$ gives

$$-\mathbf{i}\omega\hat{M}_i + \frac{1}{1+\frac{\mathbf{i}\sigma_x}{\omega}}A\frac{\partial\hat{f}_i}{\partial x} = 0, \quad -\mathbf{i}\omega\hat{N}_i + \frac{1}{1+\frac{\mathbf{i}\sigma_y}{\omega}}B\frac{\partial\hat{f}_i}{\partial y} = 0.$$

Summing up these two equations and some rearrangement gives

$$-\mathbf{i}\omega\hat{f}_i + A\frac{\partial\hat{f}_i}{\partial x} + B\frac{\partial\hat{f}_i}{\partial x} = -(\sigma_x+\sigma_y)\hat{f}_i - (\sigma_x\sigma_y)\hat{Q}_i - A\frac{\partial}{\partial x}\sigma_y\hat{Q}_i - B\frac{\partial}{\partial y}\sigma_x\hat{Q}_i$$

with the auxiliary variable $\hat{Q}_i = \frac{\mathbf{i}}{\omega}\hat{f}_i$. Transforming this back to the time domain gives

$$\frac{\partial\tilde{f}_i^{\mathrm{eq}}}{\partial t} + A\frac{\partial\tilde{f}_i^{\mathrm{eq}}}{\partial x} + B\frac{\partial\tilde{f}_i^{\mathrm{eq}}}{\partial y} = \underbrace{-\left[\sigma_y A\frac{\partial Q_i}{\partial x} + \sigma_x B\frac{\partial Q_i}{\partial y} + (\sigma_x+\sigma_y)\tilde{f}_i^{\mathrm{eq}} + \sigma_x\sigma_y Q_i\right]}_{:=\Omega_{PML}},$$

where Q_i is defined by the equation $\frac{\partial Q_i}{\partial t} = \tilde{f}^{\mathrm{eq}}$. Its value at the next time step $t+\Delta t$ can be numerically calculated using the trapezoidal rule as

$$Q_{t+\Delta t} = \tfrac{1}{2}(\tilde{f}_{\Delta t}^{\mathrm{eq}} + f_{t+\Delta t}^{\mathrm{eq}} - \bar{f}_{t+\Delta t}^{\mathrm{eq}}).$$

To ensure stability, the authors in [22] suggest to set $\sigma_x = \sigma_y = \sigma$. With this, the quantity Ω_{PML} can be simplified to

$$\Omega_{PML} = -\sigma\left(\mathbf{c}^{(i)}\cdot\nabla Q_i + 2\tilde{f}_i^{\mathrm{eq}} + \sigma Q_i\right).$$

Due to the decomposition (4.25), the evolution of f is obtained as

$$\frac{\partial f_i}{\partial t} + A\frac{\partial f_i}{\partial x} + B\frac{\partial f_i}{\partial y} = -\frac{1}{\tau}\left(f_i - f_i^{\mathrm{eq}}\right) + \Omega_{PML}. \tag{4.30}$$

The equation above is just the Boltzmann-BGK equation (4.24) with the additional term Ω_{PML} in the collision operator. This gives a straightforward way of implementing the PML for the LBM by just modifying the collision step, where the additional term Ω_{PML} needs to be evaluated.

NRBCs and PML The PML itself is not a BC but an absorbing layer padded around the computational domain. It offers a simple implementation by modifying the collision step in the additional layers according to the right hand side of Eq. (4.30). Furthermore, it makes the choice of the actual BC beyond the PML zone less crucial to achieve non-reflecting behaviour, as the reflections are dampened out by the absorbing layers.

However, the introduction of additional layers causes a computational overhead. It is therefore of interest to choose the smallest possible value for W that yields a required level of accuracy. This motivates the usage of NRBCs beyond the PML to potentially decrease the total runtime required for a simulation with such accuracy. To the best of the authors knowledge, no such study has yet been conducted in the literature.

4.4 Numerical Results

This section contains a numerical evaluation of the NRBCs discussed in this chapter.

First, two flow configurations with strictly one-dimensional dynamics are considered. In Sec. 4.4.1 an isothermal density step is simulated. This allows to isolate the effect of switching from single-speed to multi-speed velocity stencils by comparing results obtained from the D2Q9 and D2Q17 stencils. The NRBCs suitability for thermal flow is inspected in Sec. 4.4.2, where a thermal flow arising from an initial temperature step is discussed. In Sec. 4.4.3, a more challenging thermal flow with two-dimensional dynamics is considered, namely the interaction of a propagating vortex with an artificial boundary. Sec. 4.4.4 contains results on the errors caused by an oblique waves that approaches the boundary. Finally, Sec. 4.4.5 considers the impact of NRBCs on drag and lift coefficients at a square obstacle.

Reference simulation In order to quantify the accuracy of each NRBC, i) global relative L^2-errors e_Z and ii) pointwise relative errors $\widetilde{e}_Z$ with respect to a reference field Z^{ref}, where $Z \in \{\rho, u_x, u_y, T\}$ are computed. They are defined as

$$e_Z = \sqrt{\sum_{\substack{(x,y)\in \\ L_x\times L_y}} \left(\frac{|Z(x,y) - Z^{\mathrm{ref}}(x,y)|}{|Z^{\mathrm{ref}}(x,y)|}\right)^2}, \quad \widetilde{e}_Z(x,y) = \frac{|Z(x,y) - Z^{\mathrm{ref}}(x,y)|}{|Z^{\mathrm{ref}}(x,y)|}. \tag{4.31}$$

The reference fields Z^{ref} are obtained from a fully periodic LBM simulation on an extended computational domain. The domain is chosen to be sufficiently large to ensure that due to the finite speed of propagation, no error introduced by the periodicity can affect the bulk dynamics in the original domain of interest after N_{iter} iterations. Thus, any deviation from the reference fields can be attributed to the NRBC used.

For comparison, simulations with a Zero Gradient (ZG) BC are conducted. Using this scheme, all populations on boundary nodes are obtained by constant extrapolation from the adjacent fluid node. That is, for $k = 0, \ \ldots, \ \mathcal{M} - 1$, the ZG BC sets

$$f_i(\mathbf{x}_b^{(k)}, t) = f_i(\mathbf{x}_f, t), \quad i = 1, \ \ldots, \ d. \tag{4.32}$$

For a given BC, the total simulation time is measured and a number $\hat{t}$ is computed, that gives the relative increase in simulation time over the ZG BC. For a given macroscopic quantity Z, the relative reduction in maximum global error with respect to the ZG BC is computed as

$$\hat{e}_Z = \frac{\max e_Z}{\max e_Z^{ZG}}. \tag{4.33}$$

4.4.1 Isothermal Flow: Density Step

First, a strictly mono-dimensional flow in a shock-tube-like setting is considered. That is, the initially homogeneous macroscopic fields are perturbed along the x-axis by the action of the hyberbolic tangent. The resulting flow remains stratified along the y-direction. The grid size is $L_x \times L_y = 200 \times 20$ and periodic boundary conditions are used at the upper and lower boundaries while left and right boundaries are equipped with artificial BC. Thus, the reference simulation takes place on a $(L_x + 2\mathcal{M}N_{\text{iter}}) \times L_y$ grid. Here, the accuracy of the NRBCs for isothermal flow is inspected for the single-speed D2Q9 and the multi-speed D2Q17 velocity stencils. The initial conditions for density and velocity read

$$\rho(x,y) = \begin{cases} \rho_1 + \frac{\rho_1-\rho_0}{2}(\tanh\left(\mathrm{s}\left(x - \frac{L_x}{4}\right)\right) - 1), \text{ if } x \leq \frac{L_x}{2} \\ \rho_1 - \frac{\rho_1-\rho_0}{2}(\tanh\left(\mathrm{s}\left(x - \frac{3L_x}{4}\right)\right) - 1), \text{ else} \end{cases}, \mathbf{u}(x,y) = (\mathrm{Ma}\cdot c_s, 0), \quad (4.34)$$

with $\rho_1 = 1.05$, $\rho_0 = 1$ and steepness parameter $\mathrm{s} = 0.5$. The Mach number is $\mathrm{Ma} = 0.05$ and the Reynolds number $\mathrm{Re} = 10$. The characteristic length L used to calculated the Reynolds number is the amount of lattice nodes affected by the perturbation.

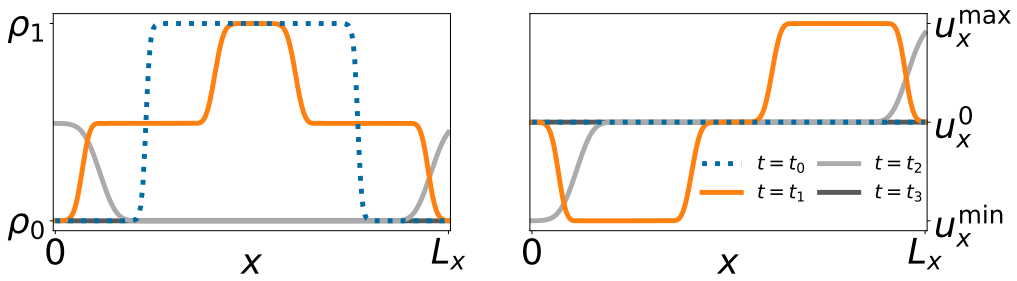

FIGURE 4.7: Density and stream-wise velocity profiles along the horizontal midplane obtained from the reference simulation. The dashed line indicates the initial state at $t = t_0$. The times t_1 and t_2 show the profiles shortly before and during the pulses interaction with the boundary respectively. At time t_3, the system is almost completely at rest.

In Fig. 4.7, density and velocity profiles of the reference simulation along the horizontal midplane $y = \frac{L_y}{2}$ are shown for selected time steps to illustrate the dynamics of the flow.

Before directly comparing the various NRBCs, all schemes are considered individually to better highlight the importance of their respective tunable parameters.

DABC The tunable parameters for the DABC are the maximum history depth $H_{\max}$ and the initialization strategy of the sub-problems. The impact of altering these parameters on the evolution of e_Z is shown in Fig. 4.8.

The results obtained using the three initialization strategies (4.1), (4.2), (4.3) are shown in the first, second and third column respectively. It can be seen that for a fixed initialization strategy, increasing the value of $H_{\max}$ minimizes the maximal errors in density and stream-wise velocity.

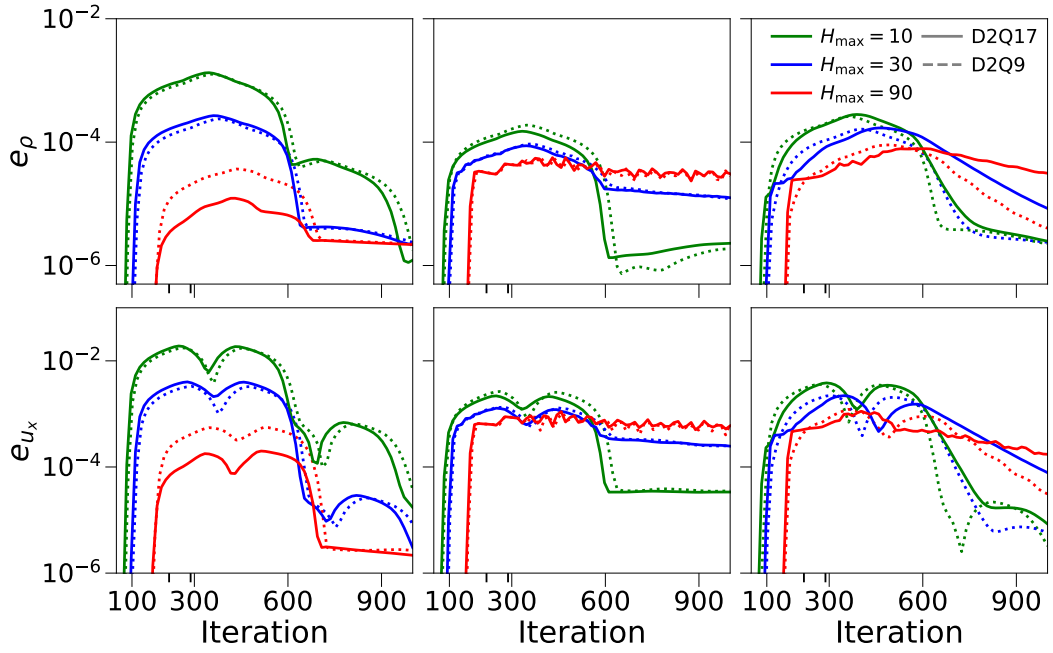

FIGURE 4.8: Error evolution in the density step benchmark using the DABC. The D2Q9 and D2Q17 velocity stencil are compared. From left to right, the columns correspond to initializations according to DABC-A (4.1), DABC-B (4.2) and DABC-C (4.3). Minor ticks on the x-axis correspond to the times t_2, t_3 given in Fig. 4.7.

Comparing the different initialization strategies using a fixed history depth, it is seen that the constant extrapolation approach given by Eq. (4.2), gives lower maximum errors than the fixed initialization for the tested values $H_{\max} \in \{10, 30\}$. However, for $H_{\max} = 90$, the peak errors grow and the accuracy is degraded when iterations > 700 are inspected. This is because as the density pulse interacts with the boundary, the sub-problems initialization using constant extrapolation leads to the injection of additional momentum and pressure into the bulk. This significantly alters the fluids behaviour after the pulse has passed the boundary. This behaviour has also been observed in [94]. By contrast, using the initialization Eq. (4.1), the global errors decline after about 600 iterations, when the small reflections caused by the BC have exited the domain of interest.

The third initialization strategy given by Eq. (4.3) can be viewed as a middle ground between the previous approaches, where the peaks of the error curves should be minimized while also enabling the fluid to return to a rest state once the pulse has left the domain. It can be seen that the errors start to slowly decrease after about 600 iterations. It is also observed that the decrease is more rapid for the single-speed D2Q9 stencil and is also delayed by an increased value of $H_{\max}$. This is expected because the maximum displacement $\mathcal{M}$ and the $H_{\max}$ directly control the amount of layers in the sub-problem that contribute towards injecting additional momentum in the bulk.

Increasing $H_{\max}$ leads to an improvement in capturing the flows interaction with the open boundary if the sub-problems are initialized according to Eq. (4.1). However, increasing the history depth also significantly increases the computational demand, as both the necessary amount of iterations and the grid size in the sub-problems increase. An initialization according to Eq. (4.3) can increase the accuracy for a given history depth, but may lead to a polluted steady state when the value of $H_{\max}$ is too large.

CBC The characteristic based BCs rely on choosing proper values for the incoming wave amplitude variations. Here, the perfectly non-reflecting LODI and CBC schemes (see Tab. 4.1) are considered. The corresponding error evolutions are shown in Fig. 4.9. Since the flow only has strictly 1D dynamics, the transversal terms that a CBC would account for vanish and the only difference in the BCs lies in the viscous terms in the momentum equation. Here, the mesoscopic EBC (3.5) was used to pose the macroscopic target values in the LBM. It can be seen that in general, both schemes yield similar accuracy. However, the CBC leads to slightly larger errors for the D2Q9 stencil. Additionally, the inclusion of diffusive terms leads to slight deformation of the curve describing the time evolution of the errors.

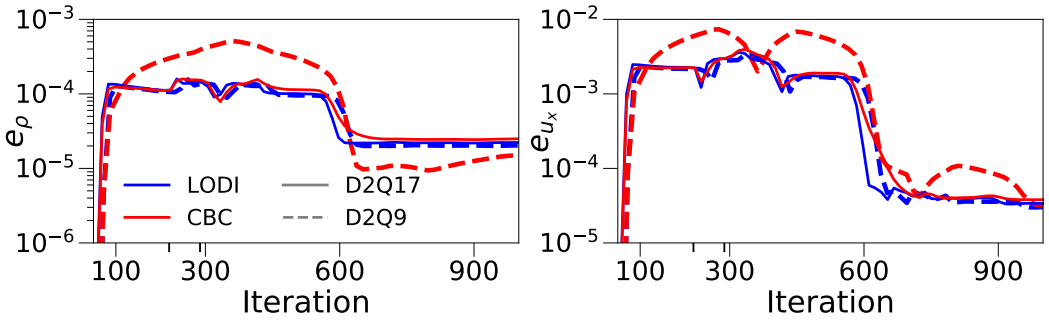

FIGURE 4.9: Error evolution in the density step benchmark using the (perfectly non-reflecting) LODI and CBC BCs. The D2Q9 and D2Q17 velocity stencil are compared. Minor ticks on the x-axis correspond to the times t_2, t_3 given in Fig. 4.7.

PML Here, the left and right-hand side boundaries are padded with absorbing layers, beyond which the LODI BC is used. Now, the PML has two tunable parameters, namely the width of the dampening layer W and the maximum dampening coefficient $\sigma_{\max}$.

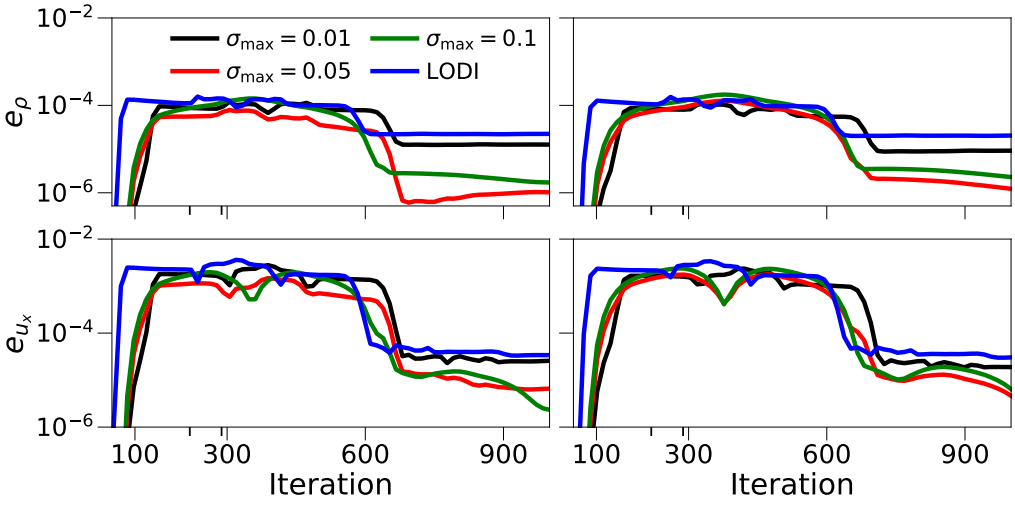

FIGURE 4.10: Error evolution in the density step benchmark using the LODI BC in conjunction with the PML approach. The D2Q9 (right) and D2Q17 (left) stencils are compared. The dampening zone width is fixed to $W = 20$ nodes and $\sigma_{\max}$ is altered. Minor ticks on the x-axis correspond to the times t_2, t_3 given in Fig. 4.7.

Fig. 4.10 shows the time evolution of e_ρ and e_{u_x} for a fixed width of the dampening zone $W = 20$ and various values of $\sigma_{\max}$. Regardless of the velocity stencil

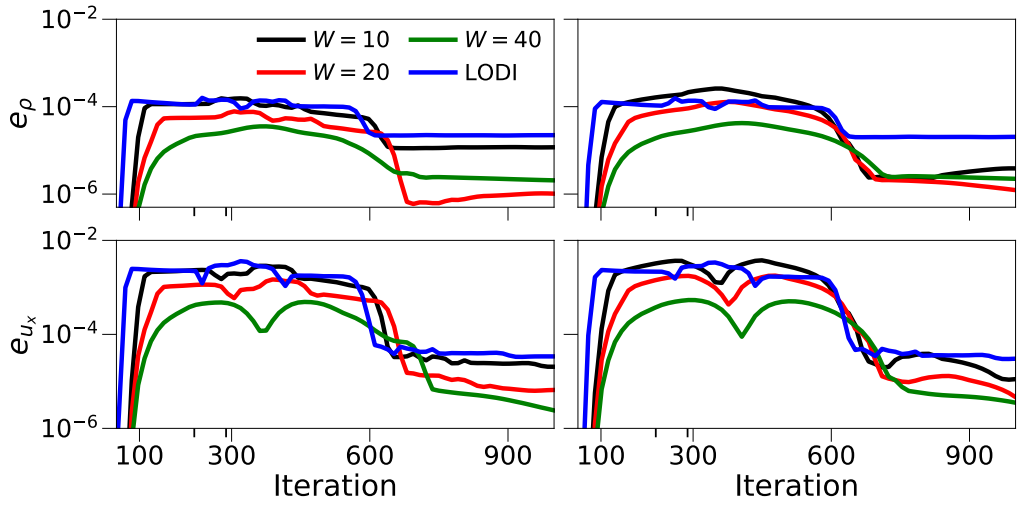

FIGURE 4.11: Error evolution in the density step benchmark using the (perfectly non-reflecting) LODI BC in conjunction with the PML approach. The D2Q9 (right) and D2Q17 (left) velocity stencils are compared. The width of the dampening zone is varied and the value of $\sigma_{\max} = 0.05$ is fixed. The minor ticks on the x-axis correspond to the times t_2, t_3 given in Fig. 4.7.

used, the overall best accuracy is obtained for the choice $\sigma_{\max} = 0.05$. Departure from this value in either direction leads to a loss of accuracy. It is noted that the results obtained using the single-speed D2Q9 and multi-speed D2Q17 stencils match qualitatively.

Varying the value of W and fixing $\sigma_{\max} = 0.05$, it is seen from Fig. 4.11 that using $W = 10$ nodes only brings a small improvement over the results obtained using LODI without any PML. For the D2Q9 stencil, the maximum of e_ρ even grows in this case. Increasing the value to $W = 80$ results in higher accuracy. However, this already requires 80 percent more grid points, as the total grid size is $(L_x + 2W) \times L_y$.

Comparison Here, both the accuracy and computational efficiency of the various NRBCs are directly compared for the D2Q17 stencil.

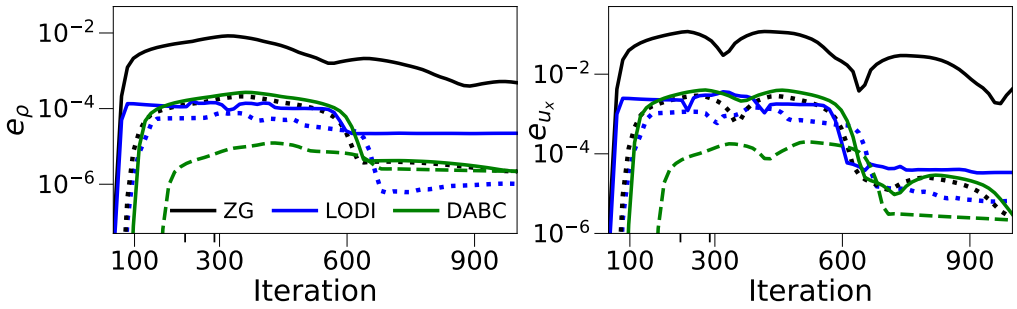

FIGURE 4.12: Direct comparison of the evolution of global errors for various BC. The PML is used with $W = 20$ nodes. For the LODI (ZG) BC, $\sigma_{\max} = 0.05$ ($\sigma_{\max} = 0.2$) is used (dotted lines). The DABC is used with $H_{\max} = 30$ (solid line) and $H_{\max} = 90$ (dashed line) using the initialization (4.1). Minor ticks on the x-axis correspond to the times t_2, t_3 given in Fig. 4.7.

Results from the previous paragraphs are collected in Fig. 4.12, where the time evolution of e_ρ and e_{u_x} is shown for the DABC, LODI BC and the LODI BC in conjunction with PML. Furthermore, results for the ZG BC with and without PML are presented. It is seen that the naive ZG approach gives errors larger by more than one order of magnitude in almost every time step when compared to the NRBCs. However, on introducing a PML of width $W = 20$ nodes at each boundary, error levels similar to the DABC with $H_{\max} = 30$ and the LODI BC are achieved. On combining the LODI BC with PML, the accuracy is further increased. The best overall result is obtained using DABC with $H_{\max} = 90$.

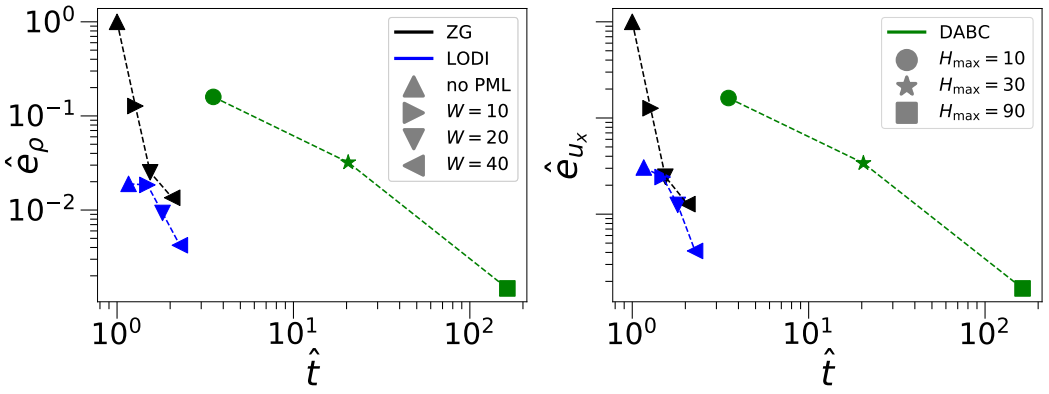

FIGURE 4.13: Accuracy vs performance evaluation of the various BC for a computational domain $L_x \times L_y = 200 \times 20$. Plotted is the relative runtime $\hat{t}$ with respect to the ZG BC versus the maximum value of e_ρ (left) and e_{u_x} (right) respectively, normalized with respect to the ZG BC. The PML is used with $\sigma_{\max} = 0.05$ for LODI and $\sigma_{\max} = 0.2$ for ZG. The DABC is used with the initialization (4.1).

To analyse the computational efficiency of the NRBCs, the quantity $\hat{e}_Z$ given in Eq. (4.33) is plotted against the relative increase in runtime $\hat{t}$ with respect to the ZG BC in Fig. 4.13.

It is seen that usage of PML greatly improves the accuracy of the ZG BC: Introducing an absorbing zone of width $W = 10$ per lateral boundary increases the runtime by about 25 percent while reducing $\hat{e}_\rho$ by approximately one order of magnitude. Using the PML, the size of the computational grid becomes $(L_x + 2W) \times L_y$. In this case, the amount of nodes grows by 10 percent, which explains most of the increased runtime. The additional overhead stems from the computation of the modified collision operator on the right-hand side of (4.30). Thus, roughly 40 percent of the additional computational load come from the grid extension while about 60 percent are due to the modified collision operator. This also holds on increasing the width of the dampening zone to $W = 40$ layers. Doing so increases the amount of nodes by 40 percent and about doubles the simulation time while reducing the $\hat{e}_\rho$ by almost two orders of magnitude.

The LODI BC without any PML requires about 20 percent more runtime than the ZG BC but reduces the maximum errors obtained by almost two orders of magnitude. It is superior to the ZG BC with $W = 20$ additional layers both in terms of runtime and accuracy.

Among the NRBCs considered, the required runtime to achieve a given level of accuracy is minimized when the LODI BC is used, potentially in conjunction with PML. The ZG BC requires thicker dampening layers for a given accuracy, which gives rise to more computational load than the simpler BC is saving over the LODI BC.

The DABC, where one sub-problem has to be solved at the left- and right-hand side boundary, has a significantly larger runtime than the other NRBCs. As discussed in Sec. 4.1, $2\mathcal{M}H_{\max}$ additional layers of nodes are introduced and iterated upon $H_{\max}$ times. With $\mathcal{M} = 3$, this gives $600 \times L_y$ additional stream and collide operations per iteration at $H_{\max} = 10$. That is, the runtime is expected to increase by about a factor of four on the given grid, which is consistent to the data shown in the figure. Accordingly, the DABC with $H_{\max} = 30$ increases the runtime by a factor of about twelve, which results in a performance comparable to the LODI BC (see again Fig. 4.12). Using $H_{\max} = 90$, the maximum error with respect to the LODI BC is about halved. However, the runtime grows by a factor of 50 with respect to the LODI scheme.

4.4.2 Thermal Flow: Temperature Step

Here, a thermal flow arising from the initial conditions

$$\begin{aligned} &\rho(x,y) = \rho_0, \quad \mathbf{u}(x,y) = (\mathrm{Ma} \cdot c_s, 0), \\ &T(x,y) = \begin{cases} T_1 + \frac{T_1 - T_0}{2}(\tanh\left(\mathrm{s}\left(x - \frac{L_x}{4}\right)\right) - 1), & \text{if } x \leq \frac{L_x}{2} \\ T_1 - \frac{T_1 - T_0}{2}(\tanh\left(\mathrm{s}\left(x - \frac{3L_x}{4}\right)\right) - 1), & \text{else} \end{cases} \end{aligned} \tag{4.35}$$

is considered to gauge the accuracy of the newly developed NRBCs for thermal flow configurations. The value of $T_1 = T_0 + \Delta T$ is determined by the Eckert number that has been set to $\mathrm{Ec} = 0.01$. The other simulation parameters remain the same as in the isothermal density step described in the previous section. The dynamics of the flow are sketched in Fig. 4.14, where temperature and velocity profiles obtained from the reference simulation along the horizontal midplane $y = \frac{L_y}{2}$ are shown for selected time steps.

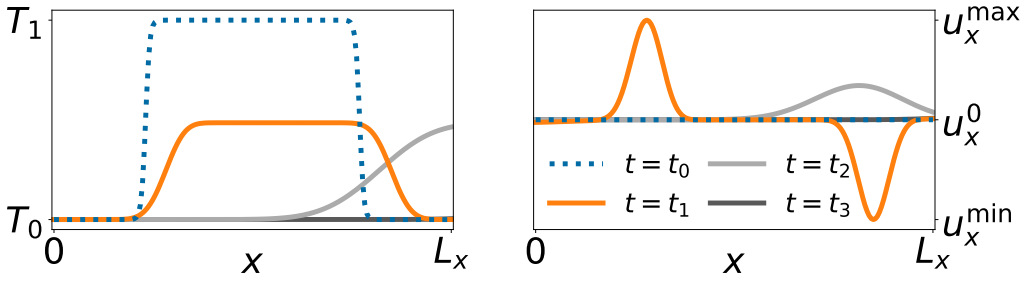

FIGURE 4.14: Temperature and stream-wise velocity profiles obtained from the reference simulation. The dashed line indicates the initial state at $t = t_0$. The times t_1 and t_2 show the profiles shortly before and during the pulses interaction with the boundary respectively. At time t_3, the system is almost completely at rest.

DABC The time evolution of the relative L^2-errors e_Z is shown for various values of $H_{\max}$ in Fig. 4.15. Due to the initialization in (4.35), pressure pulses start to propagate from $x = \frac{L_x}{4}$ and $x = \frac{3L_x}{4}$. They start interacting with the lateral boundaries after a few iterations, which results in the initial spikes in the error evolution. Increasing the history depth $H_{\max}$ significantly reduces the magnitude of these initial spikes. Using $H_{\max} = 30$ only small gains in accuracy are observed during the pulses interaction with the boundary over $H_{\max} = 10$ while $H_{\max} = 90$ gives a more significant improvement.

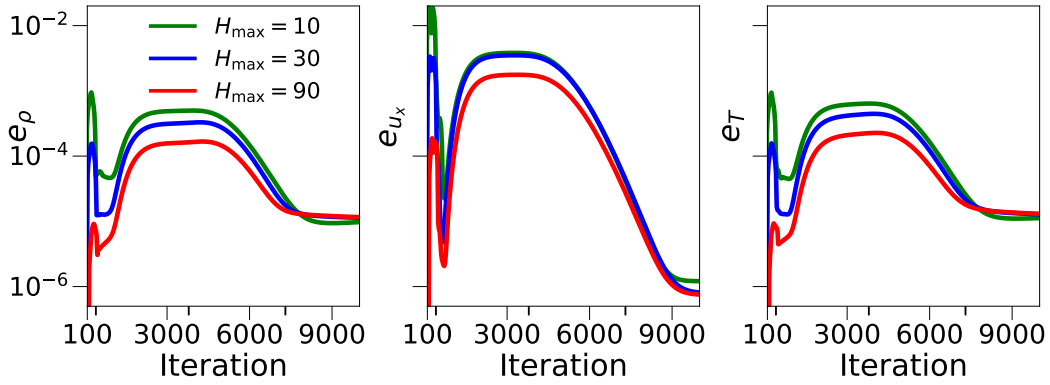

FIGURE 4.15: Error evolution in the temperature step benchmark using the D2Q17 stencil for the DABC at various history depths and initialization strategy (4.1). Minor ticks correspond to the iterations t_1, t_2 and t_3 plotted in Fig. 4.14.

Characteristic BC The impact of the mesoscopic Dirichlet BC used to transfer the macroscopic target values obtained by characteristic analysis to the LBM is inspected by comparing the error evolutions obtained using the EBC (3.5), NEEP BC (3.6) and NEBB schemes (3.10) in conjunction with the LODI BC. This is done in Fig. 4.16 for the D2Q17 and D2Q37 velocity stencils.

Similar to the DABC, the LODI scheme leads to initial spikes in the error evolution due to propagating pressure pulses, regardless of mesoscopic BC and velocity stencil used. For the D2Q17 stencil (Fig. 4.16-left), the EBC and NEBB-SE BC give comparable accuracy. Both are outperformed by the NEEP BC, which minimizes the maximum errors obtained in density in temperature by about one order of magnitude.

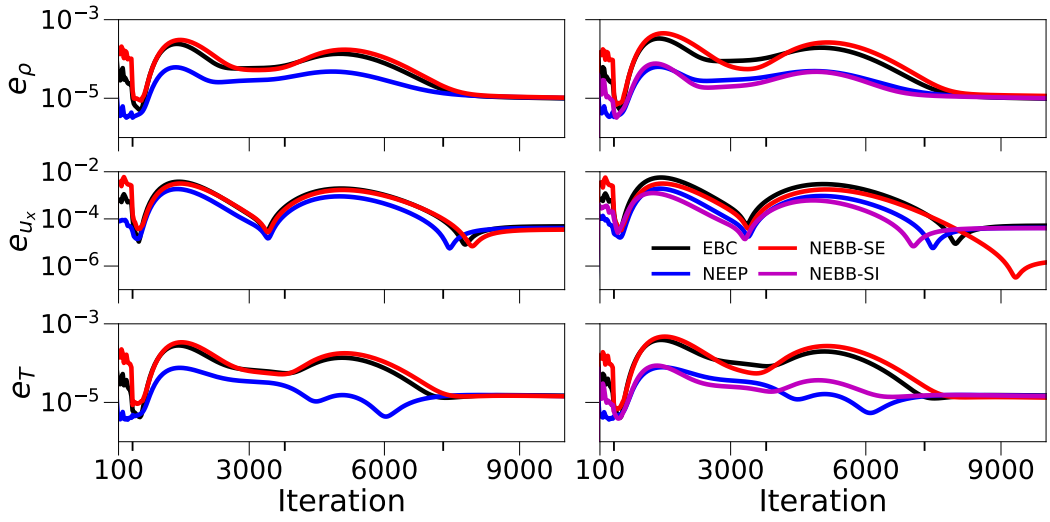

FIGURE 4.16: Error evolution in the temperature step benchmark using the LODI scheme with various mesoscopic Dirichlet BC for the D2Q17 (left) and D2Q37 (right) velocity stencils.The minor ticks on the x-axis correspond to the times t_1, t_2, t_3 given in Fig. 4.14.

The external NEBB-SE is not compatible with the layerwise characteristic analysis: In the external NEBB-SE scheme, all the layers of boundary nodes are subjected to identical macroscopic values (see Sec. 3.1.5). Thus, the macroscopic target values obtained from the layer-wise characteristic analysis are discarded for all but one

layer of boundary nodes. As a remedy, the internal NEBB-SI scheme can be used to impose different target values for each layer of nodes. However, this scheme is not applicable to the D2Q17 stencil used here, as the innermost layer of nodes only has one unknown population to set and thus does not offer enough degrees of freedom to pose all desired macroscopic quantities.

Switching to the D2Q37 stencil (Fig. 4.16-right), the NEBB-SI scheme can also be evaluated. The EBC, NEBB-SE BC give comparable accuracy for this stencil as well and like for the D2Q17 stencil, the NEEP BC, minimizes the maximum errors obtained in density in temperature by about one order of magnitude. It is now seen that the NEBB-SI scheme gives comparable accuracy to the NEEP scheme.

However, the NEEP BC requires significantly less runtime as can be seen from Tab. 4.2, where the relative increase in runtime with respect to the EBC is tabulated. Switching from the EBC to NEEP takes about 23 percent more runtime, while the NEBB-SI scheme increases the runtime by almost a factor seven.

BC	NEEP	NEBB-SE	NEBB-SI
Runtime	1.23	7.70	6.87
$\max e_\rho$	0.19	1.36	0.23
$\max e_{u_x}$	0.34	1.00	0.22
$\max e_T$	0.20	1.21	0.22

TABLE 4.2: Factors describing the change in relative runtime and maximum value $\max e_Z$ attained for various mesoscopic BC used in conjunction with the LODI scheme and the D2Q37 stencil. Baseline was the EBC.

The LODI and CBC approach are compared using both the EBC and NEEP in Fig. 4.17. Due to the subsonic background velocity, the only unknown wave amplitude at the right boundary is $\bar{\mathcal{L}}_{x,3}$. At the left boundary, $\bar{\mathcal{L}}_{x,1}$, $\bar{\mathcal{L}}_{x,2}$ and $\bar{\mathcal{L}}_{x,4}$ need to be posed.

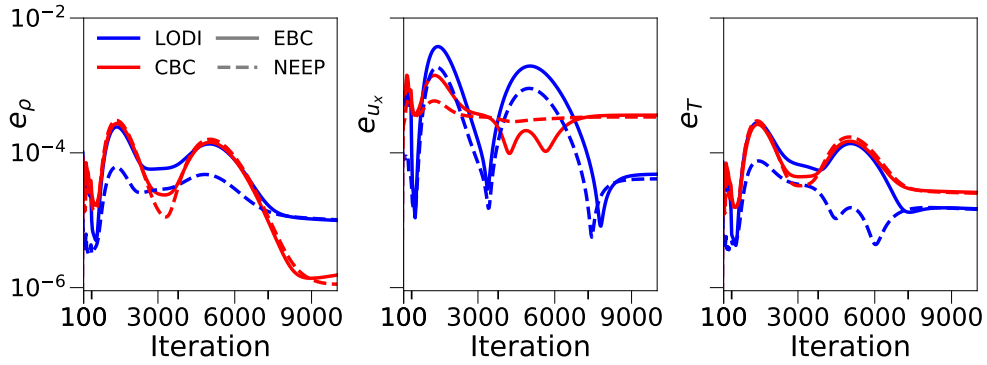

FIGURE 4.17: Error evolution in the temperature step benchmark for the D2Q17 stencil. Macroscopic target values obtained from characteristic analysis enforced by the EBC (solid lines) and NEEP BC (dashed lines).The minor ticks on the x-axis correspond to the times t_1, t_2, t_3 given in Fig. 4.14.

While the CBC minimizes $\max e_{u_x}$ over the LODI scheme regardless of the chosen mesoscopic BC, it leads to a slightly less accurate steady state after about 8000 iterations. Furthermore, the CBC does not benefit as much as the LODI scheme when the NEEP BC is used over EBC.

PML As Fig. 4.18 shows, the improvement obtained from switching the mesoscopic BC from the EBC to NEEP can be retained when the LODI BC is applied

in the PML approach. Using the parameters $W = 20, \sigma_{\max} = 0.001$, enabling PML for a given mesoscopic BC results in smaller maximum global errors and using the NEEP BC improves over the EBC regardless of PML.

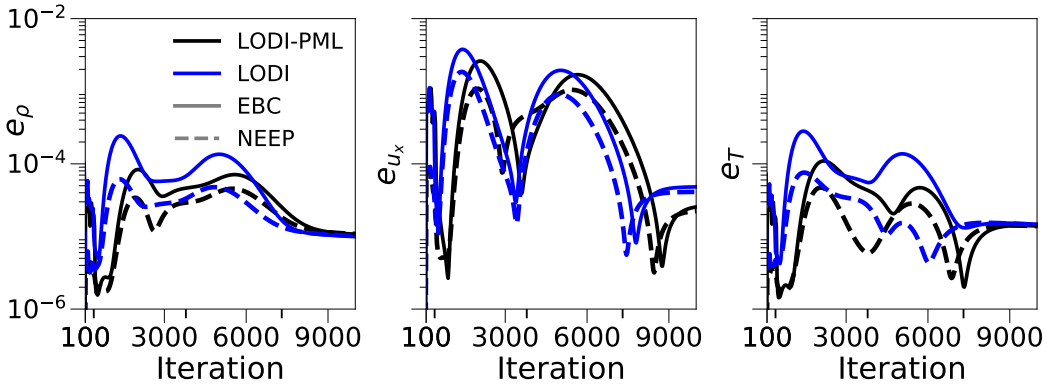

FIGURE 4.18: Error evolution in the temperature step benchmark for the D2Q17 stencil. LODI BC used with EBC (solid lines) and NEEP BC (dashed lines). PML was used with a fixed width of the damping zone $W = 20$ and $\sigma_{\max} = 0.001$ in conjunction with LODI. The minor ticks on the x-axis correspond to the times t_1, t_2, t_3 given in Fig. 4.14.

Comparison The global error evolutions of selected instances of NRBCs are shown in Fig. 4.19. At almost any given time step, the errors obtained using the ZG BC are between one and two orders of magnitude larger than errors obtained with any NRBC. The combination ZG and PML improves this, giving lower error levels than the DABC at either value of $H_{\max} \in \{30, 90\}$. These error levels are comparable to the ones obtained using the LODI BC with mesoscopic NEEP BC. Using the latter in conjunction with PML gives a further small improvement in accuracy.

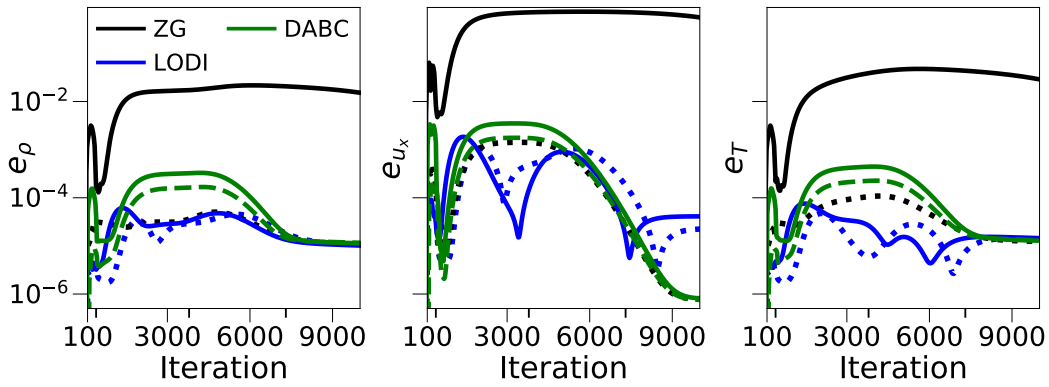

FIGURE 4.19: Direct comparison of the evolution of the global errors for various BC. The PML is deployed with $W = 20$ and $\sigma_{\max} = 0.001$ for LODI (in conjunction with the mesoscopic NEEP BC) and $\sigma_{\max} = 0.3$ for ZG (dotted lines). The DABC is used with $H_{\max} = 30$ (solid line) and $H_{\max} = 90$ (dashed line) using the initialization (4.1). The minor ticks on the x-axis correspond to the times t_1, t_2, t_3 given in Fig. 4.14.

As was done in the first benchmark, the relative increase in accuracy is measured by the quantity $\hat{e}_Z$ defined in Eq. (4.33), which is plotted against the relative increase in runtime $\hat{t}$ with respect to the ZG BC in Fig. 4.20. The ZG BC benefits from usage in conjunction with the PML technique, reducing the maximum errors obtained

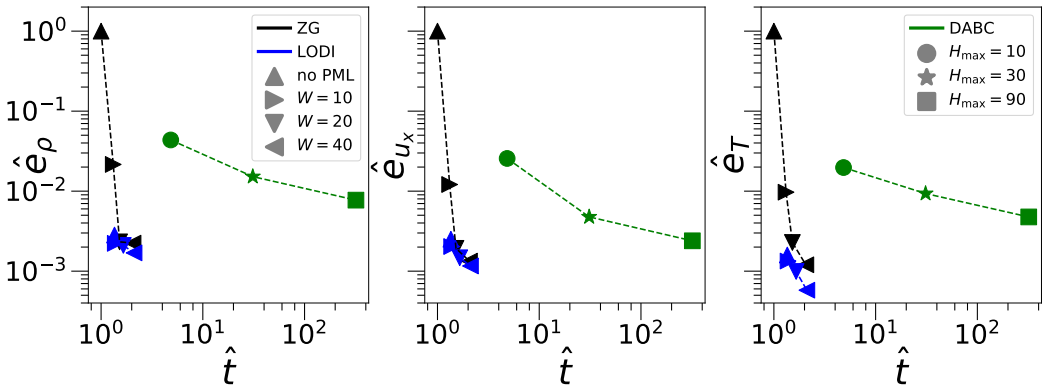

FIGURE 4.20: Accuracy vs performance evaluation of the various BC for a computational domain $L_x \times L_y = 200 \times 20$. Plotted is the relative increase in runtime $\hat{t}$ with respect to the ZG BC versus the maximum value of e_ρ (left),e_{u_x} (middle) and e_T (right) respectively, normalized with respect to the ZG BC. The PML is used with $\sigma_{\max} = 0.001$ for LODI (in conjunction with the mesoscopic NEEP BC) and $\sigma_{\max} = 0.3$ for ZG. The DABC is used with the initialization (4.1).

by three orders of magnitude at the price of an almost doubled runtime. The computational cost of the DABC is much higher: With $H_{\max} = 10$, the DABC reduces the maximum errors by more than one order of magnitude but requires almost ten times more runtime. Using $H_{\max} = 90$, reductions of two orders of magnitude are obtained but the runtime grows by a factor of 400 with respect to the base case. For the LODI scheme, only a small reduction of maximum errors is observed when the width of the dampening zone is increased. However, among the NRBCs considered, the LODI scheme in conjunction with PML and the mesoscopic NEEP BC reduces the runtime required to achieve any given reduction level of the baseline errors.

This result highlights that while usage of the PML makes simple – potentially reflective – BCs feasible, there is a computational benefit from making use of NRBCs beyond the dampening layers.

4.4.3 2D Vortex propagation

Here, the propagation of a vortex is simulated and its interaction with the boundary is analysed. Unlike the benchmarks previously considered, this flow has fully two-dimensional dynamics. In this setting, it is more difficult to design a NRBC: In a one-dimensional flow, there is only one possible direction along with reflections may occur while in two spatial dimensions, reflections may occur at an arbitrary angle.

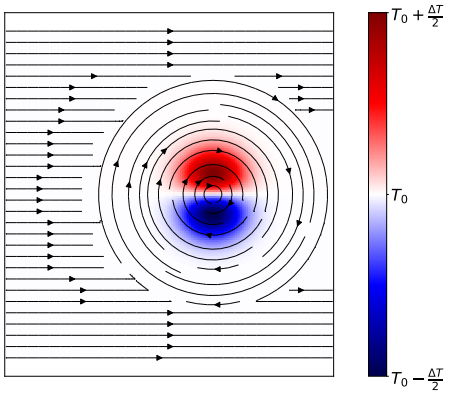

FIGURE 4.21: Initial setup for the thermal vortex benchmark. Uniform background velocity $\mathbf{u_0} = \begin{pmatrix} \mathrm{Ma} \cdot c_s, & 0 \end{pmatrix}^\top$ and uniform background temperature $T_0 = 1$ are perturbed according to (4.38) in a circle with centre $(\hat{x}_0, \hat{y}_0)$, radius $\hat{r} = 0.7$ and vortex strength parameter $b = \frac{3}{20}$. The Mach number is set to $\mathrm{Ma} = 0.1$. In this setup, $\Delta T \approx 0.0235$.

The initialization of the problem is described in normalized spatial coordinates $(\hat{x}, \hat{y}) \in [-1, 1]^2$:

$$\hat{x} = \frac{2(x-1)}{L_x - 1} - 1, \quad \hat{y} = \frac{2(y-1)}{L_y - 1} - 1. \tag{4.36}$$

The initial centre of the vortex is defined by:

$$(\hat{x}_0,\, \hat{y}_0) = \left(\tfrac{K}{L_x - 1},\, 0\right),$$

where the parameter K defines $x-$position of the vortex on the horizontal centre line.

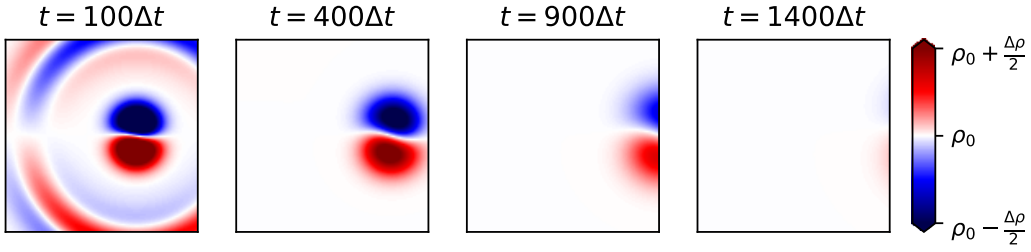

FIGURE 4.22: Snapshots of reference density fields ρ^{ref}. The time steps correspond to i) shortly after the simulation begins, ii) before the vortex-boundary interaction starts, iii) during the interaction of the vortex centre with the boundary, iv) shortly before the vortex leaves the domain of interest.

The thermal vortex is formed by a perturbation of both the temperature T around T_0 and velocity $\mathbf{u}$ around $\mathbf{u}_0$ within a circle at $(\hat{x}_0,\, 0)$ with radius $\hat{r}$ against a uniform background flow. With this, the initial macroscopic fields are given as

$$\begin{aligned}
&\rho(x, y) = \rho_0, \\
&\mathbf{u}(x, y) = \mathbf{u_0} + \begin{cases} 0 & \text{if } (\hat{x} - \hat{x}_0)^2 + \hat{y}^2 \geq \hat{r}^2 \\ \mathbf{v}(\hat{x} - \hat{x}_0, \hat{y}) & \text{otherwise,} \end{cases} \\
&T(x, y) = T_0 + \begin{cases} 0 & \text{if } (\hat{x} - \hat{x}_0)^2 + \hat{y}^2 \geq \hat{r}^2 \\ \hat{y}\, \theta(\hat{x} - \hat{x}_0, \hat{y}) & \text{otherwise,} \end{cases}
\end{aligned} \tag{4.37}$$

where the initial perturbations are set in dependence of a control parameter b as

$$\mathbf{v}(x, y) = \frac{5 c_s \text{Ma}}{2} 2^{-\frac{x^2+y^2}{b^2}} \begin{pmatrix} y \\ -x \end{pmatrix}, \quad \theta(x, y) = \frac{5 c_s \text{Ma}}{2} 2^{-\frac{x^2+y^2}{b^2}}. \tag{4.38}$$

The initial setup is illustrated in Fig. 4.21. In Fig. 4.22, snapshots of the reference density field ρ^{ref} are given for selected time steps. After 100 iterations, a density pulse is propagating due to the initial perturbation. At about 400 iterations, the vortex starts interacting with the boundary and its centre is passing the boundary at around 900 iterations. After 1400 iterations, the vortex almost completely left the domain of interest and only small deviations from the uniform background density ρ_0 remain.

DABC Among the initialization strategies tested, the only feasible way to initialize the sub-problems is given by DABC-A, i.e. Eq. (4.1). Both DABC-B and DABC-C

lead to initial discontinuities in the corners of the sub-problems domain (see Fig. 4.3) which in turn introduce severe oscillations in the bulk. As seen from Fig. 4.23, increasing the value of $H_{\max}$ only has a small impact on the global errors obtained.

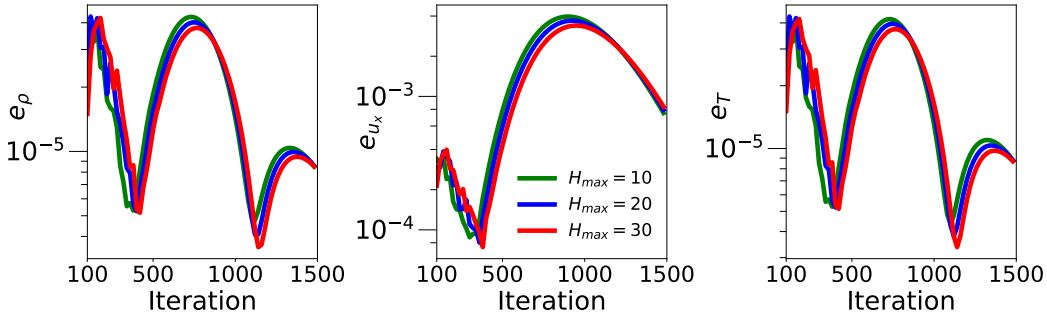

FIGURE 4.23: Error evolution in the thermal vortex benchmark using DABC-A (4.1) with various values of $H_{\max}$.

CBC When inspecting the various implementations of characteristic BCs, the right-hand side boundary is subsequently equipped with the perfectly non-reflecting LODI and CBC are compared with the CBC-RELAX scheme (see Tab. 4.1). In the later scheme, the single incoming wave amplitude at the right-hand side boundary is set by Eq. (4.16) with $\alpha = 0, \beta = \text{Ma}$. This choice has been taken from [79]. All the other face boundaries and corners are treated using the LODI scheme (see Fig. 4.6). This is because instabilities occurred near the corner nodes on evaluating transversal terms in both directions.

Role of the mesoscopic BC

The error evolutions obtained with these three characteristic based BCs are presented in Fig. 4.24 for both the mesoscopic EBC and NEEP BC. It is seen that accounting for viscous and transversal terms in the perfectly non-reflecting CBC has only a small positive effect on the obtained accuracy, as the obtained curves are visually matching for most of the iterations. Making use of the CBC-RELAX scheme instead, the error curves are reduced by about one order of magnitude between iterations 400 and 1000. It is stressed that the only difference between CBC and CBC-RELAX is the way the inward pointing waves amplitudes (here only $\bar{\mathcal{L}}_{x,3}$) are set.

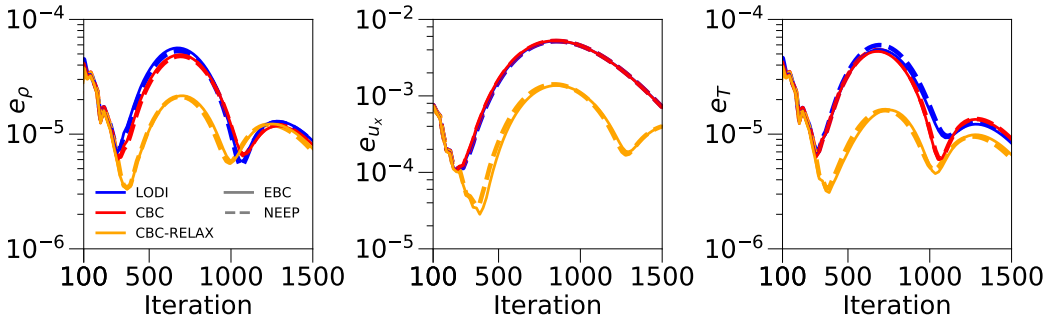

FIGURE 4.24: Error evolution in the thermal vortex benchmark using various characteristic based BCs in conjunction with the mesoscopic NEEP BC (dashed lines) and EBC (solid lines).

In contrast to the results obtained for the one-dimensional flows considered in Sec. 4.4.1 and Sec.4.4.2, here the characteristic based BCs yields similar errors levels

obtained using the EBC and NEEP BC. This is because in the NEEP BC, constant extrapolation is performed along the direction normal to the boundary, which is the only direction macroscopic information travels along in a stratified flow with one-dimensional dynamics. However, this procedure introduces additional errors in the case of two-dimensional flow dynamics.

Evaluation of viscous terms

The proposed evaluation of viscous terms is found to be crucial to ensure numerical stability over a broad range of numerical viscosities ν. To illustrate this, simu-

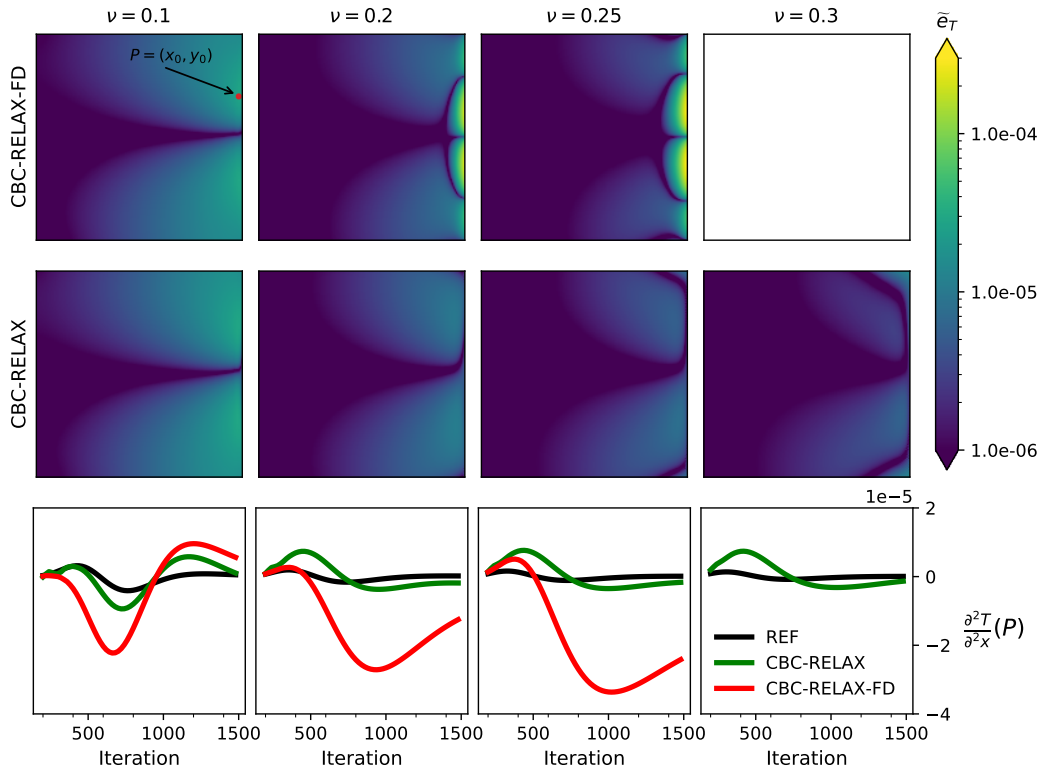

FIGURE 4.25: Upper and middle panels show heat maps of $\widetilde{e}_T$ after 1200 iterations at various numerical viscosity ranging from $\nu = 0.1$ (first column) to $\nu = 0.3$ (right column). The lower panel shows the time evolution of the quantity $\frac{\partial^2 T}{\partial x^2}$ computed at $P = (x_0, y_0)$ marked in red in the top left panel. Increasing the numerical viscosity, the coupling between the macroscopic solver on the boundary and the LBM gives rise to instability when the Laplacian is evaluated directly at the macroscopic level rather than at the mesoscopic one, leading to a failed simulation at $\nu = 0.3$.

lations at various values of ν have been conducted using a CBC formulation where instead of making use of Eqns. (4.20) and (4.21), the Laplacians of temperature and velocity are approximated using the second order finite differences

$$\frac{\partial^2 \mathbb{U}_i(\mathbf{x}_b^{(\mathcal{M}-1)}, t)}{\partial^2 x} \approx 2\mathbb{U}_i(\mathbf{x}_b^{(\mathcal{M}-1)}, t) - 5\mathbb{U}_i(\mathbf{x}_b^{(\mathcal{M}-1)} - \mathbf{e}_x, t) + 4\mathbb{U}_i(\mathbf{x}_b^{(\mathcal{M}-1)} - 2\mathbf{e}_x, t) - \mathbb{U}_i(\mathbf{x}_b^{(\mathcal{M}-1)} - 3\mathbf{e}_x, t) \tag{4.39}$$

for the outermost boundary node and the central formula

$$\frac{\partial^2 \mathbb{U}_i(\mathbf{x}_b^{(k)}, t)}{\partial^2 x} \approx \mathbb{U}_i(\mathbf{x}_b^{(k)} + \mathbf{e}_x, t) - 2\mathbb{U}_i(\mathbf{x}_b^{(k)}, t) + \mathbb{U}_i(\mathbf{x}_b^{(k)} - \mathbf{e}_x, t) \tag{4.40}$$

for the inner boundary nodes at $k = 0, 1, \ldots, \mathcal{M} - 2$. The resulting scheme is referred to with the suffix -FD. Note that this scheme can be used when working with lower order stencils which do not allow to recover high order moments.

In the first two rows of Fig. 4.25, heat maps of $\widetilde{e}_T$ after 1200 iterations for several different values of the kinematic viscosity are shown for the CBC-RELAX and CBC-RELAX-FD scheme. In the last row of this figure, the time evolution of the quantity $\frac{\partial^2 T}{\partial x^2}$ evaluated at point $P = (x_0, y_0)$ in proximity of the right-hand side boundary (cf. top left panel in Fig. 4.25) is given. For $\nu = 0.1$, similar heat maps are obtained for both schemes while there exists a notable difference in the derivatives evaluated in P. Increasing the numerical viscosity, temperature derivatives used with the CBC-RELAX-FD scheme exhibit growing differences from the reference curve and the heat maps of $\widetilde{e}_T$ show significant pointwise errors at the right-hand side boundary. Eventually numerical instabilities lead to a failed simulation at $\nu = 0.3$. In contrast, the CBC-RELAX scheme in its proposed form does not suffer from this problem and gives accurate and stable predictions of the fluid fields.

Comparison The time evolution of global errors of selected instances of NRBCs is shown in Fig. 4.26. Note that the corner treatment of the ZG BC simply consists of imposing all the populations from the adjacent fluid node on all the corner nodes (see Fig. 4.6).

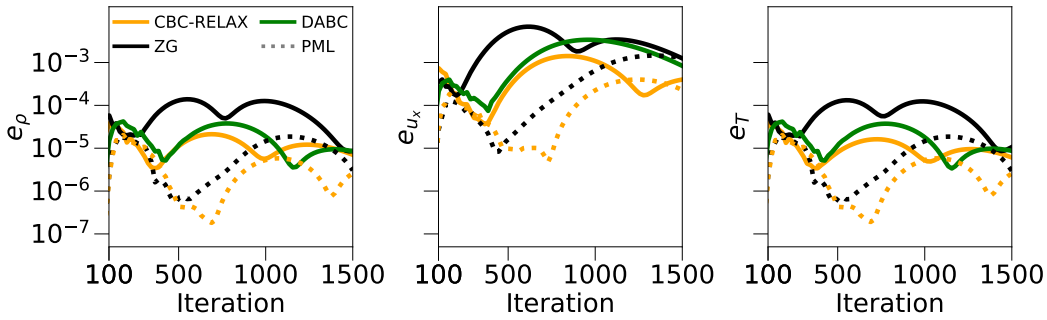

FIGURE 4.26: Direct comparison of the evolution of the global errors for various BC. The PML is deployed with $W = 20$ and $\sigma_{\max} = 0.0005$ for CBC-RELAX (in conjunction with the mesoscopic NEEP BC) and $\sigma_{\max} = 0.01$ for ZG (dotted lines). The DABC is used with $H_{\max} = 30$ using the initialization (4.1).

While the ZG BC gives poorest accuracy, it outperforms both the CBC and the DABC on combining it with the PML technique. The accuracy is further improved if the PML is combined with the CBC. Usage of PML or DABC leads to a slightly delayed increase in the global errors during the first 150 iterations.

The reason for this can be seen from Fig. 4.27, where the pointwise errors $\widetilde{e}_\rho$ are shown at selected time steps. Both the PML and the DABC are able to absorb the spherical pressure pulse that is created due to the initial conditions, while the ZG and CBC-RELAX BCs create notable reflections at all edge boundaries (Fig. 4.27-first column). As the vortex starts interacting with the boundary (second column), the reflections occurring from the CBC-RELAX scheme have largely dissipated and there are only small errors close to the boundary. In contrast, the reflections caused by the

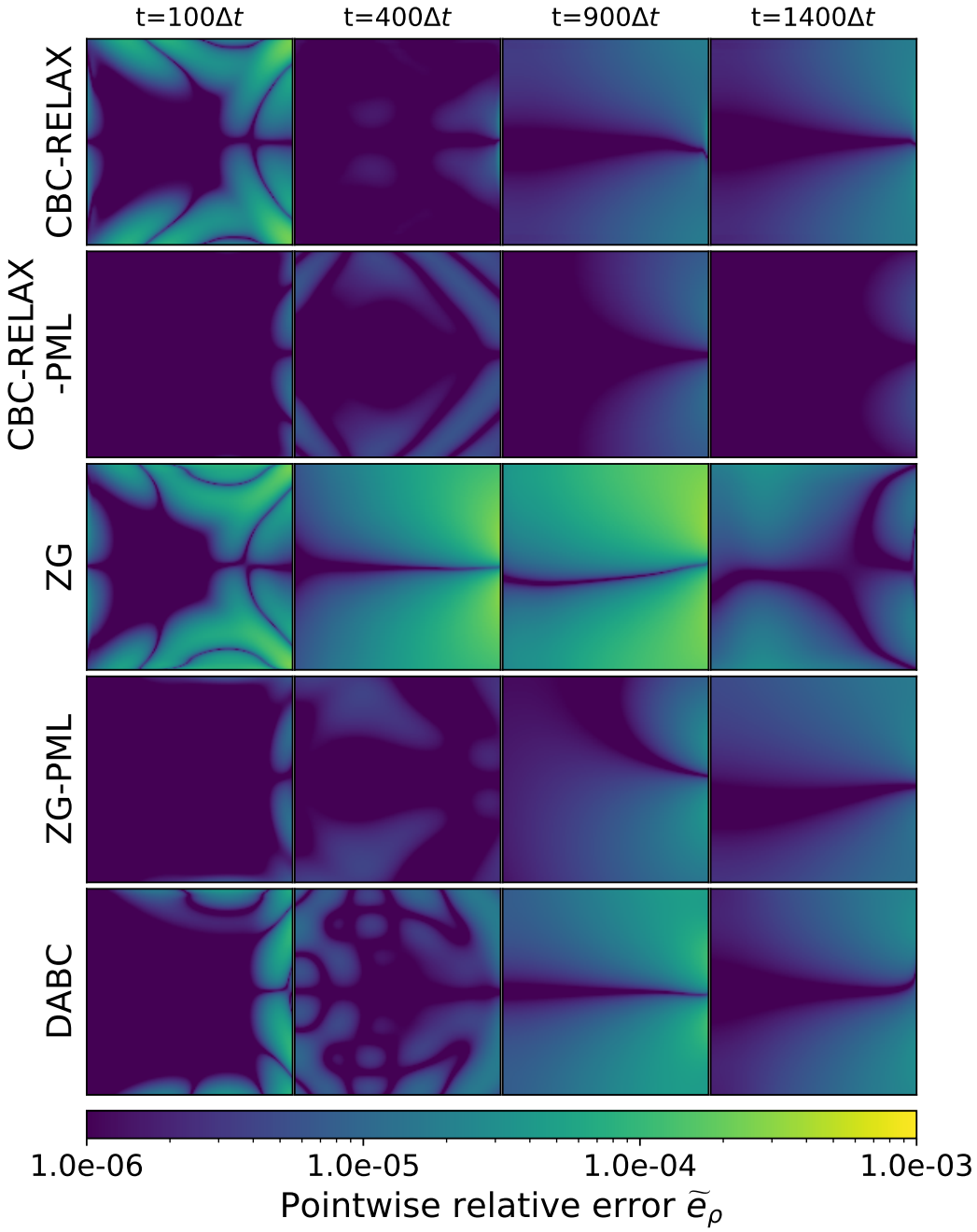

FIGURE 4.27: Direct comparison of the pointwise relative errors in density. The selected time steps correspond to the time steps given in Fig. 4.22. The CBC-RELAX BC was used with the mesoscopic NEEP BC. Results using PML are obtained using $W = 20$ and $\sigma_{\max} = 0.0005$ ($\sigma_{\max} = 0.01$) for CBC (ZG).

ZG BC pollute the entire computational domain. Also using the DABC, almost the entire domain is visibly affected by errors caused by reflection, albeit one order of magnitude smaller ones. At this point, using PML in conjunction with the CBC-RELAX BC gives rise to small scale errors at the upper and lower boundaries.

During the vortex-boundary interaction (third column), all BCs but the combination CBC-RELAX and PML result in notable pointwise errors of order about 10^{-4} in the entire bulk. The latter combination only gives errors of magnitude 10^{-5} in the right-hand side of the computational domain.

As the vortex leaves the domain of interest (last column), this combination also gives the closest approximation to the reference state.

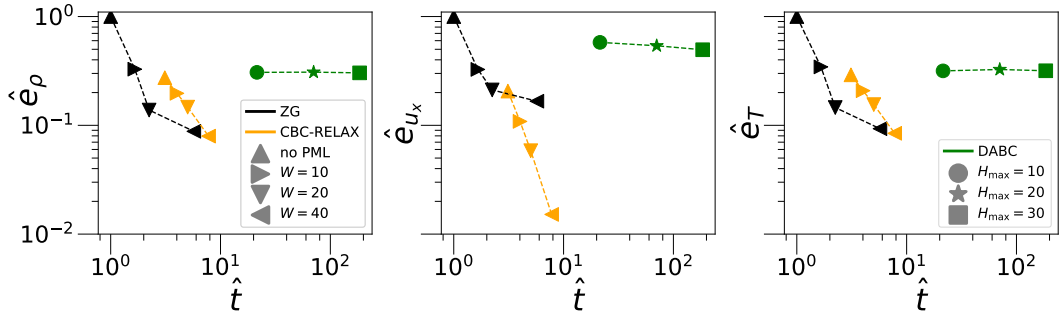

FIGURE 4.28: Accuracy vs performance evaluation of the various BC for a computational domain $L_x \times L_y = 150 \times 150$. Plotted is the relative increase in runtime $\hat{t}$ with respect to the ZG BC versus the quantities $\hat{e}_Z$ defined in Eq. (4.33). The PML is used with $\sigma_{\max} = 0.0005$ for the CBC-RELAX BC (in conjunction with the mesoscopic NEEP BC) and $\sigma_{\max} = 0.01$ for ZG. The DABC is used with the initialization (4.1).

In Fig. 4.28, the relative runtime $\hat{t}$ of the various NRBCs with respect to the naive ZG BC is plotted against the benefit in accuracy as given by $\hat{e}_Z$ (Eq. (4.33)).

As the grid is now extended along two spatial dimensions, using the PML has a higher impact on the runtime than in the previous benchmarks.

The maximum errors caused by the ZG BC can be reduced by about one order of magnitude when the PML is applied. The combination of ZG BC and PML consumes the least amount of runtime if one is content with a gain in accuracy of about one order of magnitude. Beyond this, diminishing returns with respect to accuracy are observed as the width of the dampening zone is increased further.

The CBC can give further reductions in maximum errors. However, the runtime with respect to the base case is increased by a factor of ten if a reduction of more than one order of magnitude is required.

For the DABC, the choice $H_{\max} = 10$ and $H_{\max} = 30$ lead to ten and 100 times longer simulations. However, the DABC gives a nearly constant level of error at history depth tested, giving a reduction to about thirty percent of the baseline error.

Corner treatment in the CBC In order to assess the impact the approximate treatment of corners has on simulation results, the propagation of an iso-thermal vortex is considered. The numerical setup is exactly the same as for the thermal flow discussed above, with the only difference that a uniform temperature profile is initialized and kept constant during the time evolution of the flow. Doing so allows to compare the results of simulations from multi-speed models with those given by the single-speed D2Q9 model. Since the D2Q9 does not correctly capture the heat-flux, the CBC-RELAX-FD scheme, where Eqns. (4.39) and (4.40) are used instead of

Eqns. (4.20) and (4.21), is used. The corner treatment for the D2Q9 is analogous to the multi-speed case (c.f. Fig. 4.6), albeit simpler, since target quantities $\mathbb{U}$ need to be calculated for one single corner node only.

In order to allow for a direct comparison between the different stencils, results are given at the re-scaled time $t^* = \lfloor 150 c_s^{17}/c_s^q \rfloor \quad q \in \{9, 17, 37\}$, where c_s^q is the speed of sound in the lattice for the different stencils (see Sec. 2.4.1). A time step where reflections caused at the outlet and lateral boundaries are interacting with each other close to the corners is chosen to put stress on the corner BC.

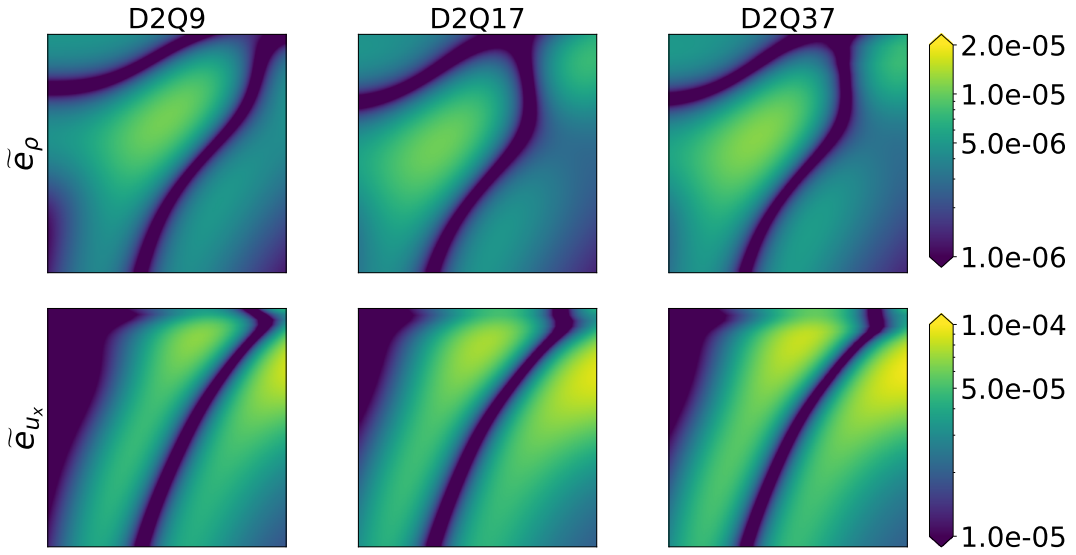

FIGURE 4.29: Comparison of pointwise relative errors obtained in the simulation of an iso-thermal vortex using the D2Q9, D2Q17 and D2Q37 velocity stencil. Shown is a subset of the computational domain, i.e. a square with a side-length of 50 nodes whose upper right corner coincides with the upper right corner of the full domain.

In Fig. 4.29 heat maps for both quantities $\widetilde{e}_\rho$ and $\widetilde{e}_{u_x}$ are shown. The dynamic obtained with the D2Q9 stencil closely resembles the one provided by multi-speed stencils, with differences observed close to the right-hand side corners. Nevertheless, the pointwise errors in the proximity of the corners are of the same order of magnitude as in the remaining points close to the outlet. Therefore, it is concluded that at least for this benchmark, the extra source of inaccuracy given by the corner treatment in multi-speed stencils is negligible.

4.4.4 Angular wave

In this section, an impinging plane wave that approaches the boundary at an angle ϕ is considered. The angle is given with respect to the vertical midplane; i.e., $\phi = 0$ states that the plane wave propagates in the direction normal to the boundary. In this benchmark, the relevance of transversal information is gradually increased as the value of ϕ increases. The initial setup is conveniently described in shifted coordinates

$$\begin{pmatrix} \hat{x}(x,y) \\ \hat{y}(x,y) \end{pmatrix} = \begin{pmatrix} \cos(\phi\frac{\pi}{180}) & \sin(\phi\frac{\pi}{180}) \\ -\sin(\phi\frac{\pi}{180}) & \cos(\phi\frac{\pi}{180}) \end{pmatrix} \begin{pmatrix} x \\ y \end{pmatrix}$$

and reads

$$\rho(x,y) = \rho_0, \quad \mathbf{u}(x,y) = \mathbf{u_0}, \quad T(x,y) = T_0 + \frac{1}{100}\exp(\frac{-\hat{x}(x,y)^2}{2s^2}).$$

In the above, $\rho_0 = T_0 = 1, \mathbf{u_0} = \begin{pmatrix} 0, & 0 \end{pmatrix}^\top$ and $s = \frac{1}{50}$.

As the simulation develops, the initial temperature spike dissipates, while two pressure (temperature) pulses travel in positive and negative $x-$ direction respectively. Exemplary snapshots of the temperature profiles at times t_0, t_1, t_2 are shown in Fig. 4.30, showing the initial state and the state before and after the boundary interaction of the angular wave.

From these time steps, reflection coefficients are computed for various angles ϕ to evaluate the BCs ability to absorb outgoing waves. To this end, simulations with various values of ϕ are run. For each run, the wave amplitudes I_Z of $Z \in \{\rho, u_x, T\}$ along the horizontal midplane $y = \frac{L_y}{2}$ are computed at t_1 and t_2, that correspond to shortly before and right after the interaction with the boundaries. The reflection coefficient is then computed as

$$R_Z = \frac{I_Z(t_2)}{I_Z(t_1)}.$$

Upper and lower boundaries are periodic, while artificial boundaries are set at the left and right-hand side of the domain. Simulations are conducted using a numerical viscosity of $\nu = 0.1$ on a $L_x \times L_y = 200 \times 700$ grid. The domain is chosen to be sufficiently large to ensure that the measurements at the horizontal midplane are not polluted by artefacts stemming from the periodicity of the upper and lower boundaries.

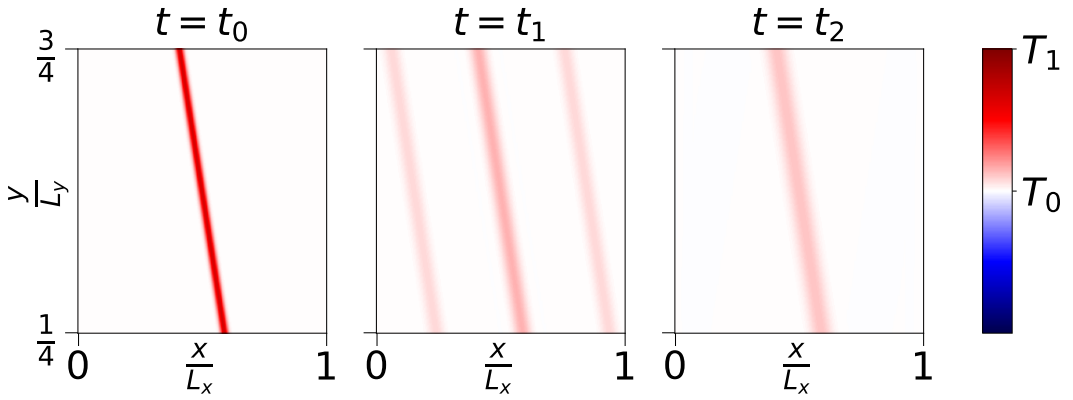

FIGURE 4.30: Temperature fields obtained at various time steps. The left panel depicts the initial state at time t_0. The times t_1 and t_2 correspond to before and after waves interacted with the left hand side boundary at height $y = \frac{L_y}{2}$ respectively.

The reflection coefficients with respect to the density, R_ρ, are given in five degree increments over the range of $0° - 40°$ in Fig. 4.31.

In the left hand side panel, results obtained using the DABC with $H_{\max} = 10$ in conjunction with initialization strategies given by Eqns (4.1),(4.2) and (4.3) respectively are shown. Furthermore, the reflection coefficients for the perfectly non-reflecting characteristic based schemes LODI and CBC are are given. It is observed that initializing the DABC sub-problems according to Eq. (4.1) gives significantly

larger values of the reflection coefficient than the other initialization strategies. However, any version of the DABC falls short of the perfectly non-reflecting characteristic based BCs. The CBC gives a small improvement over the LODI BC, as it also makes use of transversal information. The reflection coefficients obtained using the NEEP BC instead of the EBC to pose the target values obtained in the CBC are visually matching those presented and are omitted.

The right-hand side panel of Fig. 4.31 introduces the results obtained using the ZG BC for reference. This BC causes by far the largest reflection among the BCs considered here. However, on combining it with the PML approach, a performance similar to the DABC is obtained. At angles below 15°, even the CBC is outperformed. However, on combining the PML with the CBC, the overall smallest reflections are obtained. The coefficients R_{u_x} and R_T describe essentially the same situation and are thus omitted here.

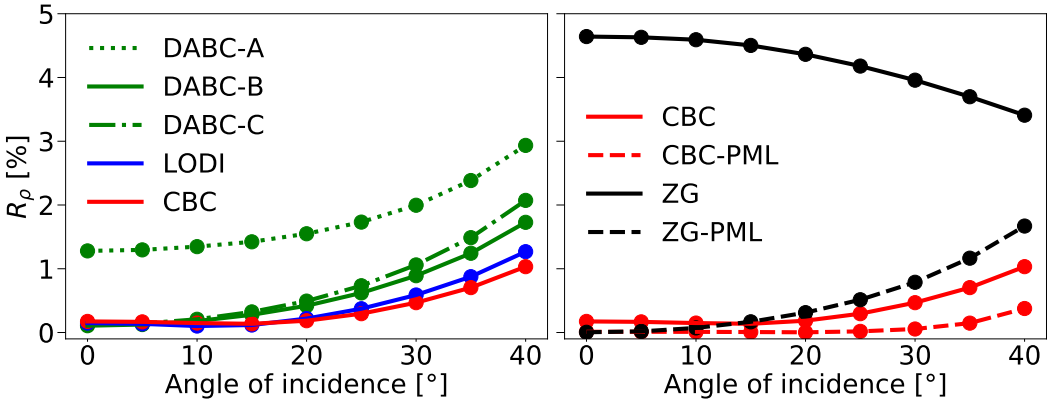

FIGURE 4.31: Reflection coefficients obtained using various BC. The perfectly non-reflecting LODI and CBC schemes were applied. Used parameters for the remaining BCs: $H_{\max} = 10$ for the DABC, $W = 20$ for the PML. For the PML results, $\sigma_{\max} = 0.0001$ has been set in conjunction with the CBC and $\sigma_{\max} = 0.2$ for the ZG BC.

4.4.5 Vortex Shedding

In this benchmark, a stationary heated rectangular obstacle with $T_{\text{obstacle}} > T_0$ consisting of $O_x \times O_y$ lattice nodes is placed in the centre of a square computational domain of size $L \times L$. Due to vortex shedding at the obstacle, vortices form at the obstacle and propagate downstream.

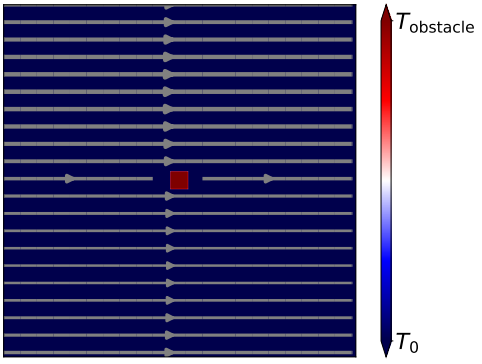

FIGURE 4.32: Initial temperature field and streamlines of perturbed initial velocity field. The width of the streamlines corresponds to their magnitude.

The initial macroscopic fields shown in Fig. 4.32 read

$$\rho(x,y) = \rho_0, \quad \mathbf{u}(x,y) = \left(u_0 + \alpha \sin(2\pi \tfrac{y}{L_y}), 0\right)^\top, \quad T(x,y) = T_0,$$

where the stream-wise velocity field was perturbed to trigger the instability causing the formation of the vortices faster [95].

The obstacle was treated using the diffusive BC discussed in 3.1.4. The external NEBB-SE BC discussed in Sec. 3.2 is applied at the left-hand side boundary to impose velocity $\mathbf{u}$ and temperature T_0 at the inlet. Here, the conservation of mass is not enforced in the NEBB scheme, as mass flux may occur over this open boundary. The remaining boundaries are equipped with an NRBC. The numerical values for the simulation parameters are

$$\mathrm{Re} = 100, \mathrm{Ma} = 0.1, \rho_0 = T_0 = 1, T_{\text{obstacle}} = 1.1, \alpha = 0.005 \text{ and } O_x = O_y = 20,$$

where the Reynolds number was computed using the side length of the square obstacle $L = O_x$.

Impact of NRBC on the pressure field First, the NRBCs ability to absorb the vortices is inspected. Qualitative results of the impact of the NRBC used at the three edge boundaries and corners are reported in Fig. 4.33, where the macroscopic pressure after 30.000 iterations is shown in conjunction with iso-contours of the absolute value of vorticity.

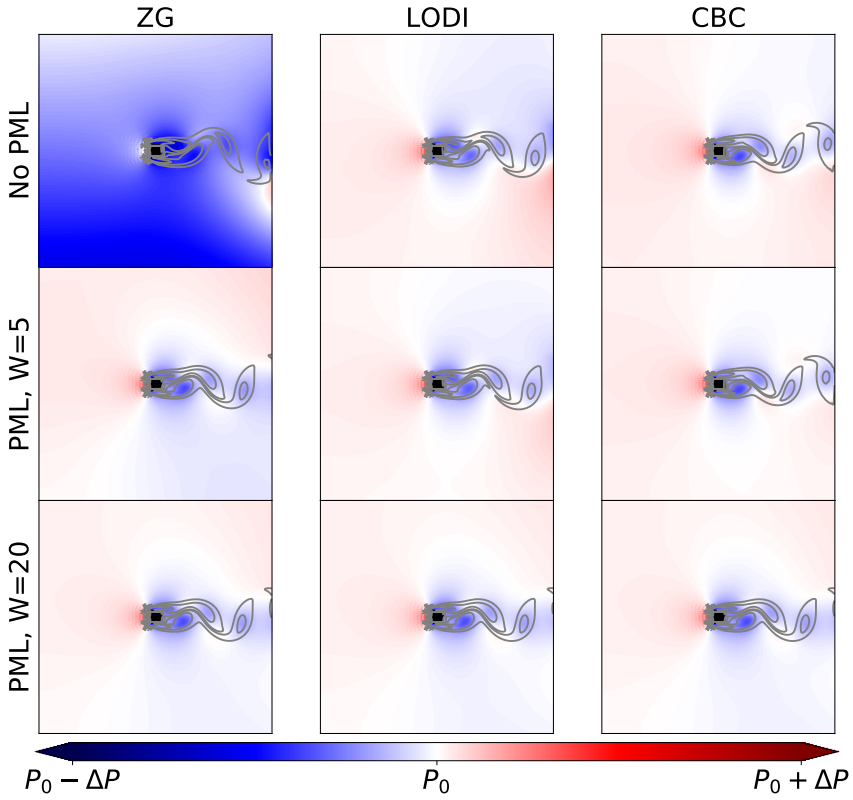

FIGURE 4.33: Snapshots of pressure $p = \rho T$ after 30.000 iterations for $L = 400$ and $\mathrm{Re} = 100$. Numerical values are $p_0 = 1, \Delta p = 0.0149$. Iso-contours of vorticity are shown. The PML was used with $\sigma_{\max} = 0.1$.

In the first row, the situation without usage of PML is shown. Using the ZG BC, the pressure in almost the entire computational domain is lower than the pressure of the background flow. Furthermore, the vortices are distorted when interacting with the boundary. Both problems are alleviated when using either the LODI or CBC scheme. A small pressure distortion close to the right-hand side boundary is still observed in the LODI BC. Due to the incorporation of transversal information, the CBC scheme is capable of modelling the vortex-boundary interaction in a more accurate way.

In the middle row, the BCs have been used in conjunction with the PML approach, where a padding of $W = 5$ nodes and a maximum dampening coefficient $\sigma_{\max} = 0.1$ have been used. For the ZG scheme, this significantly improves the pressure field and the iso-contours of vorticity are now closer to the ones obtained in the LODI scheme. However, the lower right part of the computational domain exhibits a pressure below the reference value P_0. The small reflection observed in the LODI scheme without PML is further reduced, while using the CBC in conjunction with this thin PML yields negligible only differences to the case of the CBC without PML.

In the lower row, the padding has been increased to $W = 20$ nodes. In this setting, no significant differences can be observed between the various BC. For the CBC, the pressure obtained in the lower right part of the computational domain becomes slightly lower than using a thinner PML. Furthermore, it is seen that the thicker PML prevents the CBC from making use of its ability to capture the vortex-boundary interaction as the absorbing layers dampen out the vortices before.

It is concluded that the impact of the BC becomes negligible for sufficiently thick PML zones, in which case a simple and computationally effective BC should be preferred over NRBCs. However, using an NRBC beyond the absorbing layers allows for usage of thinner dampening zones.

Impact of NRBC on drag and lift coefficients To quantify the accuracy of the NRBCs used at the edges of the computational domain, the drag and lift coefficients at the solid obstacle are tracked. They are given as [96]

$$C_D = \frac{2|F_x|}{\rho U^2 L}, \quad C_L = \frac{2F_y}{\rho U^2 L}, \tag{4.41}$$

where $\mathbf{F} = \begin{pmatrix} F_x & F_y \end{pmatrix}^\top$ denotes the total force acting on the obstacle.

Using the momentum exchange method [96–98], this force can be calculated as

$$\mathbf{F} = \sum_{\mathbf{x}_b \in B} \sum_{i=1}^{d} \left(\mathbf{c}^{(\bar{i})} f_{\bar{i}}(\mathbf{x}_b, t) - \mathbf{c}^{(i)} f_i(\mathbf{x}_b + \mathbf{c}^{(\bar{i})}, t) \right) \cdot h(\mathbf{x}_b + \mathbf{c}^{(\bar{i})}).$$

In the above, the set B includes all the nodes forming the obstacle. The boolean function $h(\mathbf{x})$ returns zero (one) if $\mathbf{x}$ is a solid (fluid) node and $\mathbf{c}^{(\bar{i})} = -\mathbf{c}^{(i)}$ is the mirror conjugate of a given population. That is, the momentum exchanged over all lattice links between solid nodes and neighbouring fluid nodes is calculated.

In Fig 4.34, the time evolutions of C_L and C_D are given for $L = 400$ and the ZG, LODI and CBC schemes. They are compared with reference results obtained using the CBC and $L = 4000$. As the size of the computational domain is increased, the impact of the BC used for the edges and corners of the computational domain on the evolution of C_D and C_L becomes less significant. At this coarse grid, where the obstacle is rather close to boundary, the BC fails to capture the sinusoidal shape in the time evolution of C_D and overestimates the amplitude in C_D by a factor of about

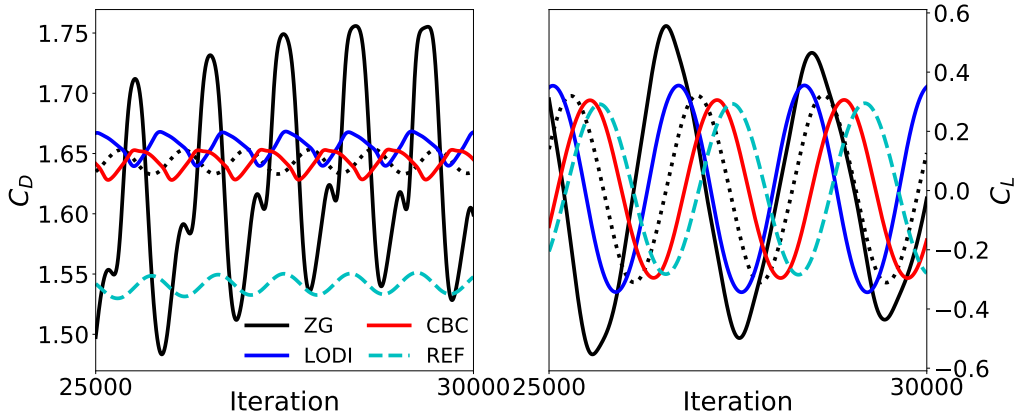

FIGURE 4.34: Time evolution of C_D and C_L at the obstacle for various BCs used at the boundaries and Re $= 100$ at $L = 400$. In all simulations, the obstacle was treated using the diffusive BC. The dotted black line represents results obtained with the ZG BC and PML with $W = 20$ and $\sigma_{\max} = 0.1$. The other BCs in conjunction with the PML gave visually matching results and are thus omitted.

ten. This is improved upon in the combination with PML, which gives results comparable to the LODI and CBC schemes. All three schemes capture the sinusoidal shape and amplitude with similar accuracy but at a constant offset of about ten percent of the average value of C_D. The situation is similar for the lift coefficient C_L, where the sinusoidal shape is captured by all schemes but the ZG gives the largest overestimation of the amplitude.

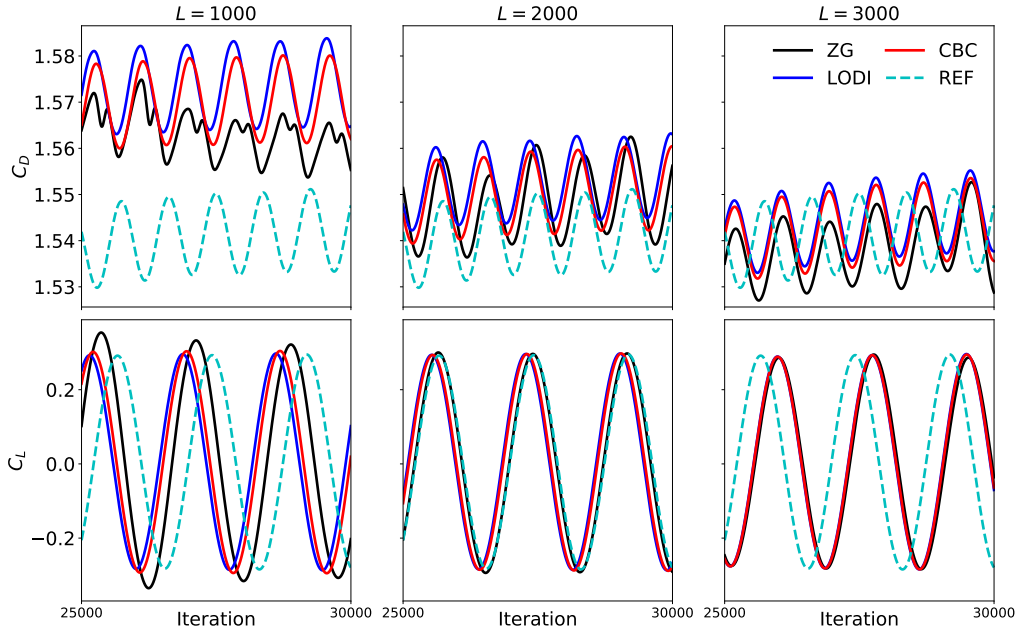

FIGURE 4.35: Time evolution of C_D and C_L at the obstacle for various BCs used at the boundaries and Re $= 100$. In all simulations, the obstacle was treated using the diffusive BC.

The motivation for usage of NRBCs is to obtain a simulation at a given level of accuracy on the smallest domain size possible. In that spirit, to further inspect the advantages of the NRBC, it is checked which distance between boundary and obstacle is necessary for the ZG BC to qualitatively capture the correct drag and

lift coefficients. To this end, the time evolution of both C_D and C_L for square sizes $L \in \{1000, 2000, 3000\}$ is shown in Fig 4.35.

In the ZG BC, the issues observed for $L = 400$ are still present at $L = 1000$, as the time evolution of C_D is still not following a sinusoidal profile. This is consistent to the findings in [21]. While this issue is resolved for $L \geq 2000$, the amplitude in the curve describing the drag coefficient still varies notably. It can be seen that enlarging the grid leads to a phase shift in the sinusoidal evolution of the drag and lift coefficients, which causes the curves for C_L to coincide with the reference for $L = 2000$. However, on further increasing the grid size to $L = 3000$, the curve are out of sync again while keeping the correct amplitude.

In conclusion, the usage of a NRBC allowed to qualitatively capture the evolution of C_L and C_D on a grid consisting of 400×400 nodes, while a naive BC requires more than 1000 nodes in each direction. This highlights the potential NRBCs have for accurate and efficient simulations.

Chapter 5

Summary and Outlook

Multi-speed Lattice Boltzmann Methods are derived from a systematic approximation to the Boltzmann equation and offer a promising way to expand the range of feasible simulation parameters. However, the choice of proper Boundary Conditions is arguably even more important than for standard lattices, as several layers of nodes need to be treated. This challenging task has only scarcely been addressed in the literature, which still limits a wide adoption of such methods.

In this work, this shortcoming was addressed by considering

1. wall BCs for the modelling of solid obstacles. This work introduced a Non-Equilibrium Bounce-Back (NEBB) BC for thermal multi-speed LBM. The new BC is completely local, as all necessary information is present on the boundary node in question. Its accuracy was evaluated and compared to established schemes in several well-known benchmarks.

   Core results are summarized as:

   - The NEBB BC gave superior accuracy over the diffusive [17] and regularized [18] BCs in the simulations of thermal Poiseuille and Couette flow at moderate Reynolds and Mach numbers, but slightly overestimated the critical Rayleigh number in simulations of natural convection.
   - In addition, two simple BCs, namely the Equilibrium Boundary Condition (EBC) and Non-Equilibrium Extrapolation (NEEP) BC were considered. While both schemes give acceptable accuracy for the channel flow benchmarks, the prediction of the critical Rayleigh number is of poor accuracy. This behaviour is contributed to the increased relevance of non-equilibrium information in the simulation of natural convection.

   The choice of BC always brings a trade-off between accuracy, stability and computational cost. The results reported above indicate that depending on the required level of accuracy and the degree of departure from equilibrium, choosing a simple BC with low computational cost may be acceptable [47]. In more complex flow configurations, only more sophisticated schemes yield acceptable accuracy and the choice of BC becomes a trade-off between stability and computational cost.

   Against this background, two natural research directions emerge to enable an informed choice: i) A stability analysis of the NEBB BC and ii) Minimization of the computational cost of the NEBB scheme: Depending on the velocity stencil used, complex analytical expressions for the missing populations are obtained. By carefully inspecting the order of magnitude of the individual terms, a more compact approximate expression that remains within an acceptable range of error may be found. Finally, it may be of interest to apply also the concept of moment based BCs [99] to multi-speed velocity stencils.

2. Non-Reflecting Boundary Conditions (NRBCs) modelling artificial boundaries. The work presented in this thesis is among the first studies of NRBC for multi-speed LBM. The established concepts of Characteristic Boundary Conditions, Perfectly Matched Layers and Discrete Artificial Boundary Conditions have been applied to multi-speed stencils and validated numerically by direct comparison against results obtained using single-speed stencils. As a novel contribution, a Characteristic Boundary Condition for thermal flow has been derived for the LBM by also accounting for the energy equation. A straightforward extension of Discrete Artificial Boundary Condition and Perfectly Matched Layers for thermal flow was given. All three approaches have shown to give a significant advantage over a naive zero gradient BC. Key properties of these schemes are summarized as follows:

    - The Discrete Artificial Boundary Condition is quite complex to implement but can in principle fulfil any accuracy requirement given the history depth is chosen large enough. However, even at moderate values, the computational cost of the scheme is infeasibly high.
    - Characteristic Boundary Conditions are not easy to implement, but model non-reflecting boundaries with satisfying accuracy at only a moderate computational cost. However, various approximations are necessary to treat corners and ensure stability.
    - Perfectly Matched Layers are straightforward to implement and have good non-reflecting properties. They rely on a grid extension, causing a small computational overhead. It was shown that the computational efficiency of the scheme can be further increased by combining it with the Characteristic Boundary Condition, as this allows for a smaller dampening zone to achieve a given level of accuracy.

    The current method of treating corner nodes in the CBC gives acceptable results at the intersection of two open boundaries. However, the treatment of corners between solid and open boundaries requires the definition of compatibility conditions [80]. The transfer of this concept to the LBM should be the investigated in the future. In addition, a higher order discretization of derivatives as proposed in [100] and flux-splitting schemes [101] may contribute to enhance the methods stability.

Bibliography

[1] E. Calore et al. “Design and Optimizations of Lattice Boltzmann Methods for Massively Parallel GPU-Based Clusters”. In: *Analysis and Applications of Lattice Boltzmann Simulations*. Ed. by P. Valero-Lara. IGI Global, 2018. Chap. 10, pp. 54–114.

[2] G. R. McNamara and G. Zanetti. “Use of the Boltzmann Equation to Simulate Lattice-Gas Automata”. In: *Physical Review Letters* 61.20 (Nov. 1988), 2332–2335. ISSN: 0031-9007. DOI: 10.1103/physrevlett.61.2332.

[3] P. J. Dellar. “Lattice Kinetic Schemes for Magnetohydrodynamics”. In: *Journal of Computational Physics* 179.1 (2002), pp. 95–126. DOI: 10.1006/jcph.2002.7044.

[4] V. E. Ambruș and V. Sofonea. “Quadrature-Based Lattice Boltzmann Models for Rarefied Gas Flow”. In: *Flowing Matter*. Ed. by F. Toschi and M. Sega. Cham: Springer International Publishing, 2019, pp. 271–299. ISBN: 978-3-030-23370-9. DOI: 10.1007/978-3-030-23370-9_9.

[5] A. Gabbana et al. “Relativistic lattice Boltzmann methods: Theory and applications”. In: *Physics Reports* 863 (2020). Relativistic lattice Boltzmann methods: Theory and applications, pp. 1–63. ISSN: 0370-1573. DOI: 10.1016/j.physrep.2020.03.004.

[6] K. Yamamoto, N. Takada, and M. Misawa. “Combustion simulation with Lattice Boltzmann method in a three-dimensional porous structure”. In: *Proceedings of the Combustion Institute* 30.1 (2005), pp. 1509–1515. ISSN: 1540-7489. DOI: 10.1016/j.proci.2004.08.030.

[7] C. M. Teixeira. “Incorporating Turbulence Models into the Lattice-Boltzmann Method”. In: *International Journal of Modern Physics C* 09.08 (Dec. 1998), 1159–1175. ISSN: 1793-6586. DOI: 10.1142/s0129183198001060.

[8] Z. Guo and T. S. Zhao. “Lattice Boltzmann model for incompressible flows through porous media”. In: *Phys. Rev. E* 66 (3 Sept. 2002), p. 036304. DOI: 10.1103/PhysRevE.66.036304.

[9] X. Shan and G. Doolen. “Multicomponent lattice-Boltzmann model with interparticle interaction”. In: *Journal of Statistical Physics* 81.1-2 (Oct. 1995), pp. 379–393. DOI: 10.1007/bf02179985.

[10] Q. Li et al. “Lattice Boltzmann methods for multiphase flow and phase-change heat transfer”. In: *Progress in Energy and Combustion Science* 52 (2016), pp. 62–105. ISSN: 0360-1285. DOI: https://doi.org/10.1016/j.pecs.2015.10.001.

[11] A. Scagliarini et al. “Lattice Boltzmann methods for thermal flows: Continuum limit and applications to compressible Rayleigh-Taylor systems”. In: *Physics of Fluids* 22.5 (2010), p. 055101. DOI: 10.1063/1.3392774.

[12] X. Shan, X.-F. Yuan, and H. Chen. “Kinetic theory representation of hydrodynamics: a way beyond the Navier-Stokes equation”. In: *Journal of Fluid Mechanics* 550 (2006), pp. 413–441. DOI: 10.1017/S0022112005008153.

[13] P. C. Philippi et al. "From the continuous to the lattice Boltzmann equation: The discretization problem and thermal models". In: *Physical Review E* 73.5 (May 2006). DOI: 10.1103/physreve.73.056702.

[14] X. B. Nie, X. Shan, and H. Chen. "Galilean invariance of lattice Boltzmann models". In: *EPL (Europhysics Letters)* 81.3 (Jan. 2008), p. 34005. ISSN: 1286-4854. DOI: 10.1209/0295-5075/81/34005.

[15] D. N. Siebert, L. A. Hegele, and P. C. Philippi. "Lattice Boltzmann equation linear stability analysis: Thermal and athermal models". In: *Phys. Rev. E* 77 (2 Feb. 2008), p. 026707. DOI: 10.1103/PhysRevE.77.026707.

[16] C. Coreixas et al. "Recursive regularization step for high-order lattice Boltzmann methods". In: *Physical Review E* 96.3 (Sept. 2017). ISSN: 2470-0053. DOI: 10.1103/physreve.96.033306.

[17] J. Meng and Y. Zhang. "Diffuse reflection boundary condition for high-order lattice Boltzmann models with streaming–collision mechanism". In: *Journal of Computational Physics* 258 (2014), pp. 601–612. ISSN: 0021-9991. DOI: 10.1016/j.jcp.2013.10.057.

[18] N. Frapolli, S. S. Chikatamarla, and I. V. Karlin. "Multispeed entropic lattice Boltzmann model for thermal flows". In: *Physical Review E* 90.4 (Oct. 2014). DOI: 10.1103/physreve.90.043306.

[19] H. Lee, S. Bawazeer, and A. Mohamad. "Boundary conditions for lattice Boltzmann method with multispeed lattices". In: *Computers & Fluids* 162 (2018), pp. 152–159. DOI: 10.1016/j.compfluid.2017.12.011.

[20] D. Heubes, A. Bartel, and M. Ehrhardt. "Discrete Artificial Boundary Conditions for the Lattice Boltzmann Method in 2D". In: *ESAIM: Proceedings and Surveys* 52 (Dec. 2015). Ed. by S. Dellacherie et al., pp. 47–65. DOI: 10.1051/proc/201552003.

[21] S. Izquierdo and N. Fueyo. "Characteristic nonreflecting boundary conditions for open boundaries in lattice Boltzmann methods". In: *Physical Review E* 78.4 (Oct. 2008). DOI: 10.1103/physreve.78.046707.

[22] A. Najafi-Yazdi and L. Mongeau. "An absorbing boundary condition for the lattice Boltzmann method based on the perfectly matched layer". In: *Computers & Fluids* 68 (Sept. 2012), pp. 203–218. DOI: 10.1016/j.compfluid.2012.07.017.

[23] F. Klass, A. Gabbana, and A. Bartel. "A non-equilibrium bounce-back boundary condition for thermal multispeed LBM". In: *Journal of Computational Science* 53 (July 2021), p. 101364. DOI: 10.1016/j.jocs.2021.101364.

[24] F. Klass, A. Gabbana, and A. Bartel. "A Non-Reflecting Boundary Condition for Multispeed Lattice Boltzmann Methods". In: *Progress in Industrial Mathematics at ECMI 2021*. Springer International Publishing, 2022, 447–453. DOI: 10.1007/978-3-031-11818-0_58.

[25] F. Klass, A. Gabbana, and A. Bartel. "A Characteristic Boundary Condition for Multispeed Lattice Boltzmann Methods". In: *Communications in Computational Physics* 33.1 (June 2023), pp. 101–117. DOI: 10.4208/cicp.oa-2022-0052.

[26] F. Klass, A. Gabbana, and A. Bartel. *Characteristic Boundary Condition for Thermal Lattice Boltzmann Methods*. 2023. arXiv: 2307.16766.

[27] D. Wolf-Gladrow. "Lattice-Gas Cellular Automata and Lattice Boltzmann Models - An Introduction". In: *Lattice-Gas Cellular Automata and Lattice Boltzmann Models* 1725 (Jan. 2000). DOI: 10.1007/b72010.

[28] X. He and L.-S. Luo. "Theory of the lattice Boltzmann method: From the Boltzmann equation to the lattice Boltzmann equation". In: *Physical Review E* 56.6 (Dec. 1997), pp. 6811–6817. DOI: 10.1103/physreve.56.6811.

[29] X. Shan. "The mathematical structure of the lattices of the lattice Boltzmann method". In: *Journal of Computational Science* 17 (2016), pp. 475–481. DOI: 10.1016/j.jocs.2016.03.002.

[30] S. Succi. *The Lattice Boltzmann Equation: For Complex States of Flowing Matter*. OUP Oxford, 2018. ISBN: 9780192538857. DOI: 10.1093/oso/9780199592357.001.0001.

[31] S. Succi. "Lattice Boltzmann beyond Navier-Stokes: Where do we stand?" In: *AIP Conference Proceedings*. Author(s), 2016. DOI: 10.1063/1.4967538.

[32] J. F. Wendt, ed. *Computational Fluid Dynamics*. Springer Berlin Heidelberg, 2009. DOI: 10.1007/978-3-540-85056-4.

[33] T. Krüger et al. *The Lattice Boltzmann Method*. Springer International Publishing, 2017. DOI: 10.1007/978-3-319-44649-3.

[34] C. Cercignani. *The Boltzmann Equation and Its Applications*. Springer New York, 1988. DOI: 10.1007/978-1-4612-1039-9.

[35] H. Struchtrup. *Macroscopic Transport Equations for Rarefied Gas Flows*. Springer Berlin Heidelberg, 2005. DOI: 10.1007/3-540-32386-4.

[36] D. Hänel. *Molekulare Gasdynamik*. Springer-Verlag, 2004. DOI: 10.1007/3-540-35047-0.

[37] S. Chapman et al. *The Mathematical Theory of Non-uniform Gases: An Account of the Kinetic Theory of Viscosity, Thermal Conduction and Diffusion in Gases*. 3. Cambridge Mathematical Library. Cambridge University Press, 1990. ISBN: 9780521408448. URL: https://books.google.de/books?id=y2Yyy798WzIC.

[38] P. L. Bhatnagar, E. P. Gross, and M. Krook. "A Model for Collision Processes in Gases. Amplitude Processes in Charged and Neutral One-Component Systems". In: *Phys. Rev.* 94.3 (1954), pp. 511–525. DOI: 10.1103/PhysRev.94.511.

[39] A. Agrawal, H. M. Kushwaha, and R. S. Jadhav. "Burnett Equations: Derivation and Analysis". In: *Microscale Flow and Heat Transfer: Mathematical Modelling and Flow Physics*. Cham: Springer International Publishing, 2020, pp. 125–188. ISBN: 978-3-030-10662-1. DOI: 10.1007/978-3-030-10662-1_5.

[40] H. Grad. "Note on N-dimensional hermite polynomials". In: *Communications on Pure and Applied Mathematics* 2.4 (Dec. 1949), pp. 325–330. DOI: 10.1002/cpa.3160020402.

[41] M. Sbragaglia et al. "Lattice Boltzmann method with self-consistent thermo-hydrodynamic equilibria". In: *Journal of Fluid Mechanics* 628 (June 2009), p. 299. DOI: 10.1017/s00221120090065x.

[42] Z. Guo, C. Zheng, and B. Shi. "Discrete lattice effects on the forcing term in the lattice Boltzmann method". In: *Physical Review E* 65.4 (Apr. 2002). DOI: 10.1103/physreve.65.046308.

[43] S. A. Bawazeer, S. S. Baakeem, and A. A. Mohamad. "A Critical Review of Forcing Schemes in Lattice Boltzmann Method: 1993–2019". In: *Archives of Computational Methods in Engineering* 28.7 (Feb. 2021), pp. 4405–4423. DOI: 10.1007/s11831-021-09535-4.

[44] X. Shan. "General solution of lattices for Cartesian lattice Bhatanagar-Gross-Krook models". In: *Phys. Rev. E* 81 (2010), p. 036702. DOI: 10.1103/PhysRevE.81.036702.

[45] U. Schiller. "Thermal fluctuations and boundary conditions in the lattice Boltzmann method". Dissertation. Johannes Gutenberg University Mainz, 2008. URL: https://openscience.ub.uni-mainz.de/bitstream/20.500.12030/3233/1/1841.pdf.

[46] Z. Guo et al. "Thermal lattice Boltzmann equation for low Mach number flows: Decoupling model". In: *Physical Review E* 75.3 (Mar. 2007). DOI: 10.1103/physreve.75.036704.

[47] A. A. Mohamad and S. Succi. "A note on equilibrium boundary conditions in lattice Boltzmann fluid dynamic simulations". In: *The European Physical Journal Special Topics* 171.1 (Apr. 2009), pp. 213–221. DOI: 10.1140/epjst/e2009-01031-9.

[48] J. Latt et al. "Straight velocity boundaries in the lattice Boltzmann method". In: *Phys. Rev. E* 77 (5 May 2008), p. 056703. DOI: 10.1103/PhysRevE.77.056703.

[49] D. P. Ziegler. "Boundary conditions for lattice Boltzmann simulations". In: *Journal of Statistical Physics* 71.5–6 (June 1993), 1171–1177. ISSN: 1572-9613. DOI: 10.1007/bf01049965.

[50] S. Ansumali and I. V. Karlin. "Kinetic boundary conditions in the lattice Boltzmann method". In: *Physical Review E* 66.2 (Aug. 2002). DOI: 10.1103/physreve.66.026311.

[51] G. Zhao-Li, Z. Chu-Guang, and S. Bao-Chang. "Non-equilibrium extrapolation method for velocity and pressure boundary conditions in the lattice Boltzmann method". In: *Chinese Physics* 11.4 (Mar. 2002), pp. 366–374. DOI: 10.1088/1009-1963/11/4/310.

[52] Q. Zou and X. He. "On the pressure and velocity boundary conditions for lattice Boltzmann BGK model". In: *Physics of Fluids* 9 (6 1997), pp. 1591–1598. DOI: 10.1063/1.869307.

[53] K. Hu et al. "A comparative study of boundary conditions for lattice Boltzmann simulations of high Reynolds number flows". In: *Computers & Fluids* 156 (Oct. 2017), pp. 1–8. DOI: 10.1016/j.compfluid.2017.06.008.

[54] O. Malaspinas, B. Chopard, and J. Latt. "General regularized boundary condition for multi-speed lattice Boltzmann models". In: *Computers & Fluids* 49.1 (Oct. 2011), pp. 29–35. DOI: 10.1016/j.compfluid.2011.04.010.

[55] J. Latt and B. Chopard. *Lattice Boltzmann Method with regularized non-equilibrium distribution functions*. 2005. DOI: 10.48550/ARXIV.PHYSICS/0506157.

[56] M. Hecht and J. Harting. "Implementation of on-site velocity boundary conditions for D3Q19 lattice Boltzmann simulations". In: *Journal of Statistical Mechanics: Theory and Experiment* 2010.01 (Jan. 2010), P01018. DOI: 10.1088/1742-5468/2010/01/p01018.

[57] T. Krüger, F. Varnik, and D. Raabe. "Shear stress in lattice Boltzmann simulations". In: *Physical Review E* 79.4 (Apr. 2009). DOI: 10.1103/physreve.79.046704.

[58] R. Huang, H. Wu, and N. A. Adams. "Lattice Boltzmann model with adjustable equation of state for coupled thermo-hydrodynamic flows". In: *Journal of Computational Physics* 392 (Sept. 2019), pp. 227–247. DOI: 10.1016/j.jcp.2019.04.044.

[59] X. Shan. "Simulation of Rayleigh-Bénard convection using a lattice Boltzmann method". In: *Physical Review E* 55.3 (Mar. 1997), pp. 2780–2788. DOI: 10.1103/physreve.55.2780.

[60] J. Wang et al. "Lattice Boltzmann simulations of thermal convective flows in two dimensions". In: *Computers & Mathematics with Applications* 65.2 (Jan. 2013), pp. 262–286. DOI: 10.1016/j.camwa.2012.07.001.

[61] I. V. Karlin, D. Sichau, and S. S. Chikatamarla. "Consistent two-population lattice Boltzmann model for thermal flows". In: *Physical Review E* 88.6 (Dec. 2013). DOI: 10.1103/physreve.88.063310.

[62] I. E. A. Spiegel. "Convective Instability in a Compressible Atmosphere." In: *The Astrophysical Journal* 141 (Apr. 1965), p. 1068. DOI: 10.1086/148197.

[63] D. O. Gough et al. "Convective Instability in a Compressible Atmosphere. II". In: *The Astrophysical Journal* 206 (June 1976), p. 536. DOI: 10.1086/154409.

[64] U. Ghia, K. Ghia, and C. Shin. "High-Re solutions for incompressible flow using the Navier-Stokes equations and a multigrid method". In: *J. Comput. Phys.* 48 (1982). DOI: 10.1016/0021-9991(82)90058-4.

[65] D. Givoli. "Non-reflecting boundary conditions". In: *Journal of Computational Physics* 94.1 (May 1991), pp. 1–29. DOI: 10.1016/0021-9991(91)90135-8.

[66] T. Colonius. "MODELING ARTIFICIAL BOUNDARY CONDITIONS FOR COMPRESSIBLE FLOW". In: *Annual Review of Fluid Mechanics* 36.1 (Jan. 2004), pp. 315–345. DOI: 10.1146/annurev.fluid.36.050802.121930.

[67] F. Q. Hu. "Absorbing Boundary Conditions". In: *International Journal of Computational Fluid Dynamics* 18.6 (Aug. 2004), pp. 513–522. DOI: 10.1080/10618560410001673524.

[68] B. Engquist and A. Majda. "Absorbing boundary conditions for the numerical simulation of waves". In: *Mathematics of Computation* 31.139 (1977), pp. 629–651. DOI: 10.1090/s0025-5718-1977-0436612-4.

[69] G. Hedstrom. "Nonreflecting boundary conditions for nonlinear hyperbolic systems". In: *Journal of Computational Physics* 30.2 (Feb. 1979), pp. 222–237. DOI: 10.1016/0021-9991(79)90100-1.

[70] K. W. Thompson. "Time dependent boundary conditions for hyperbolic systems". In: *Journal of Computational Physics* 68.1 (Jan. 1987), pp. 1–24. DOI: 10.1016/0021-9991(87)90041-6.

[71] T. Poinsot and S. Lelef. "Boundary conditions for direct simulations of compressible viscous flows". In: *Journal of Computational Physics* 101.1 (July 1992), pp. 104–129. DOI: 10.1016/0021-9991(92)90046-2.

[72] H. Han, J. Lu, and W. BAO. "A discrete artificial boundary condition for steady incompressible viscous flows in a no-slip channel using a fast iterative method". In: *Journal of Computational Physics* 114.2 (Oct. 1994), pp. 201–208. DOI: 10.1006/jcph.1994.1160.

[73] J.-P. Berenger. "A perfectly matched layer for the absorption of electromagnetic waves". In: *Journal of Computational Physics* 114.2 (1994), pp. 185–200. ISSN: 0021-9991. DOI: https://doi.org/10.1006/jcph.1994.1159.

[74] F. Q. Hu. "A Stable, Perfectly Matched Layer for Linearized Euler Equations in Unsplit Physical Variables". In: *Journal of Computational Physics* 173.2 (Nov. 2001), pp. 455–480. DOI: 10.1006/jcph.2001.6887.

[75] F. Q. Hu. "A Perfectly Matched Layer absorbing boundary condition for linearized Euler equations with a non-uniform mean flow". In: *Journal of Computational Physics* 208.2 (Sept. 2005), pp. 469–492. DOI: 10.1016/j.jcp.2005.02.028.

[76] F. Q. Hu, X. Li, and D. Lin. "Absorbing boundary conditions for nonlinear Euler and Navier–Stokes equations based on the perfectly matched layer technique". In: *Journal of Computational Physics* 227.9 (Apr. 2008), pp. 4398–4424. DOI: 10.1016/j.jcp.2008.01.010.

[77] D. Heubes. "Artificial Boundary Conditions in the Lattice Boltzmann Method". Dissertation. Bergische Universität Wuppertal, 2016. URL: http://elpub.bib.uni-wuppertal.de/servlets/DerivateServlet/Derivate-6425/dc1702.pdf.

[78] C. S. Yoo et al. "Characteristic boundary conditions for direct simulations of turbulent counterflow flames". In: *Combustion Theory and Modelling* 9.4 (Nov. 2005), pp. 617–646. DOI: 10.1080/13647830500307378.

[79] C. S. Yoo and H. G. Im. "Characteristic boundary conditions for simulations of compressible reacting flows with multi-dimensional, viscous and reaction effects". In: *Combustion Theory and Modelling* 11.2 (Apr. 2007), pp. 259–286. DOI: 10.1080/13647830600898995.

[80] G. Lodato, P. Domingo, and L. Vervisch. "Three-dimensional boundary conditions for direct and large-eddy simulation of compressible viscous flows". In: *Journal of Computational Physics* 227.10 (May 2008), pp. 5105–5143. DOI: 10.1016/j.jcp.2008.01.038.

[81] D. Heubes, A. Bartel, and M. Ehrhardt. "Characteristic boundary conditions in the lattice Boltzmann method for fluid and gas dynamics". In: *Journal of Computational and Applied Mathematics* 262 (May 2014), pp. 51–61. DOI: 10.1016/j.cam.2013.09.019.

[82] N. Jung, H. W. Seo, and C. S. Yoo. "Two-dimensional characteristic boundary conditions for open boundaries in the lattice Boltzmann methods". In: *Journal of Computational Physics* 302 (Dec. 2015), pp. 191–199. DOI: 10.1016/j.jcp.2015.08.044.

[83] G. Wissocq et al. "Regularized characteristic boundary conditions for the Lattice-Boltzmann methods at high Reynolds number flows". In: *Journal of Computational Physics* 331 (Feb. 2017), pp. 1–18. DOI: 10.1016/j.jcp.2016.11.037.

[84] D. H. Rudy and J. C. Strikwerda. "A nonreflecting outflow boundary condition for subsonic Navier-Stokes calculations". In: *Journal of Computational Physics* 36.1 (June 1980), pp. 55–70. DOI: 10.1016/0021-9991(80)90174-6.

[85] X. Chen, K. Yang, and X. Shan. "Characteristic boundary condition for multispeed lattice Boltzmann model in acoustic problems". In: *Journal of Computational Physics* (June 2023), p. 112302. DOI: 10.1016/j.jcp.2023.112302.

[86] J. Stoer and R. Bulirsch. *Introduction to Numerical Analysis*. Springer New York, 2002. DOI: 10.1007/978-0-387-21738-3.

[87] F. Collino and C. Tsogka. "Application of the perfectly matched absorbing layer model to the linear elastodynamic problem in anisotropic heterogeneous media". In: *GEOPHYSICS* 66.1 (2001), pp. 294–307. DOI: 10.1190/1.1444908.

[88] X. Antoine et al. "A Review of Transparent and Artificial Boundary Conditions Techniques for Linear and Nonlinear Schrödinger Equations". In: *Communications in Computational Physics* 4 (Oct. 2008), pp. 729–796.

[89] I. Singer and E. Turkel. "A perfectly matched layer for the Helmholtz equation in a semi-infinite strip". In: *Journal of Computational Physics* 201.2 (Dec. 2004), pp. 439–465. DOI: 10.1016/j.jcp.2004.06.010.

[90] F. Q. Hu and E. Craig. "On the Perfectly Matched Layer for the Boltzmann-BGK Equation and its Application to Computational Aeroacoustics". In: *16th AIAA/CEAS Aeroacoustics Conference*. American Institute of Aeronautics and Astronautics, June 2010. DOI: 10.2514/6.2010-3935.

[91] M. Tekitek et al. "Towards perfectly matching layers for lattice Boltzmann equation". In: *Computers & Mathematics with Applications* 58.5 (Sept. 2009), pp. 903–913. DOI: 10.1016/j.camwa.2009.02.013.

[92] A. Modave, E. Delhez, and C. Geuzaine. "Optimizing perfectly matched layers in discrete contexts". In: *International Journal for Numerical Methods in Engineering* 99.6 (May 2014), pp. 410–437. DOI: 10.1002/nme.4690.

[93] E. Craig. "Perfectly Matched Layer Absorbing Boundary Conditions for the Discrete Velocity Boltzmann-BGK Equation". PhD thesis. 2011. DOI: 10.25777/VKXG-KE33. URL: https://digitalcommons.odu.edu/mathstat_etds/19/.

[94] D. Heubes, A. Bartel, and M. Ehrhardt. "Concept for a one-dimensional discrete artificial boundary condition for the lattice Boltzmann method". In: *Computers & Mathematics with Applications* 70.10 (Nov. 2015), pp. 2316–2330. DOI: 10.1016/j.camwa.2015.08.030.

[95] M. Laroussi and M. Djebbi. "Vortex Shedding for Flow Past Circular Cylinder: Effects of Initial Conditions." In: *Universal Journal of Fluid Mechanics.* 3 (Jan. 2015), pp. 19–32. ISSN: 19-32.2241-763X.

[96] D. A. Perumal, G. V. S. Kumar, and A. K. Dass. "Numerical Simulation of Viscous Flow over a Square Cylinder Using Lattice Boltzmann Method". In: *ISRN Mathematical Physics* 2012 (Sept. 2012), pp. 1–16. DOI: 10.5402/2012/630801.

[97] A. J. Ladd. "Numerical simulations of particulate suspensions via a discretized Boltzmann equation. Part 1. Theoretical foundation". In: *Journal of fluid mechanics* 271 (1994), pp. 285–309.

[98] D. Yu et al. "Viscous flow computations with the method of lattice Boltzmann equation". In: *Progress in Aerospace Sciences* 39.5 (July 2003), pp. 329–367. DOI: 10.1016/s0376-0421(03)00003-4.

[99] L. A. Hegele et al. "High-Reynolds-number turbulent cavity flow using the lattice Boltzmann method". In: *Physical Review E* 98.4 (Oct. 2018). ISSN: 2470-0053. DOI: 10.1103/physreve.98.043302.

[100] D. N. Siebert, P. C. Philippi, and K. K. Mattila. "Consistent lattice Boltzmann equations for phase transitions". In: *Physical Review E* 90.5 (Nov. 2014). ISSN: 1550-2376. DOI: 10.1103/physreve.90.053310.

[101] M.-S. Liou and C. J. Steffen. "A New Flux Splitting Scheme". In: *Journal of Computational Physics* 107.1 (July 1993), 23–39. ISSN: 0021-9991. DOI: 10.1006/jcph.1993.1122.